UC San Diego

UC San Diego Electronic Theses and Dissertations

Title

Synchrony and concerted activity in the neural code of the retina

Permalink

https://escholarship.org/uc/item/2q2183k3

Author

Shlens, Jonathon

Publication Date

2007

Peer reviewed|Thesis/dissertation

eScholarship.org Powered by the California Digital Library
University of California

UNIVERSITY OF CALIFORNIA, SAN DIEGO

Synchrony and Concerted Activity in the Neural Code of the Retina.

A dissertation submitted in partial satistfaction of the
requirements for the degree

Doctor of Philosophy

in

Neurosciences

by

Jonathon Shlens

Committee in charge:

Professor E.J. Chichilnisky, Chair
Professor Henry D.I. Abarbanel, Co-Chair
Professor Marla Feller
Professor Pam Reinagel
Professor Charles F. Stevens

2007

Copyright

Jonathon Shlens, 2007

All rights reserved.

The dissertation of Jonathon Shlens is approved, and it is acceptable in quality and form for publication on micro-film:

_____

_____

_____

_____
Co-Chair

_____
Chair

University of California, San Diego

2007

For my teachers and mentors.

. . . to him the meaning of an episode was not inside like a kernel but outside, enveloping the tale which brought it out only as a glow brings out a haze, in the likeness of one of these misty halos that sometimes are made visible by the spectral illumination of moonshine.

— Joseph Conrad

If a theory in neuroscience is worth anything, it should be able to simplify the description of a neural circuit.

— Robert W Rodieck

Contents

List of Figures

List of Tables

Acknowledgements

The last five years have been a challenge overcoming more obstacles than I would possibly expect when I began my graduate career. My friends have been a constant support for me throughout every aspect of graduate school and made my dissertation possible. My graduate career has probably been influenced most by my roommate of the past five years and fellow graduate student, Kevin Wood. I must thank him as well as my other roommate Kevin Briggman for many memorable years and cultivating a passion for science.

As a graduate student I don't get many opportunities to shower accolades on my advisor but now I get such a chance. EJ has been an amazing mentor, advisor and teacher over my time in graduate school. He has been everything I could possibly want in an advisor — a patient, understanding and caring individual and a diligent, creative and insightful scientist. I could only hope to aspire to such a role in my future. Thank you EJ.

Graduate school is a tremendous journey with many highs and lows. Particularly during the lows every bit of encouragement and guidance goes a long way. For this I would like to acknowledge the support of Marla Feller, Henry Abarbanel, Geoff Boynton, Ken Kreutz-Delgado, Sascha Du Lac, Darwin Berg and Bill Kristan. Bill Kristan and Henry Abarbanel have been consummate advocates for me over the years far above and beyond my expectations, and for that I am eternally grateful.

I attribute many of the ideas that permeate my work to the tremendous teaching and advice from a wide variety of institutions including UC San Diego. Most of my research interests have been inspired by tremendous courses taught by faculty including John Boccio (Swarthmore College), Lisa Meeden (Swarthmore College), Geoffrey Owen (UC Berkeley), Bruce Graham (University of Edinburgh) and Bill Bialek (Marine Biological Laboratory). At UC San Diego my perspectives on neuroscience and statistics have been heavily influenced by classes taught by Henry Abarbanel, Terry Sejnowski, David Kleinfeld and an inspirational series of classes taught by Ken Kreutz-Delgado. Likewise, interactions and discussion with my collaborators, Matt Kennel, Liam Paninski, Jonathan Pillow, Eero Simoncelli and Fred Rieke, have been invaluable, providing insightful perspectives on many problems.

Many of my experiments were collaborative and required the patience, assistance and diligence of every member in the laboratory. To all of the members of the laboratory, I am indebted, but I would particularly like to acknowledge the help and guidance of a few past and present lab members. In particular, Valerie Uzzell and Jessica French shepherded me into the lab and taught me many experimental techniques. Subsequent lab technicians Brooke Kutka and Clare Hulse have provided generous support in experiments and data analysis. Greg Field has provided endless streams of advice and ideas throughout my years in the lab. Alexander "Sasha" Sher, Rachel Kalmar and Martin Greschner have been constant, heroic forces in many of our marathon experiments. Much experimental work has rested on the generosity of Ed Callaway, Howard Fox and Kent Osborn as well as the technical developments of Alan Litke, Wladeck Dabrowski, Alex Grillo, Pawel Grybos, Pawel Hottowy, Sergei Kachiguine, Dumitru Petrusca, Matthew Grivich and Steve Barry.

My graduate studies have been supported by many generous funding organizations includ-

ing NSF IGERT for Computational Neuroscience, NSF IGERT for Vision and Learning in Humans and Machines and Burroughs-Wellcome La Jolla Interfaces in the Sciences.

All of the work in thesis has been co-authored with various faculty, post-doctoral researchers and graduate students. I have received permission from all of them allowing me to include this work in my thesis. Figures 1.1, 2.1, 2.3, 4.1, 4.2 and parts of Figure 3.2 include material published elsehwhere. I have received permission to reproduce such figures.

This thesis is comprised of three works which have or will be submitted for publication. I have received permission from the respective co-authors to include this work in my thesis. The first four chapters as well as the last chapter are taken from the the first reference listed below. Chapter 5 and 6 are from the last two references, respectively.

Shlens J and Chichilnisky EJ, (2007) *Synchrony and concerted activity in the neural code of the retina.* In RR Hoy, GM Shepherd, AI Basbaum, A Kaneko and G Westheimer (ed). **The Senses: A Comprehensive Foundation**, Elsevier Press.

Shlens J, Field GD, Gauthier JL, Greschner M, Sher A, Litke AM, EJ Chichilnisky. *Islands of large-scale concerted activity in primate retina.* to appear.

Shlens J, Field GD, Gauthier JL, Grivich MI, Petrusca D, Sher A, Litke AM & EJ Chichilnisky, (2006) *The structure of multi-neuron firing patterns in primate retina.* **Journal of Neuroscience**, 26(32): 8254-8266.

Vita

1999	B. A. with High Honors, Physics and Computer Science. Swarthmore College.
1999–2001	Research Engineer, Research and Development Division. Pixar Animation Studios.
2003	Summer Student, Methods in Computational Neuroscience. Marine Biological Laboratory
2003–2006	Teaching assistant, Departments of Biology and Physics. University of California, San Diego
2003–2007	Triathlon coach, Team in Training program. Leukemia and Lymphoma Society
2007	Ph. D., University of California San Diego Department of Neurosciences

Publications

Kennel M, Shlens J, Abarbanel HDI & EJ Chichilnisky (2005) *Estimating entropy rates with Bayesian confidence intervals.* **Neural Computation**, 17: 1531-1576.

Shlens J, Field GD, Gauthier JL, Grivich MI, Petrusca D, Sher A, Litke AM & EJ Chichilnisky, (2006) *The structure of multi-neuron firing patterns in primate retina.* **Journal of Neuroscience**, 26(32): 8254-8266.

Shlens J, Kennel M, Abarbanel HDI & EJ Chichilnisky (2007) *Estimating information rates in neural spike trains with confidence intervals.* **Neural Computation**, 19:7.

Shlens J and Chichilnisky EJ, (2007) *Synchrony and concerted activity in the neural code of the retina.* In RR Hoy, GM Shepherd, AI Basbaum, A Kaneko and G Westheimer (ed). **The Senses: A Comprehensive Foundation**, Elsevier Press.

Pillow J, Shlens J, Paninski L, Sher A, Litke A, Chichilnisky EJ, E Simoncelli. *Correlations and multi-neuronal coding in primate retina.* to appear.

Shlens J, Field GD, Gauthier JL, Greschner M, Sher A, Litke AM, EJ Chichilnisky. *Islands of large-scale concerted activity in primate retina.* to appear.

Fields of Study

Major Field: Neurosciences, Specialization in Computational Neuroscience

Studies in Statistics, Professors Ruth Williams, Alon Orlitksy

Studies in Machine Learning, Professors Kenneth Kreutz-Delgado, Nuno Vasconcelos

ABSTRACT OF THE DISSERTATION

Synchrony and Concerted Activity in the Neural Code of the Retina.

by

Jonathon Shlens

Doctor of Philosophy in Neurosciences

University of California, San Diego, 2007

Professor E.J. Chichilnisky, Chair

Professor Henry Abarbanel, Co-Chair

All visual information the brain receives originates in the electrical activity of a final layer of cells in the retina, termed retinal ganglion cells (RGCs). The electrical activity of RGCs constitute the language neurons use to communicate sensory information, constraining computations performed by the nervous system and illuminating how information is represented in the brain more generally.

The electrical activity across RGCs is known to be correlated, reflecting circuitry internal to the retina and thus influencing how visual information is conveyed from the eye to the brain. Over the last few years the research compiled in this dissertation provide the first reports of concerted activity, such as synchrony, in primate RGCs. Furthermore, with the development of

new recording technologies, this work has explored the spatial and numerical scale of concerted activity in the primate retina with the ultimate goal of discerning it's role in the signaling of visual information. In the process new quantitative tools exploiting ideas from statistics and information theory have been developed to explore such questions with the hope that such work can be extended to understand the activity of neural systems more generally.

The following dissertation is largely comprised of three main parts corresponding to three published or forthcoming works. The first four chapters as well as the conclusions are largely taken from an invited book chapter of the same title. Chapter 5 consists of published material that provided one of the first accounts of concerted activity as well as introduced many quantitative tools exploited to successfully explain such activity. Chapter 6 is a first draft of a forthcoming publication extending previous work to explore the concerted activity of an entire population of RGCs.

Chapter 1

Introduction

A common thread in systems neuroscience is the constant interplay between the external sensory world and the internal dynamics of networks of neurons in the nervous system [168, 48]. In early sensory systems one amenable model for studying this interaction exists in the signaling of visual information from the eye to the brain – both driven by extrinsic visual stimulation and shaped by the intrinsic circuitry of the retina. The observation of correlated activity, such as synchrony, in the spiking activity along the optic nerve offers a window onto the function of the underlying neural circuitry in the presence of sensory signals – constraining the time and spatial scales at which retinal circuits operate and providing clues about the biophysical mechanisms used to construct such circuits [245]. The investigation of correlated activity in the neural code of the retina is of fundamental interest because these correlations shape how visual information is signaled from the eye to the brain and ultimately lend insight into how neural circuits in other sensory modalities and cortical areas represent and process information [243].

Correlated activity, such as synchrony, is measured in the final layer of neurons, termed

retinal ganglion cells (RGCs), whose axons compose the optic nerve. Correlation between mature RGCs have been identified in all species of retina investigated, including goldfish [12], salamander [191, 41, 259], frog [129], rat [119], mouse [206], rabbit [13, 4, 125, 77, 11], guinea pig [259], cat [181, 182, 183, 203, 204] and primate [273] (for studies of RGC correlation in development, see [98]). The prevalence and consistency of observations suggests that specific circuits and mechanisms underlying correlated activity are conserved across species [310]. Hence, investigating forms of correlation might yield insight into conserved principles underlying the construction of retinal circuits and possibly their underlying functional roles.

Other sensory modalities exploit synchrony and correlation for the transmission and downstream decoding of behaviorally relevant, sensory information [287, 162]. Given evolutionary pressures [15, 20], several have speculated whether correlated activity is likewise exploited by the early visual system [300, 190]. In particular, correlated firing in RGCs could provide dedicated visual information about fine spatial detail [191, 189, 261], global scene features [148], looming sensations [129] or backup (redundant) information about visual features [239, 257] (see also [269]). Ultimately, understanding the role of correlated activity in the representation of sensory information will yield insight into population coding in general [45] and inform our understanding of how network interactions influence information processing in higher cortical areas [279, 48, 139, 283].

In what follows we review the literature on correlated activity in the retina, focusing on three main issues: what are the underlying mechanisms and circuits (Section 2), what types of correlated activity have been documented (Section 3), and finally how does correlated activity effect the coding of visual information (Section 4). These issues require a wide ranging discussion from the basic biophysical mechanisms to quantitative notions of neural coding. We discuss all ideas but reserve some quantitative topics for the appendix. Before we consider such topics,

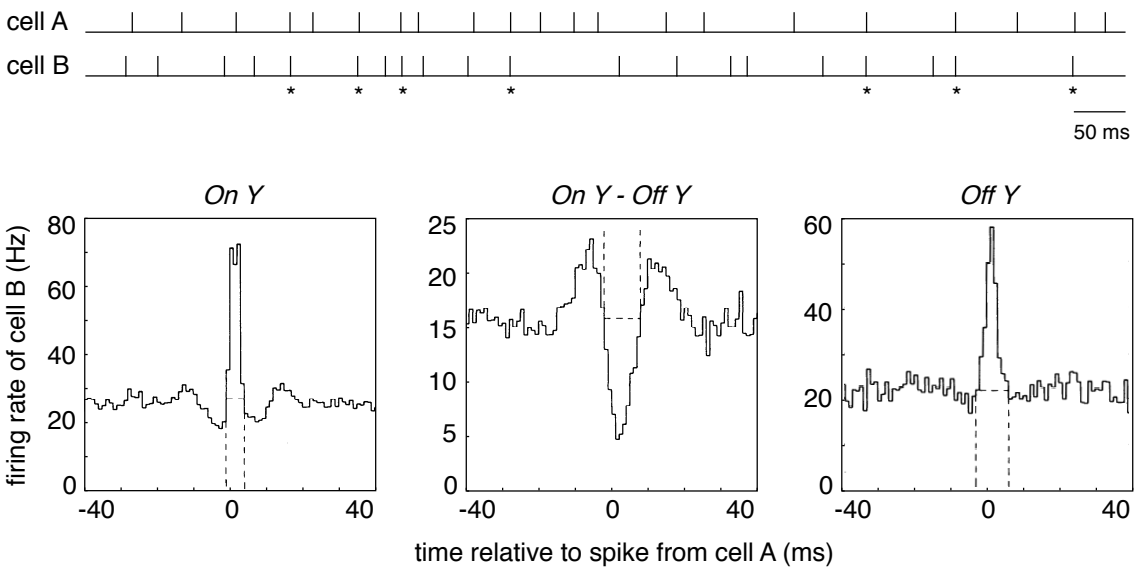

Figure 1.1: Synchrony and anti-synchrony between pairs of cat RGCs. The top panel shows a segment of simultaneously recorded spike trains with identified synchronous events (asterisks). The degree of correlation is measured by calculating the cross-correlation, or the average firing rate of one neuron as a function of the second neuron's spike time [227]. This is performed by accumulating the spike times of one neuron relative to the spike times of the second neuron and histograming at some small temporal resolution (1 ms). The x-axis represents the relative time of spikes from cell A to B, where cell A is presumed to have spikes at $t = 0$. The y-axis is a histogram count of spike times occuring within the resolution time (1 ms), converted into a spike rate. The flanks of the graph are a measure of the free firing rate of cell A and the pronounced peak (trough) represents the statistical dependency between the two spike trains termed (anti-) synchrony. Figures adapted from [181, 184].

we first discuss the basic observation of correlated activity to familiarize the reader and set a framework for subsequent discussion.

1.1 Basic observations

Although suggestions of correlated activity in the retina had existed in gross electrode recording along the optic nerve (e.g. [6, 5]) and multi-unit recordings in target neurons [281, 14, 286], the first observation of correlated spike trains in the retina did not occur until 1967 by Bob Rodieck [244] and later followed with the first observation of synchronous activity by David Arnett [12] (for negative results, see [106, 254]). Arnett recognized that nearby RGCs tended to exhibit correlation while distant RGCs showed no significant correlation [12, 13]. These observa-

tions were placed on clear footing by the pioneering work of David Mastronarde [181, 182, 183] who systematically documented the basic phenomenology of correlated activity in the cat retina (reviewed in [184]). Mastronarde demonstrated that correlated activity (1) systematically depends on cell type and cell body location and (2) reflect multiple, distinct mechanisms and circuits in the retina. In what follows we survey these basic observations to familiarize the reader with the phenomena and highlight some basic considerations when discussing correlated activity in the retina.

Although the tendency for nearly simultaneous activity can be identified in individual spike trains (Figure 1.1, top panel), the basic observation is often visualized with a cross-correlogram [227]: a single RGC exhibits a several fold increment (or decrement) in firing rate within milliseconds of a second cell's spike time (Figure 1.1, bottom panels). This prominent peak (or trough) is termed (anti-) synchrony. Note that the time scale of correlated activity occurs within the integration period of a typical neuron [139]. This observation immediately raises several important considerations in the context of the retina.

Intrinsic vs. induced correlations. Observed correlations are either generated internally by the circuitry of the retina or artificially by common visual stimulation (e.g. full field flashes). This distinction is fundamental and is reinforced semantically by distinguishing between *stimulus* and *noise induced correlations*, respectively [227, 257].

The architecture and cell types of the retina. The retina is a highly stereotyped structure, consisting of morphologically distinct cell types [245], each of which tile all of visual space [310] and mediate multiple, distinct, parallel visual pathways [96]. In particular, in higher mammalian species each RGC type independently tiles visual space in the retina and projects to

distinct target areas in the brain [96].

Returning to the cross-correlograms in Figure 1.1, we now elaborate – the observed correlations were recorded in the presence of constant illumination of a mesopic light source. Thus, these correlations are *noise correlations* and reflect the intrinsic circuitry of the cat retina: something within the retina caused both neurons to fire nearly simultaneously. Identifying such mechanisms underlying noise correlations requires a closer examination of the circuitry of the retina.

The circuitry of the retina is largely circumscribed by morphologically defined cell types [245]. Each visual pathway is constructed from distinct sets of cell types (e.g. single photon absorption events via rods, rod bipolars and AII amacrine cells [97]) terminating at the RGC population. Thus, one expects individual RGC types to reflect distinct underlying circuits and exhibit unique forms of correlations. Indeed, in Figure 1.1 the magnitude, sign and detailed timing properties of cross-correlograms vary across the pair of cells examined.

The circuitry underlying correlated activity could reflect multiple, distinct mechanisms and types of circuits. Hints of this fact can be seen in the variation in timing precision and polarity of the correlation across Figure 1.1 (e.g. the double peaks in the ON-Y pair [183]). These distinct forms of correlation are reinforced by the three time scales for observed correlation in salamander (Figure 2.1), suggestive of several putative mechanisms [41]. These mechanisms could employ electrical and/or chemical synapses and confer distinct functional consequences (e.g. driving activity vs. reciprocal interactions). We will discuss these issues in depth as well as review evidence for the range of mechanisms the retina might employ in the following section.

In the mean time, we hope that this brief survey has familiarized the reader with the basic phenomena (Figure 1.1) and highlighted the major considerations in the investigation of syn-

chronous activity in the retina – namely, the types of correlation and the prominence of cell types in retinal circuits. Needless to say, we will focus this manuscript on the observation of *noise correlations* to elucidate the types of neural circuits in the retina. We return to discussing the role of all types of correlation in the context of discussing the signaling of visual information (Section 4).

This chapter is taken from J Shlens and EJ Chichilnisky, (2007) *Synchrony and concerted activity in the neural code of the retina.* In RR Hoy, GM Shepherd, AI Basbaum, A Kaneko and G Westheimer (ed). **The Senses: A Comprehensive Foundation**, Elsevier Press.

Chapter 2

Mechanisms and circuitry underlying correlated activity

The relationship between identifying neural circuitry and observing correlated activity is reciprocal: each facet mutually informs the other and both ultimately inform our understanding of the function of these neural circuits in the retina. In this section we discuss the observation of correlated activity as well as biophysical evidence accrued from a diversity of experimental approaches in order to elucidate the range of mechanisms and circuits underlying this phenomena.

Achieving this goal ultimately requires a comprehensive discussion of evidence for all retinal circuits. Such a discussion however would be superfluous for our purposes as large bases of literature instead focus on aspects such as receptive field formation [141], dedicated pathways for light levels [97] and adaptation in neural responses [18] - most of which implicitly concerns single RGC responses. Thus, we selectively review the literature on retinal circuitry and mechanisms concentrating on aspects of the literature that might give rise to correlations between RGCs but note that the types of mechanisms mediating correlations could depend on stimulus features, light

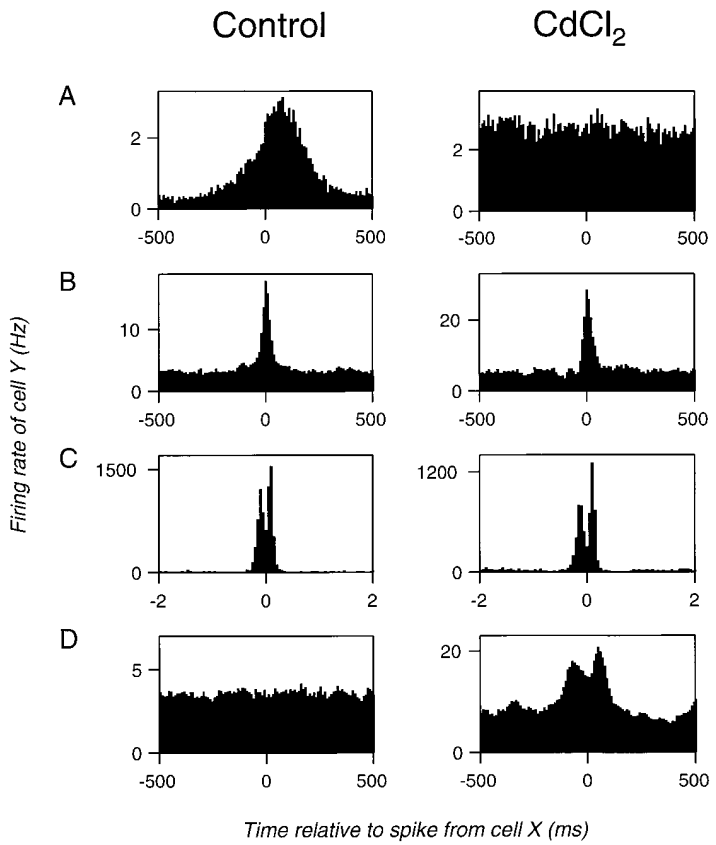

Figure 2.1: Time scales of synchrony in salamander. Left column is control and right column is addition of $CdCl_2$ to block chemical synaptic transmission. A) Broad correlations mediated through chemical synapses, possibly shared photoreceptor input. B) Medium correlations mediated through gap junctions, possibly through an amacrine cell. C) Narrow correlations mediated through gap junctions. D) Propagating waves occurring the presence of chemical synaptic blockade. Figure adapted from [41].

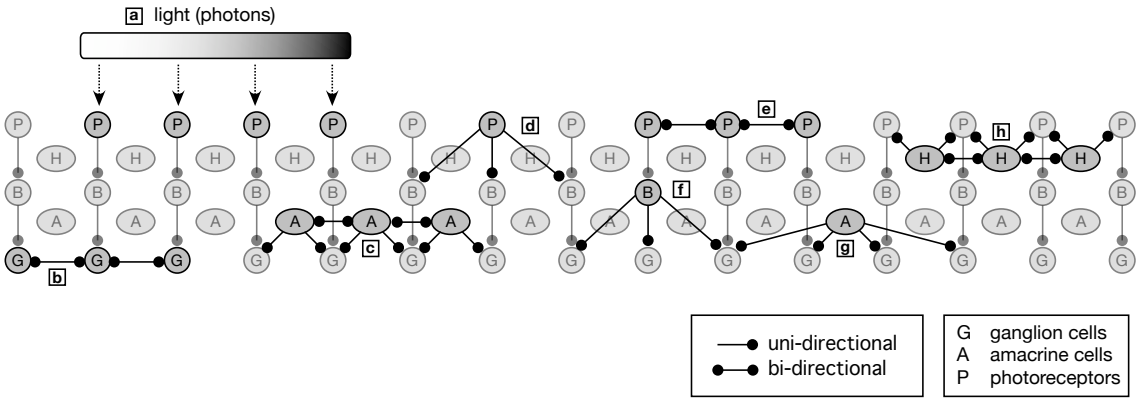

Figure 2.2: Diagram of potential mechanisms underlying synchrony. (a) Stimulus-induced correlations [257, 227]. (b) Electrical coupling between RGCs [65, 130, 246, 125, 183, 119]. (c) Divergence from and coupling between amacrine cells [65, 130, 107, 301, 303, 328, 306, 4]. (d) Divergent output from photoreceptors [253, 138]. (e) Electrical coupling between photoreceptors [255, 256]. (f) Divergent output from bipolar cells [253, 245]. (g) Widespread divergence from amacrine cells [171, 172, 284]. (h) Coupling between photoreceptors mediated through horizontal cells [245].

levels or individual species (see Figure 2.2 for a summary).

We broadly distinguish between two methods for generating correlated activity: (1) reciprocal interactions and (2) driving input. These two methods do not necessarily correspond to biophysical mechanisms but are qualitative descriptions of the neural circuits. Reciprocal interactions means that one RGC drives a second RGC, and vice versa. This method, for instance, could correspond to gap junction coupling mediated through an amacrine cell (e.g. Section 2.1.2). Driving input refers to an underlying neuron driving action potentials unidirectionally in more than one RGC. This method, for instance, could also correspond to gap junction coupling between a pair of RGCs and an amacrine cell. *We emphasize that this single retinal circuit could mediate both functions.* Hence, although this distinction is important for differentiating between qualitative phenomena (as well as statistical properties; see Section 4), it is important to be cautious at interpreting how a neural circuit operates (e.g. reciprocal interactions) based on the observation of a biophysical mechanism.

2.1 Electrical coupling between retinal ganglion cells

Many lines of evidence support the hypothesis that electrical coupling between RGCs mediate correlated activity (Figure 2.2b,c). The most direct evidence comes from biotinylated tracer dye studies [301]. Biotinylated dyes have proven superior then standard fluorescent dyes (e.g. Lucifer yellow) at revealing coupling between neurons (e.g. B-type horizontal cells, AII amacrine cells [68, 114, 194]). When neurobiotin is injected into individual ON and OFF parasol cells [65, 107, 130, 246] or α-ganglion cells in cat [301, 302], rabbit [328, 306], mouse [262], and ferret [223], this dye propagates to neighboring, homologous RGCs as well as several types of amacrine cells. Examples of this dye propagation are in Figure 2.3a,c. The physical propagation of this dye strongly suggests a electrical connection between pairs of RGCs. Conversely, α-ganglion cells in rat [119] and rabbit [125], which do not exhibit tracer coupling, do not exhibit synchrony.

Tracer studies provide strong evidence for a physical connection but must be considered in light of several complicating factors. In particular, the presence of tracer dye does not always correspond to physiologically significant coupling (e.g. ON-OFF DS ganglion cells in rabbit [302, 330, 78]) and the lack of tracer dye does not necessarily confirm the lack of electrical coupling because some dyes such as Lucifer Yellow do not pass through all types of ganglion cells [124]. These complications are explained by details of compartmentalization within a single cell, impedance mismatches between cells [124, 196, 197] and most importantly, the selectivity of gap junctions to the ionic charge of common tracer dyes [195, 197]. However, a new generation of tracer dyes may overcome some of these limitations [124].

Electrical coupling is presumed to be mediated through gap junctions [56, 57] and much

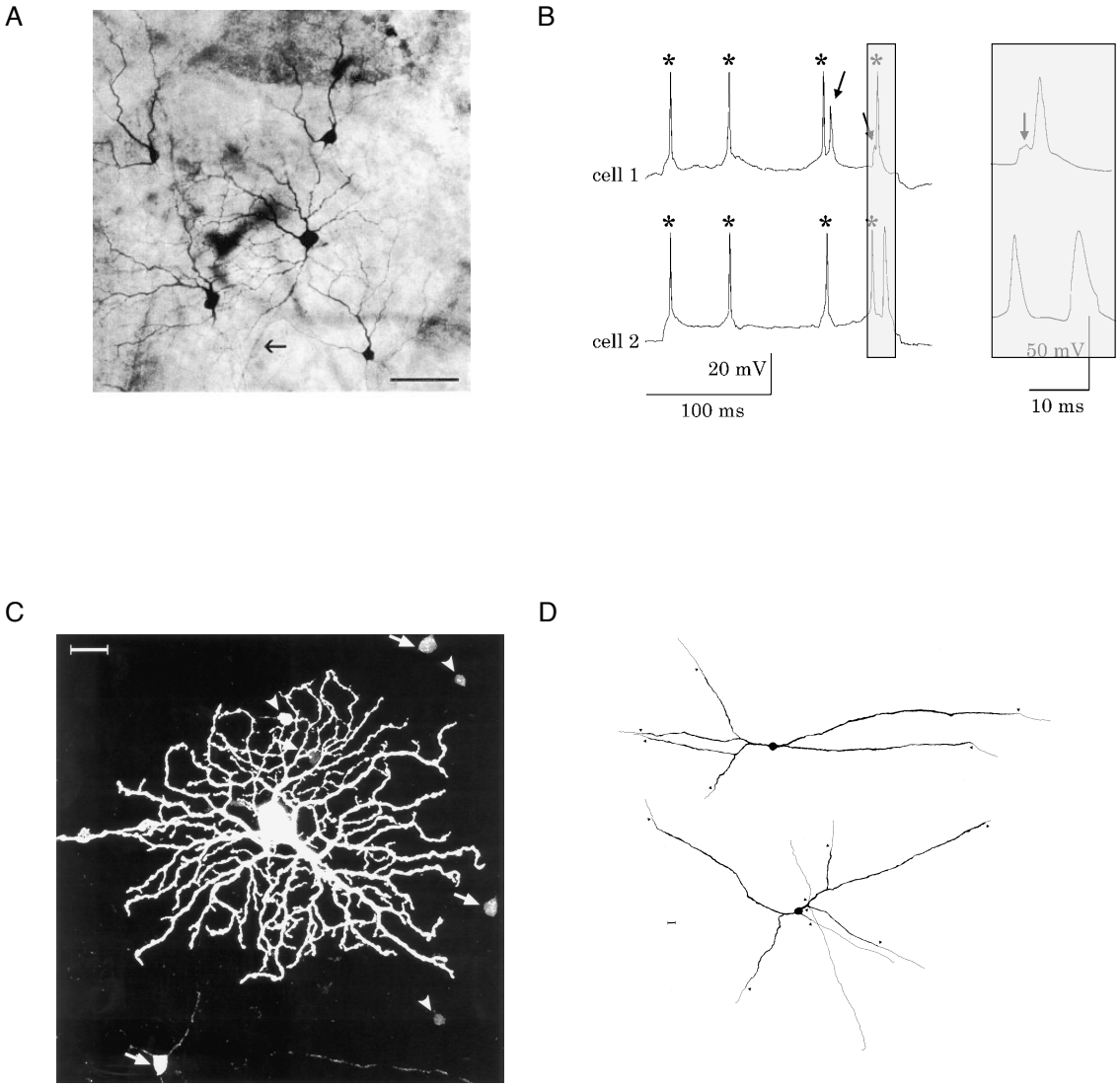

Figure 2.3: Tracer coupling between (A-B) homologous RGCs and (C-D) RGCs and amacrine cells. A) Neurobiotin injected into central α-ganglion cell in rat was taken up to by lattice of surrounding α-ganglion cells within its dendritic extent (scale bar, 100 μm). B) Dual recordings of two adjacent α-ganglion cells under chemical synaptic blockade. Astericks denote nearly simultaneous action potentials. Grey region is enlarged to highlight transient depolarization in one cell due to spike in second cell. (Figures adapted from [119]) C) Neurobiotin injected into ON parasol cell in primate was taken up by two morphologically distinct amacrine cell types labeled by arrows and arrowheads, respectively (scale bar, 25 μm). D) Camera lucida drawings of amacrine cells that indicated G6-gly immunoreactivity and co-localized with arrows in previous panel (scale bar, 10 μm). Note the long, polyaxonal structure indicative of a spiking amacrine cell [164, 284, 65] (Figures adapted from [130]).

evidence exists for the presence of gap junctions in the retina. These gap junctions provide a direct, although potentially rectified, electrical connection between individual cells. Gap junctions are composed of a family of protein subunits termed *connexins* [25, 24, 75, 110]. Within the connexin family, connexin-36 [55, 282] has been localized to α-ganglion cells [119, 262], AII amacrine cells [198, 94], photoreceptors and bipolar cells [95, 74]; the presence and location of other connexins in mammalian retina is of current, intense interest [112, 73, 180].

Further evidence for electrical coupling arises from examining the fine temporal structure of the cross-correlogram. The prevalence of narrow, bimodal cross-correlation (1-3 ms, species dependent) is interpreted as a reciprocal interaction where by one cell drives a spike in the second cell with a brief latency given by the time to each peak (Figure 1.1b, 2.1c). Bimodal cross-correlation has been observed in OFF α [125] and OFF brisk transient [77] ganglion cells in rabbit, ON and OFF Y cells in cat [181, 183, 184], ON parasol cells in primate (J. Shlens, F. Rieke; unpublished observations) and OFF cells in salamander [41].

As mentioned earlier electrical coupling can be consistent with reciprocal interactions as well as driving input[1], however the converse is not ambiguous: reciprocal interactions must be mediated by electrical coupling. Consistent with this hypothesis, pairs of cells exhibiting bimodal cross-correlation are resistant to chemical synaptic blockade in salamander [41] (but unexpectedly resistant to gap junction blockers), pharmacological blockade of the rod synapse using APB in rabbit [77, 79], and can mutually excite each other through extrinsic stimulation [125, 183, 119] (F. Rieke, C. Sekirnjak; unpublished observations). Also, the precise timing underlying synchrony persists in pairs of α-ganglion cells in spite of antagonists for chemical neurotransmitters [119]. The fact that two distinct shapes of cross-correlation exist (i.e. unimodal [41, 4] bimodal [77, 181,

[1]For instance, some forms of unimodal cross-correlation are resistant to chemical synaptic blockade [41] but abolished by gap junction blockers [4].

125]) suggest that gap junctions mediate coupling in several types of circuits.

Evidence presented thus far substantiates electrical coupling between homologous RGCs directly (Figure 2.2b) or through amacrine cells (Figure 2.2c). We now discuss individually evidence for each type of circuit.

2.1.1 Homotypic electrical coupling between RGCs

Homotypic electrical coupling has been suggested in several studies as a potential mechanism for correlated activity [125, 183, 119] (Figure 2.2b). In support of this hypothesis, neighboring α-ganglion cells in rabbit are more intensely and extensively labeled when Neurobiotin is injected in adjacent RGCs as opposed to amacrine cells [125]. Because amacrine cells are gap junction coupled and have large arborizations [32, 328, 33], if amacrine cells mediated electrical coupling, then one would expect that synchrony would extend beyond nearest neighbors in the mosaic. This was not observed in OFF brisk transient α-ganglion cells in rabbit [125]. Rather, synchrony was exclusively restricted to adjacent α-ganglion cells labeled with tracer [125]. This might reflect the fact though that amacrine cells are largely inhibitory and extensions to the receptive fields of RGC's only occur under proper visual stimulation [147]. Lastly, the observed width of the bimodal peak in rabbit α-ganglion cells is consistent with the latency observed between pairs of neurons known to exhibit direct electrical coupling in the inferior olive [169].

Additional evidence arises from studies in rat demonstrating that pairs of α-ganglion cells, which exhibit tracer coupling and synchrony, make gap junctions using connexin-36 at the intersections of their dendritic arbors [119]. This is the only mammalian species in which coupling between ganglion cells has been studied using anatomical techniques.

2.1.2 Electrical coupling mediated through amacrine cells

Several lines of evidence support the hypothesis that electrical coupling can be mediated through amacrine cells (Figure 2.2c,g). Tracer studies have consistently reported RGCs of a single morphological cell type coupled to several distinct amacrine cell types [65, 130, 107, 301, 302, 306, 328, 125]; furthermore, individual amacrine cell types homologously couple with each other [324, 301, 302].

Ultrastructural and immunolabeling studies have localized gap junctions [130, 119] and connexin-36 [119], respectively, to the intersection between the dendrites of RGCs and amacrine cells (presumptive amacrine cells in [119]). Furthermore, connexin-36 knockout mice lack the tracer coupling between OFF α-ganglion cells and amacrine cells observed in wild type mice [306] (see also [262]).

In several primate studies, two distinct types of amacrine cells (not AII amacrine cells [315, 130]) exhibited tracer coupling - one of which has been further studied [65, 130, 107]. This amacrine cell contained immunnoreactive glycine-extended cholecytokinin (G6-gly) precursor [177]. These cells are large polyaxonal cells described in previous tracer dye studies [65] and unistratified [37], "wispy" [174] and semilunar type 3 cells [154] described using Golgi methods (see Figure 2.3d). The polyaxonal amacrine cells that contain immunoreactive G6-gly are labeled when Neurobiotin is injected into parasol ganglion cells. In addition to making gap junctions with parasol cells, G6-gly-IR cells also make inhibitory chemical synapses on to ON parasol cells (see section 2.2.2).

Most of the evidence for the existence of electrical coupling mediated through amacrine cells does not exclude direct interactions between ganglion cells, however there is some suggestion

of this exclusivity in primate [65]. Specifically, (1) tracer dye spread from parasol cells to the ring of adjacent nearest neighbors but not to a second, outer ring of parasol cells, as might be expected through diffusion of the dye; (2) potential sites of coupling along dendrites have been observed between amacrine and parasol cells but not neighboring parasol cells and (3) the diameter of the amacrine dendritic tree approximates the range of RGCs that take up the dye. The observed latencies in bimodal, cross-correlation in certain types of rabbit RGCs appear slow for direct RGC interactions [77] (see also [41]).

2.2 Chemical synaptic input

Except for intensive ultrastructural studies, chemical synaptic input is harder to assay because no equivalent method to tracer dyes are known to elucidate circuits across chemical synapses yet (but see [320]). Different cells make stereotypic synaptic connections throughout the retina dictated by cell type and that these specific connections provide distinct, parallel pathways for visual information [96]. Although both excitatory and inhibitory chemical synapses are extensive in the retina and are critical for RGC light response [245], we focus our discussion on the role of chemical synapses in correlated activity.

Physiological evidence indicates that chemical synapses do mediate some correlated activity. First, anti-synchrony has been observed between cells of opposite polarity [181, 182, 184, 273]. Inhibition is a strong indication of chemical synaptic activity (but see [130]). Second, cell types that do not show tracer coupling exhibit synchrony such as X/β cells in cat [182, 301, 303] and midget cells in primate [65, 53] (see also [119, 77]; but see [124]). Third, pharmacological manipulations demonstrate that slower correlations are abolished or greatly diminished in the presence of chemical synaptic antagonists at the rod synapse [77] and complete chemical synaptic

blockade [41] (see Figure 2.1a), temporally shift in the presence of GABA antagonists [4] and are preserved in the presence of gap junction blockers [4]. These results do suggest that chemical synapses contribute to some forms of correlated activity.

Some observations of broad correlations are modulated in strength by the absolute level of light [182]. In particular, broad correlations strengthen and widen with stimuli in the scotopic range [182, 41]. In particular, at certain scotopic light levels, stimulus driven activity is entirely mediated through the AII amacrine cells which provide electrical and chemical synaptic input on to ON and OFF cone bipolar cells, respectively [93]. Correspondingly, at scotopic regimes selective inhibitory inputs into OFF α ganglion cells and excitatory inputs to ON α ganglion cells are highly correlated, a finding interpreted as divergence from an AII amacrine cell (F. Rieke & G. Murphy, personal communication).

Excitatory correlation or synchrony could be driven by excitatory drive or decrements of inhibition on to pairs of neurons. A decrement of inhibition would require chemical synaptic activity. Some observations of correlated activity are consistent with this possibility. In recordings from cat, quantum events at scotopic light level drive volleys of spikes in ON Y cells but periods of quiescence in OFF Y cells [182]. Some observed synchrony between pairs of OFF Y cells at scotopic light levels was a consequence of simultaneous periods of quiescence in pairs of OFF Y cells and likewise consistent with inhibitory drive on pairs of RGCs.

Ultrastructural studies with electron microscopy and immunostaining have demonstrated that 80% and 20% of synaptic input to peripheral ON parasol cells [130] and α-ganglion cells [317, 101, 153] come from amacrine and bipolar cells, respectively; this input arrives equally in proximal and distal dendrites. The proportion of synaptic input varies across retinal eccentricity and cell

type. For instance, 50% of synaptic input in cat X cells is from bipolar cells [319]. Parasol cells in parafoveal regions receive larger fractions of synaptic input from bipolar cells [157, 63, 179] (but see [82]). Because both cell types are in a position to drive correlated activity, we now discuss specific evidence that bipolar and amacrine cells drive correlated activity through chemical synapses.

2.2.1 Chemical synaptic input from the outer retina

The canonical circuit models the retina with a direct driving pathway from the photoreceptors through the bipolar cells to the RGCs [245]. From this perspective, one often thinks of light-driven activity as a funnel - the *convergence* of many photoreceptors down to a single RGC [131, 245], whose width is determined by retinal eccentricity and the size of the dendritic arborization [310, 152]. At first glance, this perspective suggests that shared input from photoreceptor or bipolar activity can not mediate correlated activity. However, to truly address such a question, one must examine the *divergence* or lateral spread of light-driven activity in the outer retina (Figure 2.2d,e,f,h).

For example, several mechanisms laterally spread light-driven activity in the outer retina. First, rod photoreceptors are electrically coupled to adjacent photoreceptors in cold-blooded vertebrates [88, 76] and to adjacent cones in primates [255, 256] (Figure 2.2e). Second, horizontal cells provide lateral inhibition between cones and rods and might act as a mechanism for anti-correlation [245] (Figure 2.2h).

Despite the prevalence of convergence along the visual pathways in the retina, divergent circuitry at each stage does provide a second circuit capable of generating correlated activity (Figure 2.2d,f). For instance, ultrastructural studies have demonstrated that a single S cone provides

input on to 4 ON bipolar cells [253]. Divergence from bipolar cells on to RGCs is likewise possible (Figure 2.2f) (but note that mammalian bipolar cells are non-spiking [140]). Midget bipolar cells synapse on to more than one midget ganglion cell [138] (also see [152]) and each S cone ON bipolar cell synapses onto two BY ganglion cells [253].

Unfortunately, systematic evidence for divergence is lacking and mostly suggestive based on dendritic coverage factors within each RGC type as well as the number of known RGC types. Assuming a single bipolar cell synapses uniformly onto a contiguous spatial region of one lamina of the IPL [245, 310], then the number of cells it would project to would be dictated by the dendritic coverage factor of each RGC type. A coverage factor of 3 would imply that a single bipolar cell would synapse potentially on to 3 RGCs of the same type plus any other RGC types that synapse at that layer. For example, primate midget and parasol RGCs have coverage factors of 1.0 and 3.0, respectively [65, 66], while cat α and β cells have coverage factors of 1.5 and 3.0, respectively [311, 313]. Consistent with this fact, cat X cells exhibit stronger broad correlations than cat Y cells [182].

2.2.2 Chemical synaptic input from amacrine cells

Because of their anatomical position, amacrine cells are well-situated to perform complex visual processing including extra-classical receptive fields, object motion sensitivity and other forms of adaptation [18]. Although amacrine cells provide a majority of synapses in the primate IPL [155], the distribution of amacrine cell types synapsing on to RGCs is unknown. Amacrine cells are the most diverse cell type in the retina comprising roughly 30 distinct morphological types [171, 172]. Yet, only three known amacrine cells have been identified thus far to synapse on to ON parasol cells: G6-gly-IR amacrines, cholinergic starbust amacrines and GABA-IR amacrine

cells [130]. Notably, no individual amacrine cell type dominates in rabbit retina [171], although given the unique dominance of a few RGC types in primate retina, the distribution of amacrine cell types might differ [174].

Although the function of a few specific types of amacrine cells is well known (e.g. [116, 151]), in general the function of amacrine cells is poorly understood [18]. By default, amacrine cells are considered inhibitory interneurons [171] but both excitatory and inhibitory synaptic input have been identified: starburst amacrine cells provide cholinergic input onto ON parasol cells [175, 247, 130] while GABA-IR amacrine cells provide GABA input onto parasol cells in primate [156, 130] (see also [35]). In rabbit though, the application of cholinergic blockers failed to reduce the strength of observed fast correlations suggesting that cholinergic pathways might not be involved in correlated activity [77] (but see [4]).

Very little is known about the divergence of single amacrine cells onto RGCs. The size of amacrine cell dendritic arborizations are the primary guide for determining the potential divergence from individual cells. In rabbit, most amacrine cells have been systematically classified by the size (and lamina) of their dendritic fields, the largest family termed *wide-field* have arborizations $> 400\mu m$ [171, 172]. Amacrine cells with multiple axon-like arbors, termed *polyaxonal*, have been identified in salamander [329, 58], mouse [164], rabbit [31, 32, 290, 305, 90, 91, 92], ferret [3] and primate [284], are known or presumed to generate action potentials (for review, [164, 34]) and thus can potentially mediate temporally precise correlation on large spatial scales (Figure 2.2g). For instance, in the primate retina at least two polyaxonal amacrine cells have been identified [284, 130, 65], both of which electrically couple with RGCs (Figure 2.3c). Elucidating the role of amacrine cells and their neural circuitry will be a topic of future efforts [171].

2.3 Miscellanea: other potential mechanisms

We remark on other potential mechanisms that might give rise to correlated activity. Although evidence for these mechanisms is weak, we note them for completeness and refer the reader to other references as needed.

Centrifugal fibers from the brain to the eye. These fibers have been documented in fish, amphibians, birds, reptiles and several mammalian species [43, 241]. In order for this mechanism to underlie correlated activity, the response latencies must precisely match the observed correlation time scale, which would be quite "fortuitous" [183]. Notably, all varieties of synchrony observed in vivo [184, 204] have also been observed in vitro [77, 41, 273] except for long range correlated activity [204].

Non-synaptic mechanisms. The output activity of multiple cells might become correlated through ionic current flow through a constricted extracellular space, termed *ephaptic coupling* [134, 85]. Non-synaptic mechanisms have been identified as a potential source for coupling of neighboring, tightly packed cells in the hippocampus [84, 249, 122, 111]. Consistent with this mechanism is the role distance plays in determining the strength of synchrony. One difficulty with this type of mechanism is resolving the fact that opposite polarity RGCs overlap in visual space but exhibit anti-synchrony (for more discussion, see [182]).

Chemical synapses between ganglion cells. Only one observation of this mechanism has been reported in catfish [252]. Although it is possible that chemical synapses exist in other species, ultrastructural studies have not reported such evidence in mammalian species such as primate and cat [153, 101, 130].

2.4 Summary

We have surveyed evidence for potential mechanisms and circuits that might give rise to correlated activity. In particular, we have reviewed evidence describing how specific RGC types are electrically coupled to homologous RGCs and certain types of amacrine cells (Figure 2.2b,c). In addition, we have discussed the range of circuits that provide chemical synaptic input including bipolar and amacrine cells (Figure 2.2c-h).

Finally, we emphasized that while we did manage to describe many biophysical mechanisms, we purposefully avoided an operational interpretation (e.g. reciprocal vs. driving input). The difficulty of interpreting the operation of a circuit was discussed in regard to amacrine circuitry (Section 2.1.2) but likewise extends to other circuits (e.g. electrical coupling might provide inhibition through rectification [130]). More research and a better understanding of the role of individual cell types, especially amacrine cells, eventually will shed more light on these issues.

This chapter is taken from J Shlens and EJ Chichilnisky, (2007) *Synchrony and concerted activity in the neural code of the retina.* In RR Hoy, GM Shepherd, AI Basbaum, A Kaneko and G Westheimer (ed). **The Senses: A Comprehensive Foundation**, Elsevier Press.

Chapter 3

Observed correlated activity between retinal ganglion cells

Whereas the previous section focused on elucidating *mechanisms* of correlated activity, we now focus on what *forms* of correlated activity have been observed. Again, our discussion is strongly influenced by notions of retinal organization of RGCs and this is particularly reflected in our discussion of cross-correlations between pairs of cells. We continue this section by highlighting the distinction between pairwise and multi-neuron correlated activity with the goal of examining what *should* multi-neuron activity look like given observed synchrony between pairs of neurons. We find that this leads to a natural prediction of multi-neuron activity described by the *Ising model* - the least structured model consistent with observed correlations. The success of this class of models is quite striking - accurately predicting activity in hundreds of neurons [296, 274], providing strong inferences about the underlying neural circuitry [273, 274] and exhibiting unexpected behavior only evident at large scales [259, 296].

3.1 Mosaic structure dictates pairwise correlation structure

The most prominent feature of cross-correlograms is the variation of the sign and magnitude of correlation across pairs of RGCs, evident in Figure 1.1 and 2.1. The goal of this section is to demonstrate that variation in correlation strength can be understood in the context of the known layout and architecture of RGCs in the retina. Pioneering studies by Brian Boycott and Heinz Wässle demonstrated that the dendritic arborizations of individual types of RGCs tile the retina independently (reviewed in [310]). Implicit in this observation is that the circuitry underlying RGCs should be regular and uniform across populations of RGCs within a single cell type and might be reflected in the correlated activity.

The strength of correlated activity within a single cell type systematically depends on the distance between pairs of cells within a mosaic of RGCs. In Figure 3.1, we plot as ovals the receptive field outlines of 118 ON parasol cell (see [52] for details); the location and size of the RF outlines indicates the soma location and size of the dendritic arborization [310]. Below this mosaic are the cross-correlograms for a single ON parasol cell with three other ON parasol cells of varying distance in the presence of constant photopic illumination. Note that all pairs of cells exhibit synchrony whose magnitude varies depending on the distance separating pairs of cells. We can calculate an index that measures the relative frequency of synchronous events to the amount of synchrony expected by chance within the central ± 5 ms (for details, see [273]); this index essentially measures the height of the central peak relative to the baseline rate. The synchrony index plotted versus distance between pairs of ON parasol cells indicates that synchrony is spatially localized within a single cell type, systematically depends on distance between pairs of cells and is universal among all cells of the same type (see also [77, 181]). Universality means that

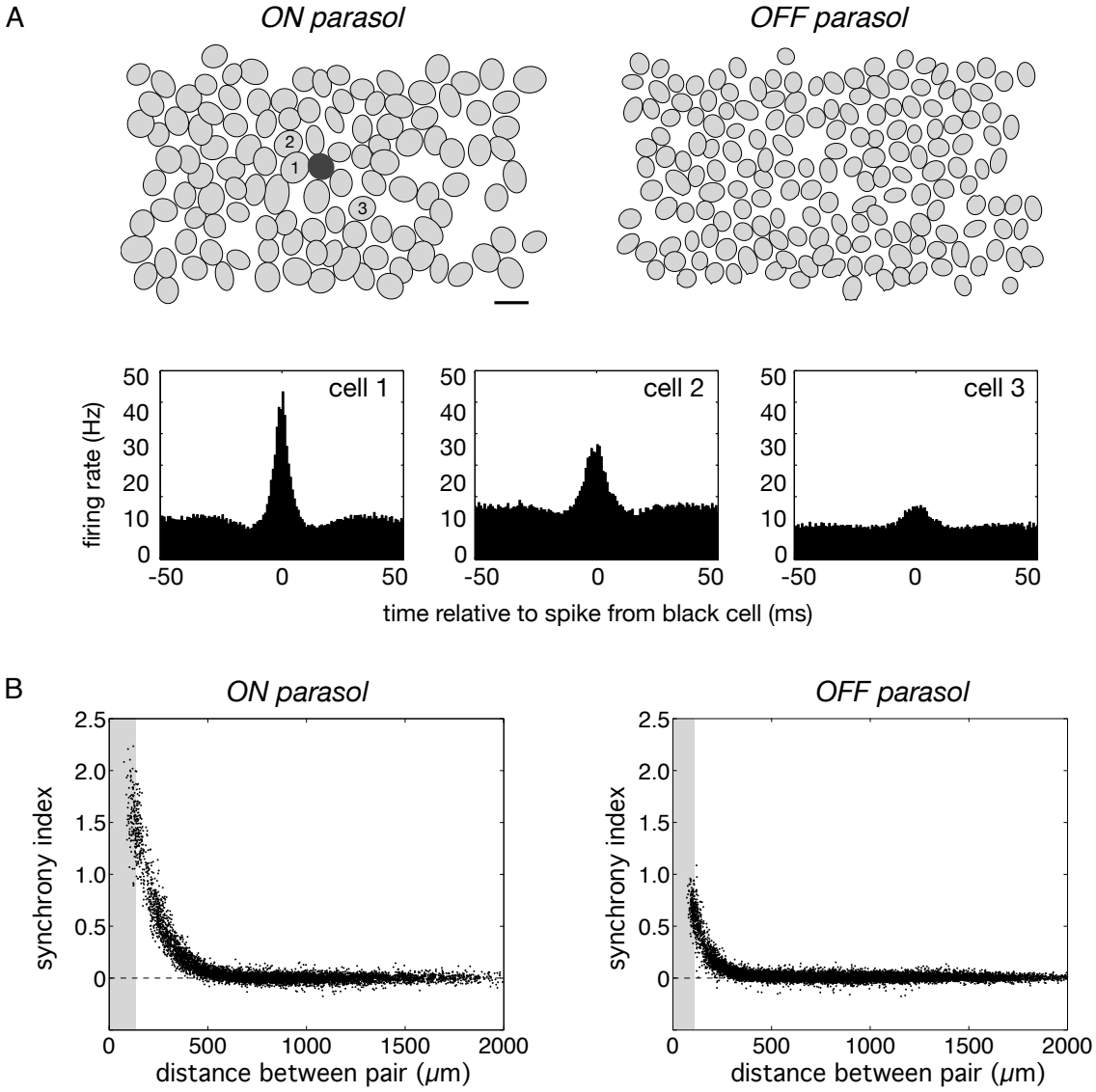

Figure 3.1: Systematic and universal pairwise correlations as a function of distance. A) Mosaic of ON parasol cells with ovals represent 1 SD of Gaussian fits to receptive field profiles. Scale bar is 200 μm. Three sample cross-correlograms between the black cell and numbered cells. Synchrony index [273] measures the strength of synchrony: 1.60, 0.95, 0.54, respectively. B) Strength of synchrony plotted versus distance between pairs of receptive field centers. Vertical grey bar denotes the modal distance between adjacent neighbors within the mosaic. Note that synchrony extends beyond adjacent neighbor region. Figure adapted from [273].

the strength of synchrony is solely dictated by the relative locations of the two cells, indicating that the circuitry underlying correlated activity is uniform across a mosaic of a single cell type.

Multiple RGC types, each receiving distinct input [96], tile the retina independently, suggesting that correlations across different cell types differ depending on the types of cells constituting a pair. This is evident in pairs of OFF parasol cells in Figure 3.1. All pairs of OFF parasols exhibit synchrony in the cross-correlograms but the strength of synchrony is systematically weaker then pairs of ON parasol cells. Conversely, the cross-correlograms between mixed pairs of ON and OFF parasol cells exhibit anti-synchrony. We emphasize that this is not light driven but is intrinsic to the circuit. Again, note that the strength of anti-synchrony systematically and universally depends on the distances between each pair of cells within their respective mosaics (Figure 3.1).

The correlated activity for primate parasol cells is similar to reports of correlated activity in higher mammalian species. Specifically, across species synchrony has always been observed in pairs of cells of the same type that are nearby, while statistical independence (or lack of correlation) is usually observed in pairs of cells separated by large distance [181, 77, 125, 273, 191]. Conversely, in several species pairs of cells of the same type but opposite polarity (e.g. ON and OFF parasol cells) often exhibit anti-synchrony between nearby pairs but statistical independence between pairs of cells far apart [181].

These general statements are not universal as pairwise correlations have been observed on occasion between pairs of cells separated by large distances in vivo in the anesthetized cat [203, 204] and frog [129] and implicitly in gross electrode recordings along the optic nerve [6, 5, 160]. In particular, in the presence of a strong stimulus with contiguous spatial structure, one group found that individual RGCs phase-locked oscillating at 80-90 Hz [203, 204]. Unfortunately, these

observations have yet to be replicated in vitro [273, 77, 125, 4, 206, 239] and in vivo [181, 182, 183] (but see [129]). Although these observations are rare (see [204] for review), these results do suggest that with appropriate stimulus manipulation, long range correlated activity might be generated in the retina (for implications, see [285, 148, 129]).

3.2 Pairwise vs. Multi-neuron correlation

The last few decades of research has heavily relied on cross-correlations to examine the interactions between pairs of neurons. Cross-correlation analysis is limited, however. Because cross-correlograms solely focus on the activity of two neurons, it averages over the sea of activity in which a pair of neurons is immersed, ignoring distinct patterned activity indicative of the complete neural circuit. Because this distinction can be subtle, we build an intuition for what multi-neuron correlations look like and finally arrive at a precise definition of this activity.

Consider three recorded RGCs from the salamander in Figure 3.2a [261]. There exists precise synchrony between pairs of neurons as demonstrated by the cross-correlograms. However, a visual inspection of a section of the spike trains highlights that many of the synchronous events between two neurons are actually subsets of all three neurons firing. How do we measure or represent the timing of firing patterns across three neurons? One possibility is to compute a triplet cross-correlogram (Figure 3.2b). This is a measure of triplet synchrony as a function of time shifts in two of the three neurons; the prominent central peak reflects the preponderance that three neurons fire nearly simultaneously, and the ridges reflect the fact that two of the three neurons fire synchronously regardless of the spike time of the third neuron. The complexity of the triplet cross-correlogram suggests that looking for features in the relative timing is difficult (but see [228]). Furthermore, extending this analysis to a larger number of neurons seriously complicates this

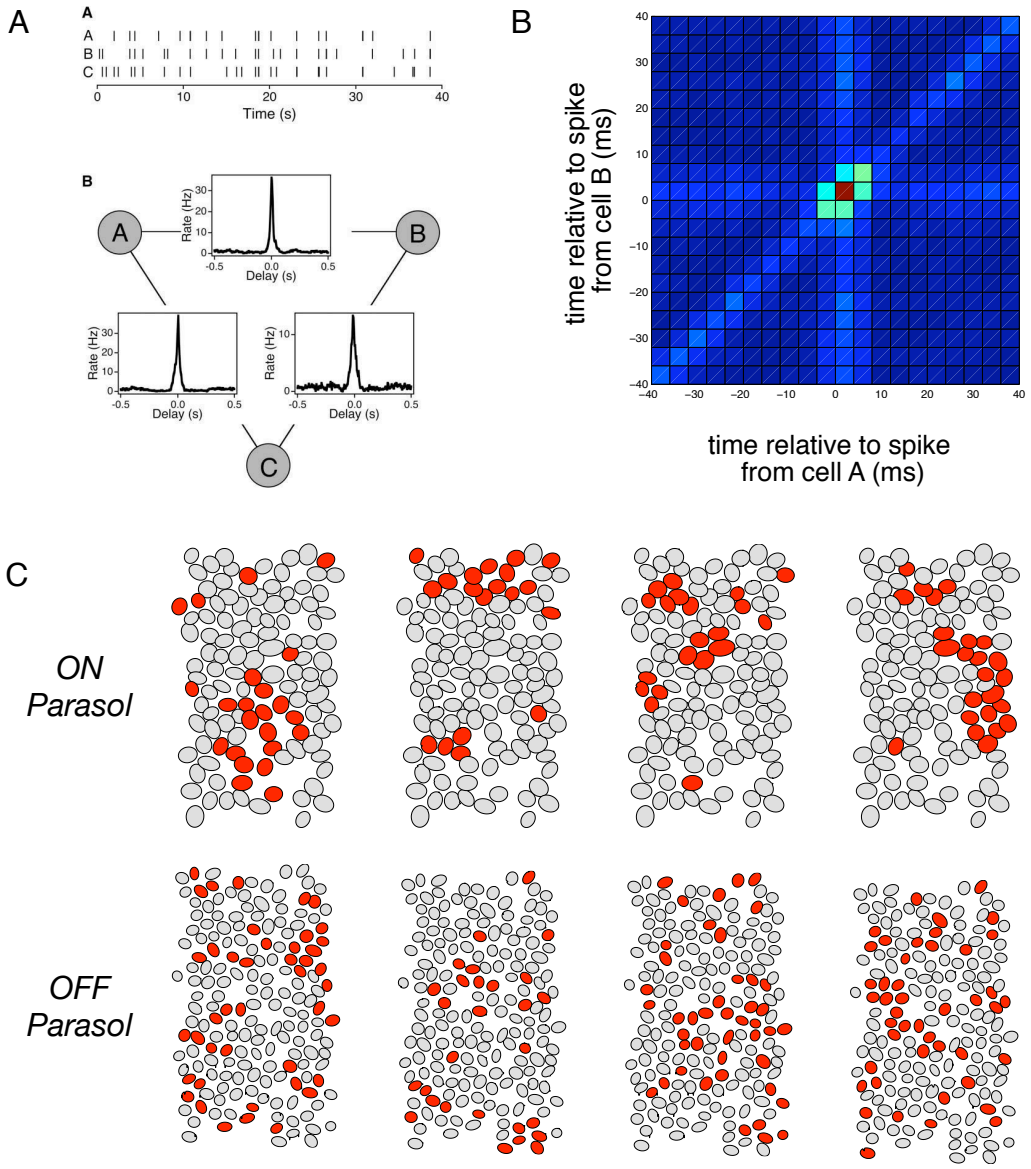

Figure 3.2: Hints of higher order correlations. A) Simultaneous recordings of three salamander RGCs. Each pair of cells are highly correlated (bottom) yet multitudes of pairwise synchrony occur when all three cells spike [261]. B) Triplet synchrony cross-correlation function with a bin size of 5 ms. Note the prominence of three cells firing simultaneously. C) Multi-neuron firing patterns (within 10 ms time bin) of ON and OFF parasol cells. Figure adapated from [274].

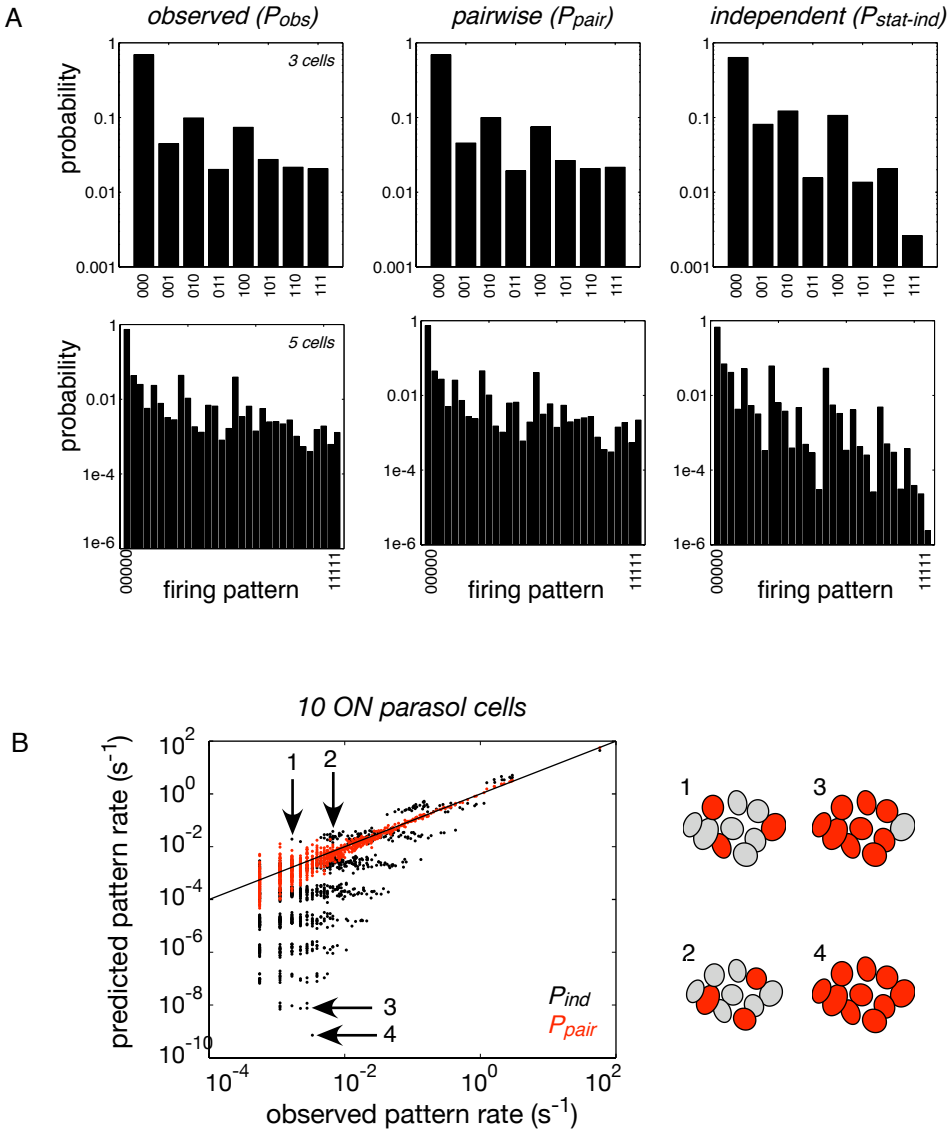

Figure 3.3: Multi-neuron firing pattern distributions. A) Top row: observed, pairwise and statistically independent firing pattern distribution (left, center and right, respectively) for 3 adjacent neurons. X-axis indexes simultaneous binary firing patterns (see text). Bottom row: same for 5 neurons. B) Probability of observed firing patterns, expressed as rate (s^{-1}), plotted versus probability predicted from statistical independence (black) and pairwise (red) distributions for mosaic of 10 ON parasol cells. Each dot is a single firing pattern; solid line represents equality; each strata of points corresponds to all firing patterns with a particular number of neurons firing (see examples on right). Statistical independence provides poor prediction of observed firing patterns, while accounting for pairwise synchrony, vastly improves the prediction to within the dispersion due to counting statistics. Figure adapted from [273].

visualization. That said, the center of the triplet and pairwise cross-correlograms do demonstrate that much of the interactions between neurons does occur *simultaneously*. Hence, for the rest of the following sections, we simplify matters by solely examining the simultaneous behavior of RGCs and return to relative timing issues in Section 4.3.2.

We can visualize the spatial structure of simultaneous multi-neuron firing patterns by examining how correlated activity is reflected in the mosaic structure of a single population of neurons. In populations of primate ON and OFF parasol cells, we observe moments of time where large, spatially contiguous groups of neurons fire simultaneously ($\pm$ 5ms) in the presence of constant illumination (Figure 3.2). These snapshots of activity demonstrate that observed synchrony between pairs of cells is a subset of larger patterns of concerted activity. Furthermore, these large patterns of activity are dictated by the cell type and spatial layout of individual cells. In salamander, for instance, it is estimated that up to 7 neurons participate in firing events which account for up to 50% of all spikes recorded [261]. Thus, understanding the structure of correlated activity requires examining the behavior of large numbers of neurons.

Examining simultaneous activity (as opposed to spatio-temporal patterns) permits a complete characterization of all firing patterns by tallying the relative frequency of each observed firing pattern. Each firing pattern can be expressed as a binary string (e.g. 10010) where a one (zero) denotes the presence (absence) of a spike for each neuron within this brief period of time (e.g. 10 ms). The number of observations of each firing pattern normalized by the total number of observations over a long experiment provides a measure of the observed firing pattern distribution.[1] We call this the observed firing pattern distribution p_{obs} and across n neurons it consists of all 2^n

[1] We assume that each firing pattern observation is independent of previous patterns and this neural system is fixed and stationary over the course of the experiment. This is formally termed independently and identically distributied (*i.i.d.*) data.

firing patterns (Figure 3.3a, left). As can be observed in Figure 3.3, triplet synchrony occurs at roughly the same rate as two neurons firing simultaneously, matching observations in salamander (Figure 3.2a). Our goal in the following section is to account for this observed activity.

3.3 Accounting for multi-neuron activity

The firing pattern distribution p_{obs} describes the simultaneous behavior of multiple neurons and any characterization of these neurons must predict the relative frequency of observing each firing pattern. Developing a parsimonious model to explain this activity has proven difficult (e.g. [189, 261]) because any prediction of a single multi-neuron firing pattern must take into account interactions amongst all neurons.

Statistical independence provides a standard model for comparison to the observed firing pattern distribution p_{obs}. For example, the probability that 3 or 5 cells fire synchronously is exceedingly small given the individual firing rates and the assumption of statistical independence (Figure 3.3a,c, far right bar). Thus, a model based on statistical independence provides a poor prediction for the probability of observing firing patterns with many neurons firing. This discussion can be made precise. Let us call $x = \{x_i\}$ the simultaneous firing pattern across n neurons. The firing pattern is a binary string (e.g. $x = 101$) as described previously (Seciton 3.2). The probability of observing a binary firing pattern x assuming statistical independence[2] is

$$p_{stat-ind}(x) = \prod_i^n p_i^{x_i}(1-p_i)^{(1-x_i)}$$

where $p = \{p_i\}$ are the individual firing rates expressed as probabilities. We term the distribution

[2]Since we are introducing our notation, a brief note is warranted for clarity: $p(X)$ denotes the probability distribution of the random variable X, while $p(X = x)$ denotes the probability that $X = x$. For convenience we sometimes abbreviate the latter as $p(x)$, where X is implied.

$p_{stat-ind}$ a type of *null model* that assumes statistical independence and the predictions of this null model for all firing patterns can be seen in Figure 3.3a, right column. Note that we can precisely test whether statistical independence is a good model by comparing the two distributions $p_{stat-ind}$ and p_{obs}.

Apriori we expect statistical independence to fail to predict the observed firing pattern distribution because we know that synchrony exists. Synchrony, by definition, is the observation of deviations from statistical independence (see Section 3.1). In fact, this expectation can be verified by visually comparing $p_{stat-ind}$ and p_{obs} across all firing patterns (Figure 3.3a). Thus, a more appropriate null model is to predict the firing pattern distribution given that synchrony is observed between pairs of neurons.

To gain a better understanding of this statement, we discuss a didactic example. Consider the observed firing pattern distribution p_{obs} of three neurons. Pretend that we had instead recorded from two out of three neurons at a time. For each pair of neurons we would measure the degree of synchrony in the pairwise distribution quantified by three pairwise distributions: $p(x_1,x_2)$, $p(x_1,x_2)$, $p(x_2,x_3)$. The goal we now wish to achieve is to make a prediction of the complete firing pattern distribution $\hat{p}(x)$ from these pairwise distributions. We emphasize that the sole requirement of the prediction $\hat{p}(x)$ is that it contains the same degree of synchrony between each marginal pair of neurons (e.g. $p(x_1,x_2) = \sum_{x_3} \hat{p}(x)$). It has long been known that this problem is under-constrained[3] and an infinite number of distributions (including p_{obs}) can satisfy this requirement. How we select such a distribution $\hat{p}(x)$ is the subject of the following section.

[3]For the case of 3 neurons, this problem can be recast in statistical mechanics terms. We wish to predict the $N+1$ body correlations from the N body correlations. In this situation, triplet synchrony has elevated status when the pairwise distributions $p(x_1,x_2), p(x_1,x_2), p(x_2,x_3)$ are known. Triplet synchrony effectively measures the 3-body *connected correlation* in the statistical mechanics literature. The frequency of triplet synchrony paired with pairwise distributions are sufficient to reconstruct the entire 3 neuron firing pattern distribution. This notion is general for constructing the $N+1$-body distribution from the $N+1$ body correlation and the N-body distributions [30].

3.4 Using maximum entropy techniques to predict multi-neuron activity

Intuitively, our goal is to select a distribution for multi-neuron activity $\hat{p}(x)$ consistent with all pairwise distributions but assumes no prevalence of additional structure. This distribution provides a suitable null model that accounts for observed synchrony and can be compared against the observed distribution p_{obs}. One strategy borrowed from statistical mechanics [132, 133] and commonly employed in machine learning [26] is to select a distribution that obeys pairwise constraints but maximizes the entropy:

$$\hat{p}(x) = \arg\max_{p(x)} \left[H[p] + \sum_{i=1}^{N} \lambda_i (E[f_i(x)] - k_i) \right] \tag{3.1}$$

where $H[p] = -\sum_x p(x) \log_2 p(x)$ is the entropy of a distribution $p(x)$ and λ_i are Lagrange multipliers enforcing selected constraints $E[f_i(x)] = k_i$. There exists a closed form solution for the maximum entropy distribution although the Lagrangian multipliers must be estimated numerically.[4] Since entropy is a measure of randomness in a distribution, the maximum entropy distribution corresponds to selecting a distribution that matches measured synchrony between pairs of neurons but is otherwise least structured [8, 258, 178].

Example. If the selected constraints solely enforce single cell firing rates, then we recover the statistically independent distribution p_{ind}. Hence, maximum entropy is a generalization of statistical independence.

[4]The maximum entropy distribution is unique, concave everywhere and calculated using standard constrained maximization techniques such as gradient ascent [173] or iterative techniques [26]. Each constraint $E[f_i(x)] = k_i$ is a linear function of the observed distribution p_{obs}. For example, one constraint on synchronous activity between neurons x_1 and x_2 might be $p_{obs}(111) + p_{obs}(110) = p(x_1 = 1, x_2 = 1)$, where $f_i(x)$ is the sum of the two selected entries from the observed distribution and $k_i = p(x_1 = 1, x_2 = 1)$.

If the selected constraints enforce all pairwise correlations, then we generate a new null model, p_{pair}. The null model provides a prediction for multi-neuron firing patterns from pairwise correlations. By selecting non-redundant constraints, grouping Lagrangian multipliers, and relabeling an absence of a spike as -1, one can re-express p_{pair} as

$$p_{pair}(x) = \frac{1}{Z} \exp\left(\sum_{i=1}^{n} h_i x_i + \frac{1}{2}\sum_{i\neq j} J_{ij} x_i x_j\right) \tag{3.2}$$

where h_i and J_{ij} are the renamed Lagrangian multipliers and Z is a normalization constant (or partition function [126]). Again, we note that $\{h_i, J_{ij}\}$ must be estimated numerically from data. This distribution is recognized as an Ising model [258] (see also [62]), a type of Markov random field [137]. The Ising model is the distribution that is the least structured distribution consistent with observed correlations between pairs of neurons. This distribution holds special prominence in several research domains: in basic statistical mechanics, Ising models provide an accurate description of equilibrium dynamics in physical media such as magnets [126]; in condensed matter physics, Ising models are a common system for exploring phase transitions [30, 108]; in computer science, Ising models are tractable representations of functional dynamics in neural networks [121, 123]; in statistics Ising models are a discrete, undirected Bayesian network [137]. Thus, by accounting for pairwise interactions, the resulting null model is a well recognized and well studied distribution [10, 126].

3.5 Measuring the success of pairwise models

Accounting for synchrony between pairs of neurons provides an accurate account of multi-neuron firing patterns. In the example of 3 and 5 neuron groups in Figure 3.3a, the entire firing

pattern distribution is predicted by calculating the maximum entropy distribution consistent with pairwise correlations (Figure 3.3a, middle column) [273]. The pairwise distributions look qualitatively similar to the observed distribuion. Likewise, the majority of the systematic deviations from statistical independence from 10 neuron firing patterns are rescued by accounting for pairwise correlations [259] (Figure 3.3b). On a quantitative level, the result shows that a firing pattern, although living in 2^n dimensional space, can be approximated with a parsimonious number of parameters given by the number of pairwise measurements n^2. In essence, we have performed dimensional reduction by approximating the distribution with pairwise correlations. On a network level, this result intonates that perhaps a more simple circuit could account for large scale activity (see Section 3.6.3).

The success of these null models can be quantified using an average likelihood analysis or equivalently an information theoretic analysis [258, 273]. In essence, these quantities measure how probable it is that a proposed null model p_{model} could give rise to an observed distribution of firing patterns p_{obs}. The Kullback Leibler divergence $D_{\mathrm{KL}}(p_{obs} \,||\, p_{model})$ provides such a measure quantified in bits (see Appendix A.7). If we denote $D_{model} \equiv D_{\mathrm{KL}}(p_{obs} \,||\, p_{model})$, then D_{ind} measures the total deviations in the observed distribution from from statistical independence [273]. In essence, D_{ind} is a cross-validated form of multi-information [258]. A natural measure of success is to ask what fraction of the failures of statistical independence are rescued by a particular model: $1 - \frac{D_{model}}{D_{ind}}$. In the case of primate retina, 99% of the noise correlations in up to 7 neurons are rescued [273] while in salamander and guinea pig 90% of stimulus and noise correlations in up to 10 neurons are rescued [259]. Hence, solely accounting for synchrony between pairs of neurons provides an accurate representation of multi-neuron patterns across species.

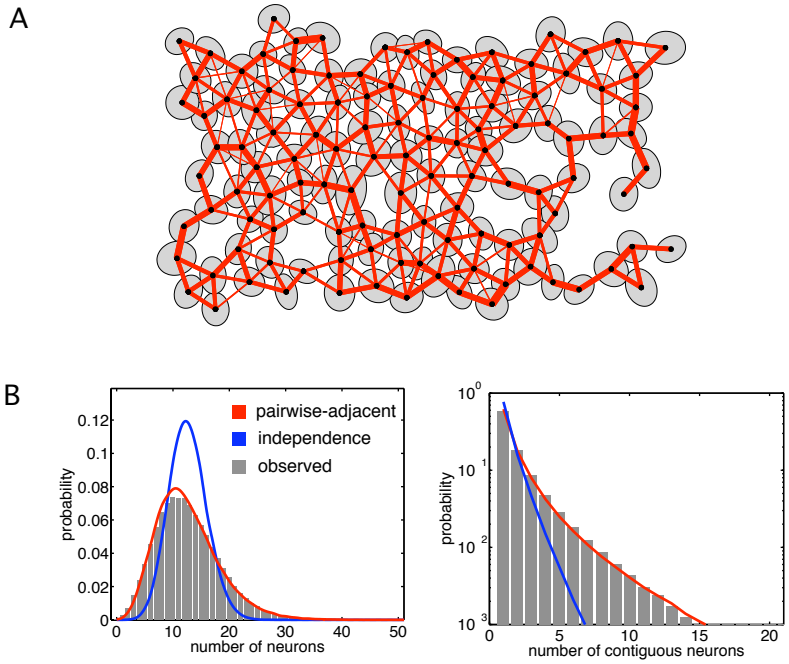

Figure 3.4: Ising models of large scale firing patterns. A) Visualization of nearest neighbor Ising model (or pairwise-adjacent maximum entropy model); thickness of red lines corresponds to strength of coupling terms between RGCs (see Equation 3.2). B) Nearest neighbor Ising model predicts the distribution of the number of neurons firing and the number of contiguous neurons firing across populations of 118 ON parasol cells. For comparison, statistical independence based on individual firing rates (blue).

3.6 Explorations of large-scale activity

The spatial scale of firing patterns (Figure 3.2) requires examining whether we can likewise explain larger scale activity in a population of neurons. Intuitively speaking, one would suspect that as we look at larger numbers of neurons, we would expect that patterned activity should become increasingly difficult to explain with statistical independence. Indeed, this has been quantified and independently reported in primate, guinea pig and salamander [273, 259, 296]. Accounting for this correlated activity with pairwise correlations however becomes technically more difficult as estimating and validating a pairwise model becomes more difficult. Estimating the parameters of the Ising model $\{h_i, J_{ij}\}$ becomes more difficult because the number of parameters which must be fit grows quadratically [327, 120, 224] . More vexing, however, is the fact that lim-

ited recording times and counting statistics systematically detriment the ability to quantitatively assess the success of the model. The former can be overcome by resorting to extensively developed Monte Carlo techniques in the Ising model literature [288, 322]. The latter problems can be overcome by examining other statistical features of the firing pattern.

3.6.1 Characterizing large-scale activity

Mechanisms such as wide-field amacrine cells [171, 172] suggest the possibility that correlations can propagate over long distances in the retina [203]. Thus, although we have discussed firing patterns patterns in $n \leq 10$ neurons, it is unclear how far, numerically and spatially, correlations spread. For instance, the firing patterns in Figure 3.2 provide signs of this spatial and numerical scale of correlated activity, although this is restricted to one of approximately two dozen cell types in the primate retina [67]. Although techniques for recording from large numbers of neurons are coming online [166, 266, 128], it is difficult to record long enough to accrue accurate statistics on firing patterns for $n > 10$. We must resort to examining statistical features of the distribution which are better approximated.

For instance, we can ask what fraction of total and spatially contiguous neurons fire simultaneously. This distribution measures the numerical and spatial scale of synchronous events in the primate retina. In the presence of constant illumination noise correlations cause an average of X% of the 118 ON parasol cells to fire; on average, these neurons fire in spatially contiguous groups of X neurons within 10 ms. Furthermore, over 99% of the synchronous events involve less than X% of the cells and are comprised of less than X spatially contiguous groups of neurons. If one assumes that a mechanism underlying this activity is exctitatory, this spatial and numerical scale bound the range of effective divergent circuitry.

A second statistical feature one can examine is the entropy of the distribution to examine how variability scales in the aggregate activity of population of neurons. A well known difficulty with this approach is that entropy is difficult to estimate in finite data for large distributions (i.e. large n) [214, 202]. Thus, an approach taken by [259] is to extrapolate the expected behavior of the entropy at large n where the extrapolation is based off of known scaling behavior in Ising models [150, 192]. Although this extrapolation necessarily fails at large n, this trend highlights the fact that pairwise correlations when taken together can dramatically reduce the number of allowable firing patterns in a distribution. One prediction is that in large populations of neurons, there exist an effectively limited set of firing patterns that the populations of neurons can express, although it is unclear how much of these reported correlations reflect the circuit or the strongly correlated stimulus [259]. One implication of this result is that because large scale firing patterns are so stereotyped, multi-neuron correlations might provide an ability to error check the coding of visual information [72, 259]. Hints of this phenomena have been observed in further work that identified families of firing patterns, corresponding to basins of attraction that consistently reappeared across multiple stimulus presentations [296].

3.6.2 Signatures of a critical point

A second line of questions is to ask whether the strength of correlations have been optimized by the biology for some purpose. In particular, does the large-scale activity of the retina represent a system organized to maximize information transmission? The one term that is missing from the Ising model (Equation 3.2) is the temperature T, a free parameter that scales the "energy" term inside the exponential. Implicitly, for the pairwise model fit to the observed multi-neuron firing patterns, the temperature is $T = 1$.

One study measured how artificially manipulating the temperature by scaling all parameters by this constant effect the variability of the network of neurons [296]. This study measured the specific heat as a function of temperature and observed that a sharp peak exists at $T = 1$ and this peak sharpens as larger numbers of neurons are examined. This sharp peak in the curve suggests that the system might be poised at a critical point. Signatures of critical points have also been observed in the power law distribution of avalanches of spontaneous neural activity in cortical slices [22, 23]. Theoretical work has suggested that critical points might be optimal for information transmission [22, 149, 296] because systems poised at critical points can dynamically maximize their range of responses to stimuli of varying amplitudes and likelihood [149, 296]. Whether the correlated activity of the retina reflects this optimality will be the subject of future investigation.

3.6.3 Inferring neural circuitry

The observation of patterned neural activity provides strong clues about the underlying neural circuitry. This sentiment permeates our discussion of the structure of pairwise activity (Section 3.1) and serves as a strong motivation for even investigating correlated activity [181, 182, 183]. We ask whether structure within multi-neuron correlations provides any clues about the identify of the underlying neural circuit.

Consider a relatively simple mechanism that provides reciprocal interactions between adjacent RGCs within a mosaic (Figure 2.2b,c; see Section 2). Such a neural circuit could generate multi-neuron correlated activity through the propagation of activity through intermediary neurons. A unique feature of this type of neural circuit is that knowledge of the correlation strengths between adjacent neurons in a mosaic is sufficient for specifying the entire neural circuit and con-

sequently the prevalence of all forms of multi-neuron correlations. In terms of the firing pattern distribution, rather than requiring knowledge of n^2 pairwise interactions, knowledge of n adjacent interactions suffices to predict all activity - a vast simplification in the large neuron regime.

We can explicitly test whether this phenomenological model is consistent with this type of circuit by examining whether *only* correlations between neighboring RGCs are sufficient for predicting multi-neuron firing patterns. Note that we are additionally testing implicitly whether synchrony between non-adjacent neurons is naturally predicted from synchrony between adjacent neurons. Correspondingly, in terms of the Ising model (Equation 3.2), we are setting $J_{ij} = 0$ when neurons i and j are not physically adjacent. This type of Ising model is termed a nearest-neighbor Ising model [126].

In the case of up to 7 neuron firing patterns in primate retina, this pairwise-adjacent maximum entropy (or nearest neighbor Ising model) accounts for 99% of the reproducible correlations in firing patterns of up to 7 neurons[5]. It is indistinguishable statistically from a full pairwise Ising model. In larger populations of up to 118 ON parasol cells this pairwise adjacent structure continues to predict the correct statistics of firing patterns over 99% of the recording time (Figure 3.4). Thus, a reciprocal mechanism is consistent with large-scale firing patterns (Figure 2.2b,c).

3.7 Summary

Until recently, the observation of correlated activity has been largely restricted to the interactions between pairs of neurons. The structure of correlated activity across pairs of neurons has demonstrated how circuitry is specific to each cell type and dictated by the mosaic layout of

[5]Unfortunately, higher order correlations can still be quite significant even when large fractions of the correlated activity are accounted for by pairwise interactions [273].

RGCs [184, 77, 273]. With the advent of large scale recording technology [166, 266], several studies began to explore how the correlations expressed by multiple neurons [261, 178] are qualitatively distinct from correlations observed in pairs of neurons. Fundamental insights into the structure of correlations [8, 258] have created new models for determining whether multi-neuron correlations can be explained in a parsimonious manner [259, 273], although ignoring temporal dynamics and the role of the stimulus (see Section 4.3.2). In particular, these new models have created bridges with otherwise distinct fields of research [126, 123, 121], highlighted how neural circuits exhibit distinct behavior at large scales [296] and provided strong inferences about the underlying neural circuit [273].

This chapter is taken from J Shlens and EJ Chichilnisky, (2007) *Synchrony and concerted activity in the neural code of the retina.* In RR Hoy, GM Shepherd, AI Basbaum, A Kaneko and G Westheimer (ed). **The Senses: A Comprehensive Foundation**, Elsevier Press.

Chapter 4

Neural coding of visual information

Assessing the role of correlations in transmitting visual information from the eye to the brain requires dissecting out the specific contributions correlations between neurons provide about the visual world - a subject of intense interest [104, 191, 257, 206]. A complete understanding of the role of correlations in information transmission in the retina contains broader implications as quantitative insights are applicable across sensory modalities for discerning the role of extrinsic and intrinsic influences on how information is processed. In this section we highlight the numerous questions that arise when examining the role of correlated activity and in subsequent sections we discuss the ensuing quantitative analysis of correlated activity in the retina with a particular emphasis on the resulting biological implications.

The role of correlated activity is a rather broad topic with many perspectives for engaging this issue. If the precise mechanisms underlying this activity were known, then arguably it would be possible to assess the function of correlated activity in the retina (e.g. a signal for spatial contiguity [148]). However, in the absence of such knowledge one must ask more general questions

which attempt to minimize assumptions about how the system works:

- How do correlations alter the receptive fields of RGCs? Do patterns of spiking activity represent specific aspects of the visual scene? (Section 4.1)
- Does the aggregate activity of a population of RGCs provide information about a stimulus that is not available in individual cell activity? (Section 4.2)
- How does the presence of correlated activity effect the ability to decode a visual stimulus? (Section 4.2)
- What types of decoding strategies exploit correlation structure to reconstruct the stimulus (Section 4.3)?

The diversity of questions reflects the intense interest in this field and the multitudes of complimentary tools employed in addressing this broad topic (see [243] for an introduction). Before discussing each specific questions, we must frame these issues quantitatively in the context of several important issues.

Correlations in natural scenes. The statistics of the visual environment contain spatial and temporal correlations over multiple scales [250, 278] and differ substantially from traditional stochastic stimuli [251]. Although a complete characterization of natural scenes is unavailable, the known correlation structure in the visual world can artificially induce correlations in the retina on top of intrinsic correlations. Whether the structure of noise correlations change in the presence of stimulus correlations is an area of active research [4, 129].

Optimal decoding of a neural response. The term *ideal observer* describes the best possible performance any algorithm could achieve at reconstructing a stimulus from a system's

response (for review, see [294]). Unfortunately, this fuzzy notion is ill-defined without explicit reference to a measure of error. Although information theory can place bounds on performance, the optimal estimate of a stimulus under a particular error measure (e.g. maximum a-posteriori) is often difficult to calculate efficiently (but see Section 4.3.2).

While these considerations formalize quantitative issues, at the same time reflect the subtleties that arise when considering these issues. For instance, if the world is swamped with spatial correlations (whose exact distribution is unknown), could the brain use noise correlations as a special channel to extract unique features of the visual world [191, 70]? This question becomes more nuanced if the structure of noise correlations change depending on the stimulus itself due to adaptation in the underlying mechanisms [4, 129]. Thus, simply considering noise correlations as setting the effective prior distribution from which the brain must extract the visual world, while a useful starting point, might over-simplify the complexity of the situation.

How multiple target areas in the brain respond in the presence of correlations can of course be quite distinct from the manner in which the retina encodes visual information. For instance, it is well known that single neurons use a *nonlinear* encoding mechanism (i.e. thresholding), however a majority of information can be extracted using a *linear* decoder [28]. This quantitative discrepancy (i.e. linearity) between the encoding and decoding within a single neuron serves a pedagogical purpose: asking questions about both, while equally important, are entirely distinct mathematically. Thus, as we will see in subsequent sections, the choice of analysis one selects for examining correlated activity ultimately reflects whether one examines how RGCs encode visual information or conversely how the brain decodes the information from the optic nerve.

In the following sections we will approach many of these issues and questions with multi-

tudes of techniques and quantitative tools. We will start from a mechanistic perspective by examining how RGC receptive fields might reflect underlying neurons and conversely, how correlated activity alters the shape of receptive fields. We next move on to discussing how the statistics of correlations have been examined non-parametrically with information theory. We forewarn the reader that this section is the most demanding quantitative section of this chapter, but we do our best to motivate these formulations and discuss the trade-offs for various types of analysis. Finally, we discuss strategies for decoding visual stimuli from retinal spike trains with a focus on understanding the role of these correlations. This discussion will take us away from the retina as modeling and other experimental work influence our perspective about how correlations are exploited by any decoding algorithm, whether biological or artificial.

4.1 Consequences of correlations on neural responses

The receptive field is a fundamental characterization of the stimulus-response properties of a neuron [308], because it characterizes the type of stimulus which causes a neuron to spike. One method to explore the role of correlations in transmitting visual information is to examine how the receptive fields of RGCs are altered by the presence of correlations. This perspective is motivated by a mechanistic view which leverages strong assumptions about the types of interactions to gain some prediction about how response properties of RGCs change due to correlations.

The types of changes one could observed in RGC response properties can range from changes in the timing properties to spatial integration. For instance, one could imagine that a single neuron might fire more reliably just after a nearby (correlated) RGCs fire. Implicit signs of this increment in reliability exist [259, 273] and further analysis has demonstrated that one can predict the spike times of RGCs far better when the spike times of nearby RGCs are taken into

account (J. Pillow, personal communication). Likewise, it is easy to envision that the spatial area of the RF should vary in the presence of correlations. This issue, however, depends on the type of hypothesized mechanism. We discuss each mechanisms, reciprocal and common inputs, in the following sections.

4.1.1 Reciprocal coupling might enlarge receptive field size

A simple hypothesis is that reciprocal coupling increases the size of the integration area of individual RGCs [77, 33] - possibly as a means to boost sensitivity to spatial information at low light levels [65]. A mechanistic interpretation is that a single RGC might fire in response to stimulus-elicited activity in adjacent RGCs, thereby effectively growing its receptive field. Consistent with this hypothesis, amacrine cells in lower vertebrates are electrically coupled and their RFs are far larger than would be expected given their dendritic arborizations [292, 201, 118, 291].

This hypothesis has been explored in rabbit retina [33, 77]. In the rabbit the ON and OFF brisk transient RGCs have comparably sized dendritic trees [222], however OFF brisk transient RGCs exclusively exhibit noise correlations due to reciprocal coupling. If one assumes that both cell types have consistent relationships between dendritic coverage and RF size, one can view the ON brisk transient as a control for examining the effects of reciprocal coupling in OFF brisk transient cells. Indeed, OFF brisk transient cells were systematically better fit by the sum of two Gaussians, where the second Gaussian picked up the skirt of the receptive field. In addition, the receptive field size of OFF brisk transient cells are larger, resulting in a nearly 4-fold increment in RF coverage [78, 77]. A second line of experiments in OFF cells [33] found that the receptive field size more closely matched the spatial extent of the dendritic arbors in α-ganglion cells, even though these cells exhibited tracer dye coupling. Although these results do not measure the spatial

contribution of correlated activity, they do suggest that receptive fields are not grossly extended beyond their dendritic arborizations due to reciprocal coupling.

Preliminary work in primate parasol cells has also examined this question in the context of a new line of statistical models (see Section 4.3.2). Briefly, a class of statistical models (generalized linear models) can be fit efficiently to the stimulus and spike train of a recorded neuron. This statistical model simultaneously fits a linear receptive field, and cross-currents to explain the causal dependencies between neurons and the stimulus [298, 218]. In preliminary work this model has been shown to be an accurate predictor of population activity of RGCs. The benefit of this statistical paradigm is that one can neglect to include cross-currents in the model and measure how the RF size is altered. As predicted, the RF size, in particular the surround, increases roughly two-fold when cross-currents are neglected indicating that cross-currents effectively enlarge the RF size (J. Pillow, personal communication).

4.1.2 Common input might provide fine spatial information

A second hypothesis is that correlated RGC activity reflects the electrical footprint of an underlying interneuron, such as an amacrine cell (see Section 2.2.2). By this hypothesis synchrony between RGCs is a surrogate for the spiking activity (or graded potential) of an underlying common input. An intriguing corollary to this hypothesis is that synchronous activity could reflect a unique channel for visual information that conveys the tuning properties of the underlying common input. This multiplexing hypothesis, sometimes termed *concerted coding*, was first proposed in [191, 189].

One test of this hypothesis is to examine the receptive field of synchronous spikes. If the cells were independent, then the synchronized spike receptive field should approximate the sum

of the individual receptive fields [261]. Surprisingly, in the presence of a minimally correlated checkerboard stimulus, the synchronized spike RF of two reported correlated cell pairs in salamander were smaller than their respective parent cell RF's (see also [70, 300]). This result has been extended to the receptive fields of statistically significant, synchronized firing patterns across multiple neurons identified using a compression algorithm [261]. The receptive field of synchronized firing patterns across 2, 3 or 4 neurons were consistently smaller than the sum of the parent receptive fields. Hence, these results suggest that synchronized activity of multiple RGCs could convey fine spatial information, and are consistent with the hypothesis that an underlying common input provides a multiplexed signal through the correlated activity.

4.2 Information theory and statistics of correlations

One benefit of using a more general statistical theory is that we can minimize the number of assumptions about the effects of correlated firing on conveying visual information. The trade-off is that this comes at the sacrifice of understanding the specifics of the results. Part of the reason for much excitement in recent years is that explorations and debates into correlated activity has led to new understandings of correlations in general and new quantitative tools for disambiguating the consequences of correlated activity [159, 258, 8]. We again remind the reader that this section is quantitatively demanding.

This approach begins by attaching a statistical interpretation to experiments exploring the stimulus-response relationship in the retina. Typically, one thinks of the retina as providing a response r that is some deterministic function of the stimulus s. This response could be from a single neuron or the activity of multiple neurons labeled r_1, r_2, etc. Unfortunately, this perspective avoids a foundational observation of the neural response in all sensory systems: if we present the

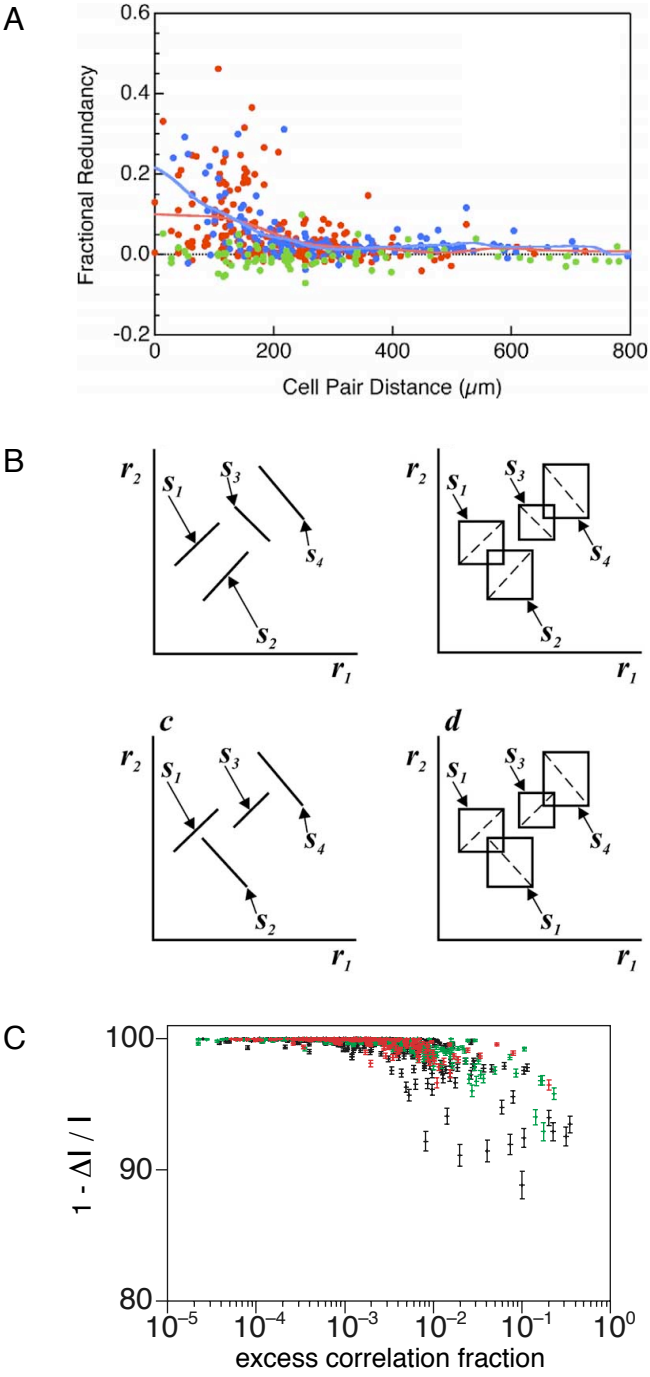

Figure 4.1: Information theoretic analysis of correlated activity. A) Average redundancy (negative of Equation 4.2) expressed as a fraction of the total information conveyed for individual pairs of neurons in the presence of a checkerboard stimulus. Same functional type (blue); ON-OFF cell pairs (green); Other different functional types (red). B) Schematic highlighting how ignoring correlations can have no effect (top row) or a detriment (bottom row) on decoding visual information. Each stimulus is equally likely. Left column shows a correlated distribution. Right column shows distribution where the correlations are ignored. Note that in the bottom right the overlap of the dashed line in within a neighboring box is indicative of lost precision in identifying the stimulus. C) Fraction of information that is retained by decoding while conditionally independent posterior distribution $p_{ind}(s|r)$ is used instead of $p(s|r)$. The x-axis measures the strength of the synchrony. Figures adapted from [159, 206], respectively.

same stimulus multiple times, we often record a range of neural responses. This variability appears non-deterministic (but see [1]) and thus a common strategy is to regard the neural response as random, whose relative frequency and regularity are dictated by a conditional probability distribution $p(r|s)$ [243, 83, 163]. From this perspective, one can view each measurement as a random sample from this distribution. The observation that the neural response is related to the stimulus is reflected in the structure of the conditional distribution, or said more precisely, the differences between $p(r)$ and $p(r|s)$. These changes can be quantified using *mutual information* $I(S;R)$, a non-negative measure of statistical dependence; it is zero if and only if the two variables are statistically independent (see Appendix A.7). An important feature of mutual information is that it bounds the performance of any potential decoding mechanism, whether artificial or biological.[1]

The focus of neural coding is the (nonlinear) correlation between the stimulus s and the neural response r, however the focus of our interest is the correlation between individual neural responses r_1 and r_2. Of course, we must be mindful of the fact that the stimulus drives these neural responses. For instance, the observation of statistical dependence $p(r_1, r_2) \neq p(r_1)p(r_2)$ between a pair of neurons (or $I(R_1;R_2) > 0$) does not necessarily reflect intrinsic mechanisms in the retina because a stimulus might induce such correlations. Intrinsic correlations (i.e. noise correlations) instead reflect the failure of independence when the stimulus is held fixed

$$p(r|s) \neq \prod_i p(r_i|s).$$

The failure of *conditional independence* is the statistical interpretation of noise correlations.[2] We

[1] For instance, one might employ an algorithm to estimate the motion in the visual scene s_{est} from a neural response r. This algorithm could be a model for visual processing in MT cortex [100] or be a read-out method for a neural prosthetic device [264]. Regardless, the fundamental property of mutual information guarantees that $I(S;R) \geq I(S;S_{est})$ meaning that $I(S;R)$ is an upper bound on the amount of information available to the decoding algorithm.

[2] We emphasize that, while useful for dissecting out the contributions of the circuit, the statistical distinction of noise correlations is completely artificial from the perspective of a decoding algorithm in the brain. The brain can not

can label the right hand side of the equation $p_{ind}(r|s) \equiv \prod_i p(r_i|s)$. The quantity $p_{ind}(r|s)$ is an artificial construct that is quite useful for understanding the role of correlated activity, because it provides a statistical model for what the neural response would be if the neural response were conditionally independent (or as if noise correlations do not exist.). By the same token, if the neural responses were conditionally independent, then the conditional mutual information would be zero $I(R_1;R_2 \mid s) = 0$. Often, though, we are interested in the average conditional dependence over a distribution of stimuli

$$I(R_1;R_1|S) = \sum_s P(s) I(R_1;R_2|s). \tag{4.1}$$

We will revisit this quantity multiple times in the following section as in effect, $I(R_1;R_1|S)$ acts as the information theoretic analog of the cross-correlation function, measuring the average strength of noise correlations [257].

Before proceeding further, we must discuss a large caveat to applying these and subsequent ideas to real data. Ultimately, our goal is to examine the structure of $p(r|s)$ from a finite set of measurements. A large base of literature has recognized that information theoretic quantities derived from finite measurements of $p(r|s)$ can be systematically biased [193, 297, 214]. Although many novel estimation techniques have been developed recently (reviewed in [304]), one must take caution and additionally evaluate any experimental conclusions based on whether information theoretic quantities are estimated well [213].

In the following sections we discuss two complimentary approaches in the literature for quantifying the effects of correlations using information theory. For each topic we discuss what

distinguish whether correlations are driven by a stimulus or the retinal circuit. Hence, it is highly suspect to believe that the brain can recognize whether RGCs are conditionally independent [257].

conclusions one can draw about the retina. Finally, because consensus has not yet emerged in this field, we discuss limitations for applying any information theoretic analysis to decipher the role of correlations.

4.2.1 Measuring additional information in correlated neural responses

One method for assessing the significance of correlations is to ask whether correlations enhance or degrade information about the stimulus. Consider the total information the correlated response of two neurons provides about the stimulus $I(S;R_1,R_2)$. If more information is available about the stimulus by observing the simultaneous neural response, then in principle one could build a better decoder of visual information using the joint statistics. On one extreme two neurons could provide distinct information about the stimulus (e.g. two RGCs on opposite ends of the retina), thus the total information these two neurons provide is the sum of the individual informations $I(S;R_1,R_2) = I(S;R_1) + I(S;R_2)$. However, a natural extension is to ask whether additional information about the stimulus is provided by observing the simultaneous (joint) responses. This difference has been defined as the synergy

$$Syn(R_1,R_2) \equiv I(S;R_1,R_2) - [I(S;R_1) + I(S;R_2)]\,. \tag{4.2}$$

The synergy measures how much additional information is encoded in the joint response rather than the sum of the individual neural responses [104, 103, 170, 39, 257]. This quantity is intuitively appealing and also follows from natural generalizations of mutual information [258] (see also [187, 318]). The role of noise correlations becomes evident by rewriting the above equation as

$$Syn(R_1,R_2) = I(R_1;R_2|S) - I(R_1;R_2). \tag{4.3}$$

Because mutual information is a non-negative quantity, the synergy must be bounded from above by the average strength of the noise correlations (Equation 4.1) and from below by the average strength of the overall correlations between the neural responses [257]. If the synergy is positive, then pairs of neurons provide more information about the stimulus than the sum of its parts [39, 104, 170, 103].

If Equation 4.2 is negative, then the information neuron 1 provides about a stimulus duplicates information that neuron 2 provides about the stimulus. Negative synergy has been termed *redundancy* in the neural coding literature [257, 104, 240] and measures how much information about the stimulus is duplicated between neural response.[3] Redundancy has been systematically examined in the salamander retina [239] (but for similar analysis see [200, 170, 103, 104]), a species which exhibits little mosaic structure in RGCs [267]. In multi-electrode recordings of salamander retina, 479 pairs of RGCs were presented various natural movies as well as white noise checkerboard stimuli. In the presence of all stimuli, pairs of neurons exhibited substantial spatially localized redundancy that tapered off with distance [239], roughly corresponding with the spatial scale of correlations [191] (Figure 4.1a). Very few of the cell pairs exhibited synergy not explained by sampling errors, thus by extrapolating to large populations of cells, one can surmise that each bit of visual information is replicated 10-fold across the RGC population in salamander.

4.2.2 Are correlations necessary to identify the stimulus?

Examining differences in information highlights how much information is available about the stimulus but it does not specify whether correlated activity is *necessary* to reconstruct the

[3] Redundancy used in this context is quite distinct from redundancy often used in information theory literature [271, 60]. In the information theory literature, redundancy is the failure to maximize the total amount of information which could be transmitted down a noisy communications channel [159, 17, 21].

stimulus. A second perspective is to examine the consequences of noise correlations on the ability of the brain (or any system) to reconstruct the stimulus. Why this question is distinct can be observed in the schematic in Figure 4.1b. In these two toy examples, the two neural responses are correlated, however in the top row the correlations are necessary for decoding the identity of the stimulus, while in the bottom row the correlations are not necessary. The subtle point to glean from this example is that although noise correlations might increase our knowledge about the stimulus, noise correlations might be unnecessary for identifying a stimulus [206].

This slight change in emphasis has important consequences on the ensuing analysis as the focus now shifts to our uncertainty about the stimulus having observed a neural response. We can make this notion precise by applying Bayes rule [83] to calculate the posterior distribution of stimuli $p(s|r) = \frac{p(r|s)p(s)}{p(r)}$ consistent with an observed neural response.[4] To ask how noise correlations affect the posterior distribution of stimuli, we can create an artificial posterior distribution $p_{ind}(s|r)$ derived from the conditionally independent distribution $p_{ind}(r|s)$ using Bayes rule $p_{ind}(s|r) = \frac{p_{ind}(r|s)p(s)}{p_{ind}(r)}$ where $p_{ind}(r) = \sum_s p_{ind}(r|s)p(s)$. If $p_{ind}(s|r) = p(s|r)$, then noise correlations do not effect the posterior distribution and are unnecessary to identify the stimulus. We can use the Kullback-Leibler divergence (see Appendix A.7) to assess how poorly one fares with an approximate distribution $p_{ind}(s|r)$ in lieu of the actual distribution $p(s|r)$,

$$\Delta I(R_1, R_2) \equiv \sum_r p(r)\, D_{\mathrm{KL}}\left[p(s|r) \;||\; p_{ind}(s|r)\right] \tag{4.4}$$

averaged over all neural responses. $\Delta I(R_1, R_2)$ was proposed by [206] (see also [219, 235, 205])

[4] We note for completeness that a particular distribution by itself does not specify a decoded stimulus. Commonly, when dealing with a posterior distribution, one selects the maximum a-posteriori (MAP) or MMSE estimate of the stimulus. The choice of the decoding estimator reflects an underlying choice of error function. More will be discussed about this in Sections 4.2.3, 4.3.

as an upper bound on how much information is lost about the identity of the stimulus by selecting the conditionally independent posterior distribution over the correct posterior distribution (see also [325]). If $\Delta I(R_1,R_2) = 0$, then the posterior distribution of the stimulus is invariant to the presence of noise correlations. However, as $\Delta I(R_1,R_2)$ increases, there is a greater potential cost in bits of assuming conditional independence for reconstructing the posterior distribution. To highlight the role of noise correlations (Equation 4.1), we rewrite this quantity as

$$\Delta I(R_1,R_2) = I(R_1;R_2|S) - D_{\mathrm{KL}}\left[p(r) \,||\, p_{ind}(r)\right]. \tag{4.5}$$

Note the parallel with Equation 4.3 (see [9] for discussion). In particular, $\Delta I(R_1,R_2)$ is bounded from above by the average strength of the noise correlations so long as all observed responses $p(r)$ occur in the marginal distribution derived from conditional independence $p_{ind}(r)$ [257, 9].

Across about 1000 pairs of RGCs in mouse stimulated with a natural movie, the amount of information lost about the posterior stimulus distribution was small compared to the total amount of stimulus information in the pair of neurons [206] (see also [229, 230, 220, 211, 109, 16]). Nearly all pairs exhibited less than a 10% loss in information about the stimulus with the vast majority of pairs less than 5% (Figure 4.1c). Hence, when examining pairs of neurons one can determine the posterior distribution with minimal cost if one assumes conditional independence between pairs of neurons. It remains to be seen whether this result holds in larger groups of neurons [159].

4.2.3 Limitations of information theory

A profound limitation of information theory is that this class of measures do not inform us *how* these neural responses are related, nor which features of the correlation are important to the organism (but see [295, 81]). In particular, one limitation with any approach based on information theory is that because derived quantities are in bits, it is difficult to interpret what the function of these bits are. For instance, what if $\Delta I(R_1, R_2) = 1$ bit, how does an incorrect posterior distribution effect a stimulus estimate? This single bit could have a profound or negligible influence on $p_{ind}(s|r)$ and concomitantly on any estimate of a stimulus s_{est}. Ultimately, when one begins to think about creating an estimate of the stimulus s_{est}, information theory is insufficient for judging the quality of decoding - a measure of absolute error must be considered. Given a particular error measure (e.g. mean squared error), one could ask whether measured bits bound the magnitude of error (for review, see [294]). Unfortunately, in the case of $\Delta I(R_1, R_2)$, only weak bounds have been identified for limited cases (P. Latham, personal communication). In general, no bounds have been identified, meaning that one bit could translate into potentially large deviations.

A second limitation with information theory is that it averages across an entire distribution of neural responses. Although averaging over an entire distribution provides a measure that obeys several central requirements in information theory [60], this average can obscure the contribution of individual symbols within a neural code [80]. New methods have been developed for peering inside this expectation [80, 39, 274] and preliminary results have demonstrated that individual correlated neural responses in the retina provide surprising contributions to resolving the identity of a stimulus [260]. These and future results must be weighed against the fact that the principal theorems of information theory are solely derived from expectations across distributions [60], and

peering inside the expectation can be fraught with complications [80, 46, 47, 27]. Thus resolving the contributions of individual neural responses might ultimately require examining one's ability to reconstruct the stimulus.

4.3 Reconstructing the stimulus

For all of the limitations of information theory, one benefit of a non-parametric approach is that it avoids making assumptions about what features and errors are important to a biological system. In the context of an organism under evolutionary pressures, it is unclear if any single measure of error is appropriate given multiple competing factors and the complex environment in which the nervous system operates. That said, given the clear function of early sensory systems such as the retina, reasonable criterion can be proposed to test whether neural systems are optimized to their environment [242, 161].

Selecting a measure of error to judge the quality of an estimate of a stimulus is an archetypical example of parameter estimation, a field with a long history in statistics [163] and engineering [143, 199]. Not surprisingly, there exist an infinite number of error measures, however, it is well established that for certain error measures and classes of estimators, one can derive the optimal estimator, i.e. perform optimal decoding. For example, the Bayesian MMSE estimator is optimal under a mean squared error loss function, while a maximum a-posteriori estimator is optimal under more restrictive regimes or a zero-one loss function [143, 199].

The optimal decoder, even under a mean squared error, is often difficult in practice to calculate, even for the relatively simple case of a single neurons (but see [237, 218]). Thus, one strategy is to resort to regression techniques focused on functional approximations of the decoder under a

particular error measure. In recent years, new statistical techniques have permitted the calculation of optimal Bayesian decoders, however, these results must be qualified by several technical limitations. Furthermore, in many cases novel statistical techniques have been pioneered in improving the decoding ability for single neurons. Thus, historically a large literature base exists in single neuron decoding (reviewed in [277]); only in the last few years have attempts to extend these ideas to multi-neuron activity yielded insights into how correlations have contributed to coding of visual information. We discuss both regression and Bayesian techniques (following [231]), highlighting recent applications of decoding techniques to multi-neuron activity and showcasing novel methods as yet solely applied to single neurons.

4.3.1 Regresssion

Regression refers to estimation techniques that attempt to minimize a loss function (typically, mean squared error) by exploiting functional approximations without any explicit calculation of the posterior distribution [143]. The seminal work of Bialek and colleagues [29] (see also [72, 28]) demonstrated that a linear decoder that minimizes the mean squared error can perform quite well at reading a neural code approaching the theoretical maximum dictated by biophysical constraints. Linear decoding has since been applied in many neural coding contexts outside of the retina because an analytical solution is tractable and easily calculated using standard signal processing techniques (e.g. [127, 36, 113, 268, 49, 263]).

In the context of correlated activity, linear decoding techniques have been extended to decode the simultaneous activity of multiple neurons [309, 70]. In the presence of spatially uniform, photopic stimulation, multiple RGCs in salamander of the same functional type provide duplicate information about the stimulus but RGCs of distinct functional types provide independent infor-

mation about the stimulus [309]. Conversely, authors in a separate study used a variant of linear decoding to study the correlated activity of target neurons to RGCs in cat and found that such a decoder could extract 20% more information about the stimulus when synchronous activity is considered. Linear decoding permits such analysis because of its analytical simplicity but is limited by the fact that the optimal decoder need not be (nor probably is) linear.

Differences between the information extracted by linear decoders and non-parametric measures of information suggest that more sophisticated types of decoding strategies could extract more information about the stimulus [7, 277] . Extensions have explored how higher-order terms [243, 89], artificial neural networks [309], kernel regression [276, 86] and curved manifolds [7] improve the reconstruction of the stimulus. In addition, other lines of work have examined how optimizing information theoretic error measures improve estimates of the stimulus [272, 213, 232]; one benefit of the latter approach is that such techniques work well under non-Gaussian stimuli, a traditional limitation of decoding techniques [272, 277]. Such techniques have been successful in studying single neuron responses and applying them to examine multiple neuron responses might require simplifying assumptions to minimize data requirements and make the solution computationally tractable [232].

4.3.2 Bayesian methods

The diversity of regression techniques for neural decoding leverage off a a wealth of methods available for functional approximation and error minimization [238], but suffer from the fact that they require the decoder to be a particular functional form. For instance, if the optimal decoder is not a polynomial, approximating the decoder with successively higher-order polynomial terms would be inefficient if not prohibitive [243, 213]. The optimal decoder can be calculated though

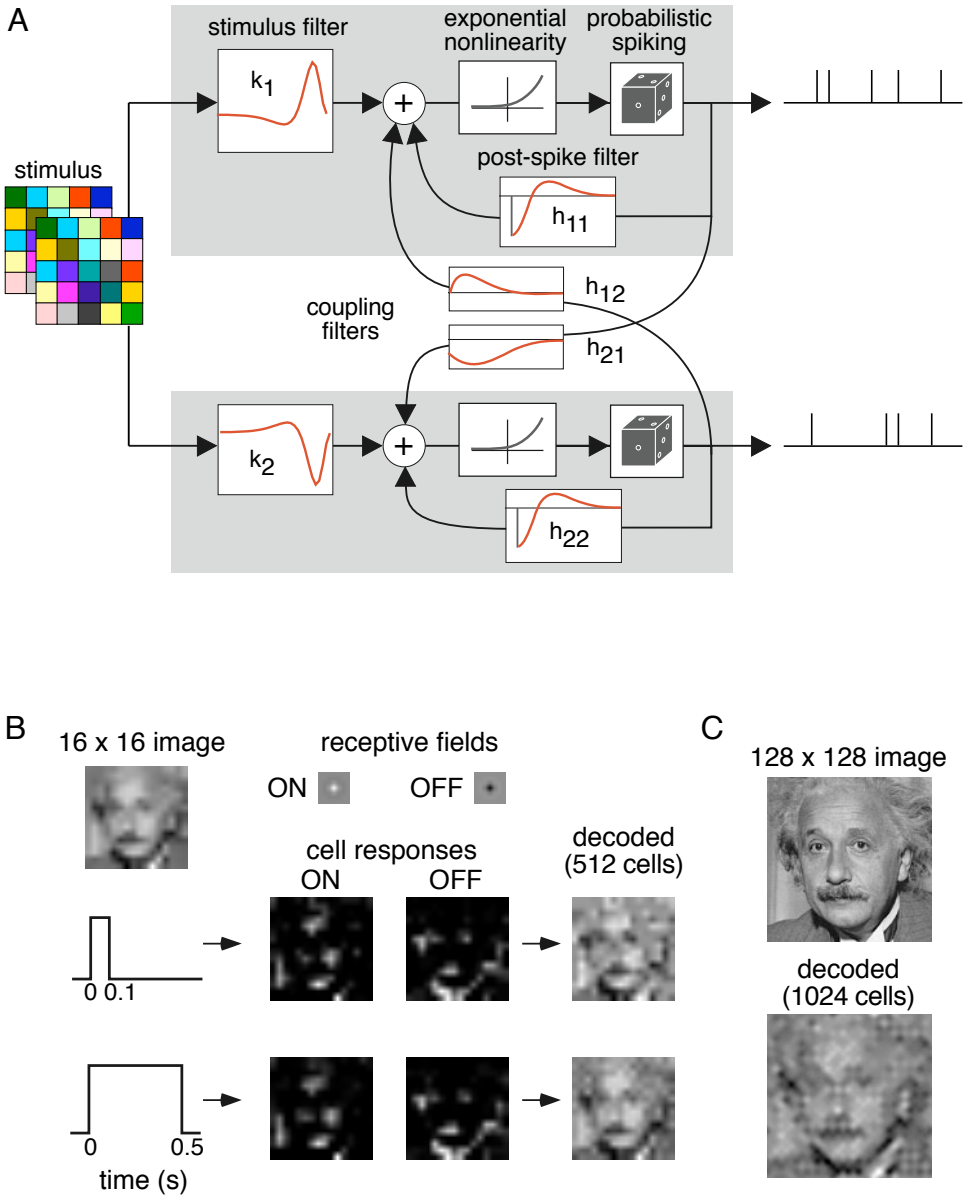

Figure 4.2: Illustration of Bayesian decoding in populations of neurons. A) Schematic of point process encoding model (generalized linear model). Each shaded region corresponds to the summed and exponentiated response of a single neuron. Model parameters, the linear stimulus filter $\{k_i\}$ and post-spike currents $\{h_{ij}\}$, are estimated using maximum likelihood from neural data. B) Steps in Bayesian MAP decoding of small image patch using responses of 512 simulated RGCs. Image presented briefly to simulated RGCs (0.1, 0.5 sec, respectively) and spike trains from cells summarized as spike rates in middle panels and Bayesian MAP estimate of stimulus computed from spike trains from brief duration presentation (right panel). (c) Bayesian MAP decoding on larger image which necessitates searching through larger 16,384 dimensional stimulus space.

through the application of Bayes rule to determine the posterior distribution of stimuli $p(s|r)$ for a given neural response r. An optimal estimator of the stimulus can subsequently be calculated from the posterior distribution $p(s|r)$; for particular error measures, such as mean squared error (or zero-one loss), the optimal estimator is well known and computationally tractable using new Monte Carlo techniques [102]. Furthermore, Bayesian estimates of the stimulus provide a natural error bar based on the the width of the posterior distribution.

The limitation of a Bayesian estimate of the stimulus is that they require that the prior distribution of stimuli $p(s)$ and crucially the generative model $p(r|s)$ be properly specified. Specifying the correct generative model $p(r|s)$ must however be weighed against the difficulty in estimating parameters specifying the model. For instance, parameters of some neural models are intractable [144], where as the parameters of other models are inefficient [117] of computationally intensive [217] to estimate. Further complications arise when generating Bayesian estimates of the stimulus because they involve high-dimensional integrals over stimulus space [83]. In spite of these hurdles, progress has been made by using low dimensional stimuli [185, 142, 2] and exploiting recursive techniques [333, 44, 19, 326, 42, 145, 275] to compute a Bayesian estimate of the stimulus.

A new class of statistical models, termed *generalized linear models* (GLM's) [186, 215], has offered several promising new avenues, providing the necessary richness to reproduce the dynamics and nonlinearities of single neurons [105, 136] and network correlations [217, 298], yet the parameters of these models can be estimated efficiently using maximum likelihood [215, 298, 19]. For example, one proposed class of GLMs model populations of coupled neurons as a point

process [69] with an instantaneous firing rate (or conditional intensity function),

$$\lambda_i(t) = \exp\left(k_i \cdot x(t) + \sum_{j,s} h_{ij}\,\delta(t - t_{js})\right) \tag{4.6}$$

where i indexes the firing rate of each neuron over time t; s indexes all observed spike times up to time t; k_i is each neuron's linear stimulus filter and h_{ij} is the post-spike effect from the j'th (to the i'th) observed neuron. In particular, the parameter h_{ii} captures each neuron's refractory effect following a spike while h_{ij} (for $i \neq j$) captures the effective pairwise coupling (or correlation) between neurons. A diagram of this model is in Figure 4.2a. The set of parameters $\{h_{ij}, k_i\}$ does reflect some (unobserved) biophysical process, but because this is a phenomenological model, biophysical conclusions derived from estimated parameters must be interpreted with care.

In addition to efficiently estimated parameters, GLMs offer the added benefit that the log-likelihood function is concave in stimulus space (as well as parameter space) making it possible to perform Bayesian decoding. Leveraging Monte Carlo techniques permits estimation of Bayesian MMSE estimator and information theoretic quantities for populations of neurons, tasks otherwise impossible using non-parametric techniques [231]. An example of the power of these decoding techniques is demonstrated in simulation in Figure 4.2b in which the optimal stimulus was estimated for 1024 simulated RGCs across 16,384 stimulus dimensions. The power of the GLM framework is that the Bayesian (or optimal) decoder can be computed for populations of neurons but this must be weighed against several technical limitations. The first issue is that the prior stimulus distribution must be well specified and log-concave [216] – both of these restrictions prevent the presentation and analysis of natural scenes [278] and restrict attention to exponential distributions. The final issue of course is that the encoding model could be wrong. For instance, if a

neuron responded linearly to a stimulus (but see, e.g. [54]) and pairwise correlations were entirely reciprocal (but see Section 2.2), this might be the appropriate model class. However, in spike of these shortcomings, GLM's can still provide a good approximation of RGC population activity (J. Pillow, personal communication). These shortcomings, however, could be remedied with new extensions incorporating latent common input [158] and other extrinsic factors [298].

4.4 Summary

The field of neural coding has grown tremendously in the last few decades (for early review, see [226]) with the development of many new quantitative tools for the analysis of neural data [243, 304]. In particular, much focus has shifted from understanding the information content of a single neuron towards understanding the activity of populations of neurons, termed *population coding*, and this change in emphasis has had a large impact on retinal physiology [190, 96]. In particular, new results have suggested that correlated activity in the retina could reflect special channels for communicating visual information [191] or provide redundancy to safeguard against errors in transmitting visual information [239]. While debate and discussion still resides in how to properly analyze this activity [257, 159], the tantalizing possibility exists that observations of weakly correlated activity in small scale systems could translate into dominant strategies used by the early sensory systems to transmit visual information [17, 259, 273].

This chapter is taken from J Shlens and EJ Chichilnisky, (2007) *Synchrony and concerted activity in the neural code of the retina.* In RR Hoy, GM Shepherd, AI Basbaum, A Kaneko and G Westheimer (ed). **The Senses: A Comprehensive Foundation**, Elsevier Press.

Chapter 5

Structure of Multi-Neuron Firing Patterns in the Primate Retina

5.1 Introduction

A central challenge in neuroscience is to understand how large circuits of neurons represent and process information. For decades, studies of neural function were restricted to recordings from single neurons, with the tacit assumption that the function of complex circuits could be deciphered with such measurements (see [308]). However, multi-neuron recordings have revealed substantial interactions that cannot be observed with single-neuron recording. For example, retinal ganglion cells (RGCs) exhibit strong stimulus-independent correlated activity; the circuits mediating such correlations and the consequences for visual processing are not fully understood [12, 135, 183, 191, 77, 261, 206, 257]. Such findings suggest interesting possibilities for circuit function, but at the same time raise a major concern: will it be necessary to record from all the cells in a neural circuit, and analyze all possible interactions, to determine how the circuit works? If so, a deep

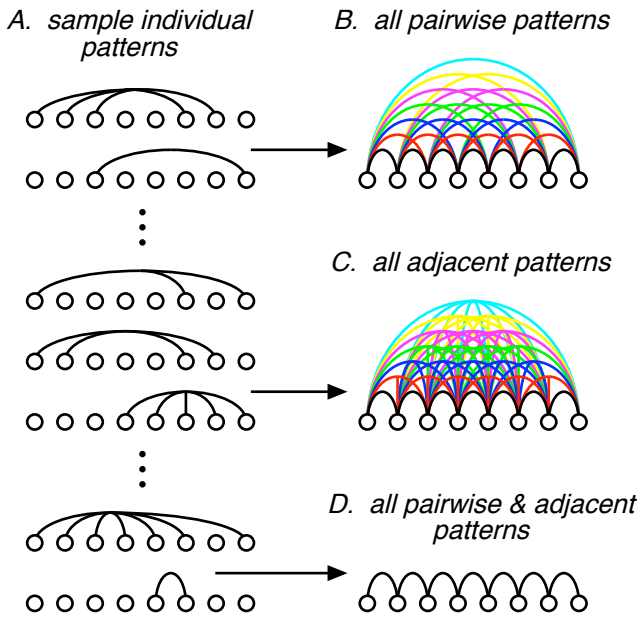

Figure 5.1: Patterns of connectivity. (a) A small random sample of the possible input patterns to a collection of $n = 8$ cells. From top to bottom, 7 different hypothetical input patterns are shown, each terminating on a different collection of target cells (circles). In general, the total number of distinct patterns is on the order of 2^n. (b) All distinct pairwise patterns, superimposed. Each color shows, superimposed, all pairwise patterns across cells separated by a particular distance. An example of a single pairwise pattern from (a) is indicated with an arrow. In general the number of distinct pairwise patterns is on the order of n^2. In this simplified diagram, the 28 patterns shown exclude wraparound and symmetric patterns. (c) All distinct adjacent patterns, superimposed. Each color shows, superimposed, all adjacent patterns consisting of a particular number of cells. An example of one adjacent pattern from (a) is indicated with an arrow. Again, 28 distinct patterns are shown, in general the number of distinct patterns is on the order of n^2. (d) All possible patterns that are both pairwise and adjacent, superimposed. 7 patterns are shown, a single example is indicated with an arrow. In general, the number of possible patterns is on the order of n.

understanding of many neural systems may be out of reach for a long time.

In this context, any simplifying principles that can make the problem more tractable are of great value. To illustrate this, consider the number of possible circuits terminating on a collection of n neurons. The number of distinct circuits is determined by the number of distinct input patterns that contribute to the circuit. Examples of distinct input patterns are illustrated schematically for $n = 8$ cells in Figure 5.1a. Even with this small value of n, the entire collection of distinct patterns is too large to depict easily; thus only selected examples are shown. In general, the number of possible input patterns is ˜2^n, a prohibitive complexity: for the collection of several hundred RGCs

depicted in Figure 5.2a, 2^n exceeds the number of stars in the known universe [165]. However, two simple constraints on connectivity can dramatically simplify the problem. The first is *pairwise* connectivity, in which each input pattern contacts only two cells. All pairwise patterns may be depicted together in a single diagram (Figure 5.1b). The second is *adjacent* connectivity, in which each pattern contacts all cells within its extent. This constraint also restricts the possibilities to a set which can be depicted easily (Figure 5.1c). The pairwise and adjacent constraints each reduce the number of possible patterns to $\sim n^2$, a huge simplification. With both constraints, the number of possible patterns is reduced to $\sim n$ (Figure 5.1d). The practical consequences of this simplifcation are profound: in principle, one can understand the function of the entire circuit simply by recording from individual cells and pairs of neighboring cells.

The importance of these simplifying principles is illustrated in the retina. Recent work suggests that synchronized firing among RGCs could originate in common input to multiple RGCs, forming a multiplexed neural code in which the large and distinctive electrical "footprint" of a presynaptic cell conveys a specific visual message to the brain [191, 261]. Other studies have also suggested interactions in RGC light responses over large spatial scales [188, 210]. From such observations, a picture of retinal connectivity emerges in which all possible interactions between large numbers of cells must be probed before the function of the circuit can be understood (Figure 5.1a). On the other hand, several lines of evidence indicate that synchronized firing can originate from pairwise, adjacent interactions: gap junction coupling between adjacent RGCs, electrical coupling of neighboring RGCs via an intermediate amacrine cell, or common synaptic inputs from bipolar or amacrine cells to neighboring RGCs [183, 41, 125, 119, 262, 65, 130, 306]. Thus, interactions among multiple RGCs over large spatial scales may simply reflect the combined effect of pairwise, adjacent interactions (Figure 5.1d), which can be characterized using readily

available experimental methods.

In this paper we test whether multi-neuron firing patterns are consistent with purely pairwise adjacent connectivity, or instead imply more complex circuitry. Until recently, two major challenges have precluded such an investigation. First, one must be able to record simultaneously from all cells in a circuit over a substantial area [100, 266]. Second, one must have a framework within which to assess the significance of higher order interactions among the neurons in a circuit [8, 258, 259]. We approach these issues with a combination of novel techniques. We apply new 512-electrode electrophysiological recording [100, 166] to the primate retina, which contains 1-2 dozen distinct RGC types that convey complete, parallel images of the visual scene to distinct targets in the brain, and which closely resembles the human retina [245]. In these recordings, distinct cell types such as the ON and OFF parasol cells are easily identified (Figure 5.2a) [316, 236]. The regular mosaic arrangement of these cells in the retina [221, 314, 78], combined with recordings that sample almost all the cells of each type, make possible a direct test of pairwise and adjacent connectivity. We perform this test by examining the spatial patterns of electrical activity in different cells using the maximum entropy framework borrowed from statistical mechanics [132, 133], as described in [8, 178, 258, 259]. The results indicate that patterns of electrical activity in groups of parasol cells may be understood almost entirely based on pairwise interactions, restricted to adjacent cells in the mosaic. This finding substantially simplifies our understanding of the retinal circuit.

5.2 Methods

Action potentials were recorded from RGCs in isolated macaque monkey retina perfused with physiological saline solution, using an array of 512 electrodes [166, 100]. The receptive

field of each RGC was identified using reverse correlation with a white noise stimulus. Cells were segregated into distinct classes according to their receptive field characteristics; ON and OFF parasol cells were identified by their size and response kinetics [54]. The receptive fields of all ON and OFF parasol cells in one recording are shown in Figure 5.2a. These form an orderly mosaic that tiles visual space with minimal overlap, as expected from previous work in primates and other species [314, 78, 64]. The completeness of the mosaics indicates that the recordings sampled most of the parasol cells in the 4×8 degree region of retina. For details of methods, see Appendix A.

5.3 Responses of nearby RGCs are not statistically independent

To quantify functional connectivity in the retinal circuit, spontaneous activity of ON and OFF parasol cells was recorded in the presence of steady, spatially uniform, photopic illumination. Interactions between pairs of cells were probed by examining the cross-correlation in spiking activity, that is, the probability that one cell fired as a function of time relative to the time of a spike in the second cell. If the two cells fired independently, the cross-correlation would be flat. Instead, nearby cells of the same type (ON or OFF) exhibited a strong tendency to fire nearly synchronously, as shown by the pronounced peak at the origin with a width of about 10 ms (Figure 5.2B) . This *synchronized firing* in the absence of time-varying stimulation (also known as *noise correlations*) resembles observations in other species, and indicates functional connectivity due to common inputs and/or reciprocal connections in the retina [12, 135, 183, 191, 78, 119, 41]. Anti-correlation between ON and OFF parasol cells was also observed (data not shown; [181]), however, subsequent analysis will be restricted to cells of the same type.

Pairwise synchrony was restricted to nearby cells. To quantify this tendency, spike trains

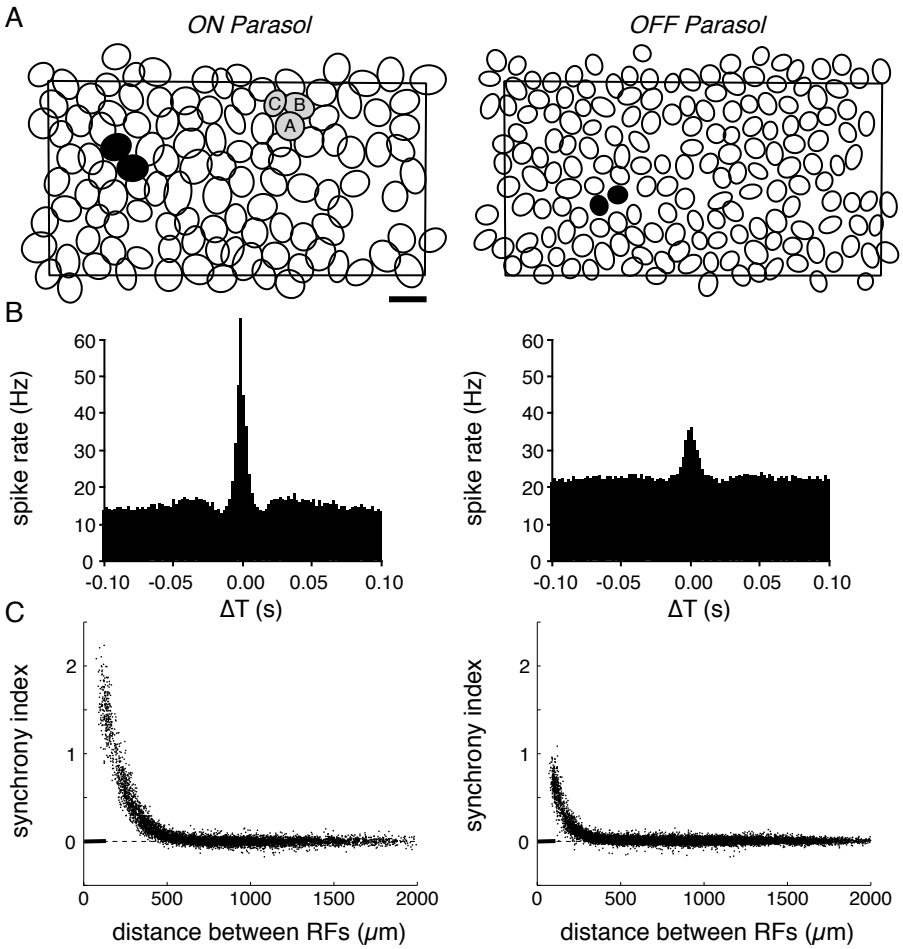

Figure 5.2: Pairwise synchrony. (a) receptive fields of 118 ON and 175 OFF parasol RGCs simultaneously recorded in one retina. Ellipses represent 1 SD of the Gaussian fit to the spatial profile of the receptive field. Rectangles represent outline of electrode array. Scale bar: 200 micrometers. (b) Sample cross-correlation functions for pairs of ON and OFF parasol cells shown shaded in black in (a). The firing rate of one cell is shown as a function of time relative to the time of a spike in the second cell. The synchrony index for these pairs is $S = 1.57, 0.59$, respectively. (c) Synchrony index S as a function of distance between receptive fields of ON and OFF parasol cells. For comparison, the black bar near the origin represents the modal separation between cells in the mosaic (see Methods).

from pairs of cells were binned at a resolution of 10 ms, yielding binary spike counts A and B as a function of time. The probability of synchronous firing, $P(A = 1, B = 1)$, was measured, where 1 denotes the occurrence of a spike. This probability was expressed relative to the probability expected from statistically independent firing using a *synchrony index*:

$$S = \log_2 \frac{P(A = 1, B = 1)}{P(A = 1)(B = 1)} \tag{5.1}$$

The index is shown as a function of separation between pairs of cells in Figure 5.2c. Cells separated by less than several hundred μm, corresponding to about 3 times the average cell-cell separation in the mosaic, fired synchronously at rates well above chance (S=0). Cells that were more widely separated did not. In summary, pairs of parasol RGCs in primate retina are functionally connected, and this connectivity is universal among cells of like type and spatially localized [183].

The above observations provide significant constraints on functional connectivity between RGCs. However, the connectivity of the circuit cannot be understood with these measurements alone. First, the fact that pairwise synchrony extends over a distance of several cells in the mosaic (Figure 5.2c) does not require that direct connections reach this far. Instead, synchrony might be mediated by pairwise interactions, for example, gap junction electrical coupling, propagated through several intermediate cells [125, 119, 262, 65, 130, 306]. Second, the observed pairwise synchrony provides no information about higher-order interactions. To illustrate the distinction between pairwise and higher-order synchrony, consider two hypothetical mechanisms: (a) common input from a spiking amacrine cell to more than two RGCs [191, 261], (b) direct gap junction electrical coupling between pairs of RGCs (note that these candidate mechanisms are not exhaustive,

but merely serve as examples). These mechanisms can produce very similar cross correlations in pairs of cells, but very different concerted firing patterns in multiple cells. Specifically, in case (a), a single spike in an amacrine cell could induce a spike in most or all of its RGC targets simultaneously. However, in case (b), the probability of the entire collection of RGCs firing synchronously is relatively low. The distinction is fundamental: the mechanism of case (a) has been suggested as a way to convey distinctive, multiplexed visual messages to the brain [191, 261]. This simple example illustrates that pairwise synchrony provides only a limited picture of circuit connectivity. Thus, probing the full extent of neural interactions requires measuring patterns of firing in many cells simultaneously.

5.4 Triplet synchrony is explained by pairwise interactions

Consider three adjacent ON parasol cells labeled A, B, and C in Figure 5.2a. Each cell pair exhibits strong synchronized firing (Figure 5.3a). To characterize the joint activity of the three cells requires extending the notion of cross-correlation to three dimensions. The left plot in Figure 5.3b shows the probability of spikes in all three cells as a function of time shifts ΔT between cells A and B, and A and C. The three extended ridges represent the preponderance of synchronous firing in each of the cell pairs, regardless of the activity of the third cell, similar to Figure 5.3a (for an alternative representation, see [228]). However, the prominent peak at the origin, with a width of about 10 ms, indicates that all three cells often fired synchronously. The key question is whether this multi-cell firing occurs at the rate expected from the known pairwise correlation (e.g. mechanistic hypothesis (b) above), or alternatively, whether more complex patterns of interaction are required to explain triplet firing (e.g. mechanistic hypothesis (a) above).

To distinguish these possibilities requires a null hypothesis: the probability of all three cells

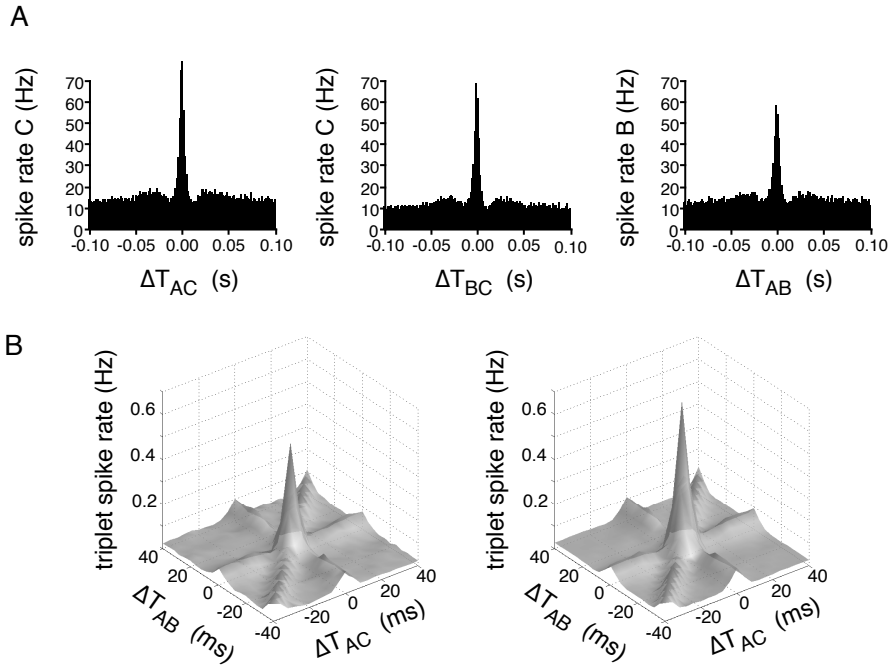

Figure 5.3: Triplet synchrony. (a) Cross-correlation functions for each pair from a group of three adjacent ON parasol cells (labeled A,B,C in Figure 5.2a). Each cell pair exhibits strong synchrony ($S = 1.90, 2.05, 1.64$ from left to right). (b) Three dimensional cross-correlation for triplet synchrony (left), and maximum entropy pairwise prediction (right). Note that maximum entropy predictions computed for different time offsets are not statistically independent.

firing in the same time bin (Δt = 10 ms), given only the pairwise interactions. This is analogous to the two-cell case, in which the null hypothesis was statistical independence and a synchrony index much greater than zero revealed a departure from the null hypothesis. However, in the case of three or more cells, the null hypothesis is not as simple, because the statistical independence hypothesis,

$$P_{ind}(A,B,C) = P(A)P(B)P(C) \tag{5.2}$$

does not account for known pairwise correlations. Ideally, one would compare the observed data to a null hypothesis which assumes nothing beyond pairwise correlations.

An approach borrowed from statistical mechanics, known as *maximum entropy*, solves the problem uniquely [132, 133, 8, 178, 26, 258] (see Methods). Intuitively, the approach is to pose a null hypothesis that assumes no prevalence of structure in firing patterns above and beyond the observed pairwise interactions. Specifically, denote the joint distribution of responses of the three cells by $P(A,B,C)$, the pairwise joint distributions by $P(A,B)$, $P(B,C)$, and $P(A,C)$, and the single cell firing rates by $P(A)$, $P(B)$, and $P(C)$. Our null model, $P_{null}(A,B,C)$, must satisfy the single-cell and pairwise constraints. This problem is underconstrained because many different models for the joint activity are consistent with these marginal constraints. The solution is to compute a joint distribution, $P_{pair}(A,B,C)$, which has the maximum possible *entropy* (i.e. least structure) given that it satisfies the marginal constraints. $P_{pair}(A,B,C)$ is a complete null hypothesis for the observed firing patterns[1]. Note that in the two cell case, maximum entropy is equivalent to statistical independence: $P_{null}(A,B) = P_{ind}(A,B)$. The right panel in Figure 5.3b shows the

[1] Selecting the maximum entropy model corresponds to selecting the maximum likelihood model from the family of distributions which satisfy the pairwise constraints; see Methods.

maximum entropy pairwise prediction for all three cells firing at various time offsets. This model accounts for the major features of the 3D cross-correlation, qualitatively consistent with the idea that pairwise interactions alone can explain the temporal structure of synchronized firing in these three cells.

To test the maximum entropy pairwise prediction quantitatively, analysis was restricted to patterns of firing in the same time bin for all three cells (e.g. central peaks in Figure 5.3b). While this analysis does not account for the possibility of complex temporal interactions, it captures the spatial patterns of synchronous activity which dominate both the pairwise and triplet cross-correlograms. A *pattern index* was computed which generalizes the synchrony index (Equation 5.1) to all spike patterns in three cells:

$$Q = \log_2 \frac{P_{obs}(A,B,C)}{P_{null}(A,B,C)} \tag{5.3}$$

In this expression, $P_{obs}(A,B,C)$ denotes the observed probability of a particular three-cell firing pattern. P_{null} represents a null hypothesis for the prevalence of different firing patterns. The index Q indicates how frequently a particular firing pattern was observed, relative to the prediction of the null model P_{null}. Note that in the reduced case of two cells firing at the same time ($A = B = 1$) and a null model of statistical independence ($P_{null} = P_{ind}$), Q is equivalent to the index S in Equation 5.1.

First, the degree of triplet synchronized firing was established by examining deviations from statistical independence. For this analysis, $P_{null} = P_{ind}$. The black symbols in the left panel of Figure 5.4a show the value of Q computed for the firing pattern $(1,1,1)$ in many cell triplets randomly sampled from the mosaic of ON-parasol RGCs shown in Figure 5.2a. The index is

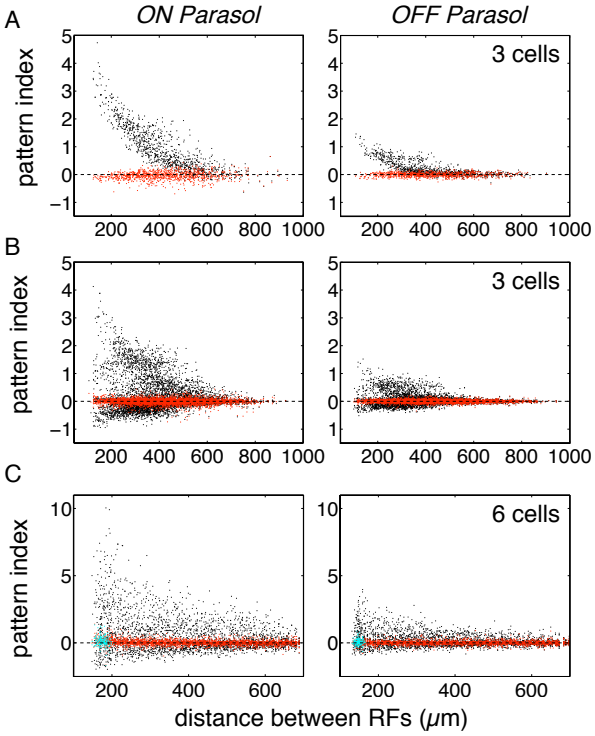

Figure 5.4: Pattern index for multi-neuron firing. (a) Pattern index Q (Equation 5.3) for firing pattern $(1,1,1)$ in groups of 3 cells as a function of the geometric mean of the distances between each pair in the group. Black symbols: pattern index using statistical independence as the null model. Red symbols: pattern index using pairwise constrained maximum entropy as the null model. (b) Pattern index for all 8 firing patterns in groups of 3 cells. Symbol colors as (a). (c) Pattern index for groups of 6 cells. Red and black symbols as (a). Blue symbols: pattern index obtained using the pairwise adjacent maximum entropy model. For the latter, analysis was restricted to local groups of cells conforming to selection criteria described in Methods and containing at least one non-adjacent cell pair.

plotted as a function of the geometric mean of the distances between each pair of cells in the triplet. As with the pairwise synchrony index (Figure 5.2c), Q is large for nearby triplets and approaches zero for widely spaced triplets. Specifically, triplets of parasol cells fired synchronously up to $2^Q \approx 10$ times more frequently than expected from statistical independence. Note that triplets with a large mean distance can sometimes exhibit departures from independence if two of the cells in the triplet are near one another. Similar results are shown for OFF parasol cells in the right panel.

Second, to assess whether pairwise interactions alone account for triplet synchrony, the predictions of the maximum entropy model using pairwise constraints were examined. In this case, $P_{null} = P_{pair}$. The values of Q for this model (red symbols) cluster near the horizontal line at zero, that is, the probability of triplet synchrony is roughly equal to the probability expected from pairwise interactions. Thus, the excess of triplet firing above what is expected from statistical independence is accounted for by pairwise interactions.

5.5 All triplet firing patterns are explained by pairwise interactions

To test the maximum entropy pairwise prediction more fully, analysis was performed on all simultaneous firing patterns for triplets of recorded cells. For example, all cells firing synchronously is represented by $(1,1,1)$, no firing is represented by $(0,0,0)$. The distribution of all 8 possible firing patterns observed in a set of 3 ON-parasol cells is shown in Figure 5.5a. For comparison, Figure 5.5c shows the firing pattern distribution expected from statstistical independence (Equation 5.2), which deviates substantially from the data. Figure 5.5b shows the maximum entropy pairwise prediction, which captures most of the structure in the data.

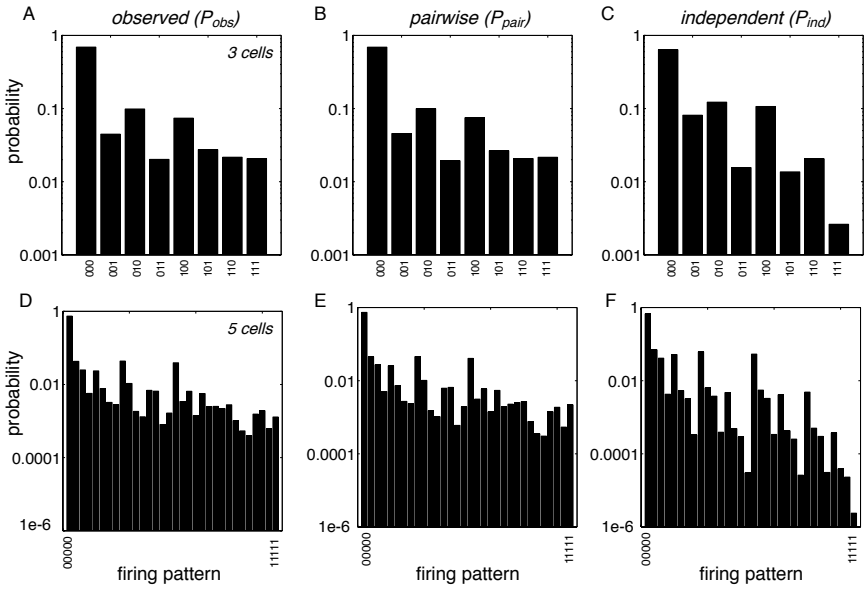

Figure 5.5: Sample firing pattern distributions. Panels (A-C) show firing pattern distributions for 3 ON-parasol cells. Each distribution is shown as a histogram, with the firing pattern indicated by binary digits on the abscissa representing a spike or no spike in each cell, and the probability indicated on the ordinate (note logarithmic scale). Firing pattern distributions were obtained from (A) raw data, (B) the pairwise model, and (C) the statistically independent model (the latter obtained by multiplying the marginal probability distributions for each cell, see Equation 5.2). The likelihood of the data obtained from the pairwise model was 0.99944, from the independent model was 0.94959, and from the empirical model was 0.99955. Distributions in (B) and (C) were fitted to interleaved recordings from the same cells, distinct from the data in (A) (not shown). (D-F) Same as (A-C), but for 5 ON-parasol cells. The likelihood of the data obtained from the pairwise model was 0.99728, from the independent model was 0.92107, and from the empirical model was 0.99836.

To quantify these observations for each firing pattern separately, values of Q were examined for all 8 possible triplet firing patterns. In Figure 5.4b, distinct values of Q for each firing pattern in a triplet of cells are shown with different points. The band of points near the top reproduces the data of Figure 5.4a, that is, the firing pattern $(1,1,1)$. Other patterns occur with greater or lesser frequency than predicted from statistical independence because strongly coupled cells tend to fire together or not at all (see also Figure 5.5a,c) The departure from independence in all triplet firing patterns, evidenced by the large vertical spread of black points, is almost entirely eliminated by taking into account pairwise interactions (red symbols).

To provide a statistical summary of the performance of the pairwise model across all firing patterns, the average *likelihood* of the observed data, P_{obs}, under different models was computed. The likelihood indicates the probability of having observed the data given a particular model. In general, more (less) accurate models exhibit likelihood values approaching 1 (0). To express the likelihood in units that are invariant with respect to the length of the data sample, the average (geometric mean) likelihood per time bin was computed (see Methods). The average likelihood of the data in Figure 5.5a under the independent model (Figure 5.5c) was 0.94959, while the likelihood under the pairwise model (Figure 5.5b) was 0.99944. Although this difference seems modest, the multiplicative accumulation of probability over sequential time bins means that from 60 seconds of data collection one may conclude that the probability of the data having arisen from the pairwise model is more than 10^{133} times larger than the probability of the data having arisen from the independent model. In other words, the enormous difference between the predictive power of the pairwise and independent models is easily distinguished even with modest data sets.

As a benchmark for the likelihood, an empirical model P_{emp} was obtained from the recorded frequencies of all 8 firing patterns in a separate segment of recording from the same retina (the

same recording that was used to fit P_{ind} and P_{pair} above). P_{emp} represents an ideal model for the observed data P_{obs} given the intrinsic reproducibility of the measurement. For the data in Figure 5.5a, the average empirical likelihood was 0.99955. For comparison to the ratio of likelihoods above, the ratio of empirical to pairwise model likelihood was smaller than 2 with 60 seconds of data. Note that the empirical likelihood of the data is not 1, reflecting a combination of finite counting statistics and possible (small) non-stationarity in the neurophysiological recording. Also, note that the empirical likelihood is an upper bound for the performance of any model; as expected, it exceeds the likelihood associated with both the pairwise and independent models. The pairwise model likelihood is very close to this upper bound, while the independent model likelihood is far from it.

The average likelihood was examined for all triplets of cells recorded. The dark blue symbols in Figure 5.6a show the likelihood of the observed triplet firing patterns assuming statistical independence P_{ind}, compared to the likelihood obtained with the empirical model P_{emp}. Again, the likelihood under the independent model is much lower, confirming that the firing of RGCs departs subtantially from statistical independence. In contrast, Figure 5.6b shows that the pairwise model P_{pair} produces likelihood values nearly identical to those produced by the empirical model P_{emp}. Thus, pairwise interactions explain the frequency of triplet firing patterns nearly as accurately as a repeated measurement.

5.6 Multi-cell firing patterns are explained by pairwise interactions

The maximum entropy framework is easily extended to test for interactions in larger groups of cells. For example, for 5-cell firing patterns, the observed firing pattern distribution $P_{obs}(A,B,C,D,E)$ is compared to a maximum entropy null model, $P_{pair}(A,B,C,D,E)$, and a statistically independent

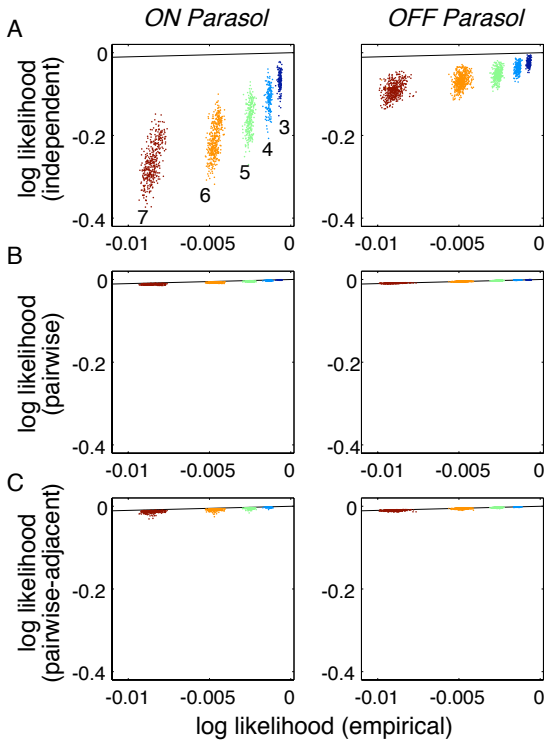

Figure 5.6: Likelihood test of pairwise and adjacent models under constant, spatially uniform illumination. (a) Likelihood of observed data under an assumption of statistical independence as a function of likelihood obtained from an empirical model based on a repeated measurement, for groups of 3,4,5,6 and 7 cells. Diagonal gray line near top indicates equality (note different scales on abscissa and ordinate); large departures from this line indicate substantial failures of statistical independence. (b) Likelihood of observed data in the pairwise maximum entropy model as a function of empirical likelihood. Symbol colors and equality line same as (a). (c) Likelihood of observed data in the pairwise-adjacent maximum entropy model as a function of empirical likelihood. Symbol colors and equality line same as (a). All likelihood analysis was restricted to local groups of cells conforming to selection criteria described in Methods. For (c), analysis was further restricted to groups that included at least one non-adjacent cell pair.

model, $P_{ind}(A,B,C,D,E)$. Figure 5.5d-f shows these three firing pattern distributions for collections of 5 cells. As in the 3 cell case, the pairwise model prediction substantially captures the structure of the observed firing pattern distribution, while the statistically independent prediction does not.

As above, the pattern index was examined to quantify the quality of the predictions. Figure 5.4c shows values of Q for the independent and pairwise models, for groups of 6 cells randomly sampled from the ON and OFF parasol mosaics of Figure 5.2a. Black symbols reveal large departures from statistical independence: values of Q as high as ˜10 indicate firing patterns occurring ˜1,000 more frequently than predicted by chance. Red symbols reveal that these departures are almost entirely accounted for by pairwise interactions. This finding is supported by comparing the likelihood of the observed firing pattern distribution P_{obs} under the models P_{ind} and P_{pair} to the likelihood obtained from the empirical model P_{emp} for groups of 4,5,6, and 7 cells[2]. In all cases, the large systematic failures of statistical independence (Figure 5.6a) are explained by the pairwise model (Figure 5.6b).

In summary, pairwise interactions explain almost all of the departures from statistical independence in parasol cell signals, with a precision comparable to the reproducibility of the measurements. This implies that the structure of multi-neuron firing patterns may be understood with high accuracy based on pairwise connectivity, without postulating more complex interactions. A possible mechanistic interpretation is that frequent multi-cell firing in the retina does not imply widely diverging common inputs [261], but instead can arise from reciprocal connections between, or common inputs to, pairs of cells (see Discussion).

[2]For this analysis and what follows, results from larger groups are not reported because of potential biases due to high dimensionality of the data (see Methods).

5.7 Multi-cell firing patterns are explained by pairwise, adjacent interactions

The next step in simplifying our understanding of the circuit is to test whether pairwise interactions are restricted to immediately adjacent cells, or instead must span larger distances. The mosaic arrangement of receptive fields, which corresponds to the physical arrangement of RGCs in the retina [314, 78], provides a uniquely useful measure of adjacency (Figure 5.2a), and the maximum entropy approach provides a straightforward test of the hypothesis.

Specifically, consider a more restrictive null model for the distribution of firing patterns, P_{adj}. This is the unique maximum entropy distribution subject to the single cell constraints $\{P(A), P(B), \cdots\}$ as before, and pairwise constraints $\{P(A,B), P(B,C), \cdots\}$ obtained *only* from immediately adjacent cells in the mosaic (see Methods). The pattern index obtained from many cell groups with this model are shown with blue symbols in Figure 5.4c. To reduce the effect of adjacent interactions present in the retina but missing in the group of cells analyzed, only groups that uniformly cover a roughly convex area of the retina were considered (see Methods). As a result, the points cover only a small range of distances. Trivial cases in which all pairs are adjacent were excluded. As with the more general pairwise model, the pairwise-adjacent model (turquoise symbols) accounts for almost all the departures from statistical independence (black symbols). Figure 5.6c shows that the likelihood of the data P_{obs} under the pairwise-adjacent model P_{adj} is very similar to the likelihood under the empirical model from a repeated measurement P_{emp}. Comparison to Figure 5.6b shows that the pairwise and pairwise-adjacent model likelihoods are nearly indistinguishable. In summary, pairwise interactions between adjacent RGCs in the mosaic are sufficient to account for almost all multi-neuron firing patterns.

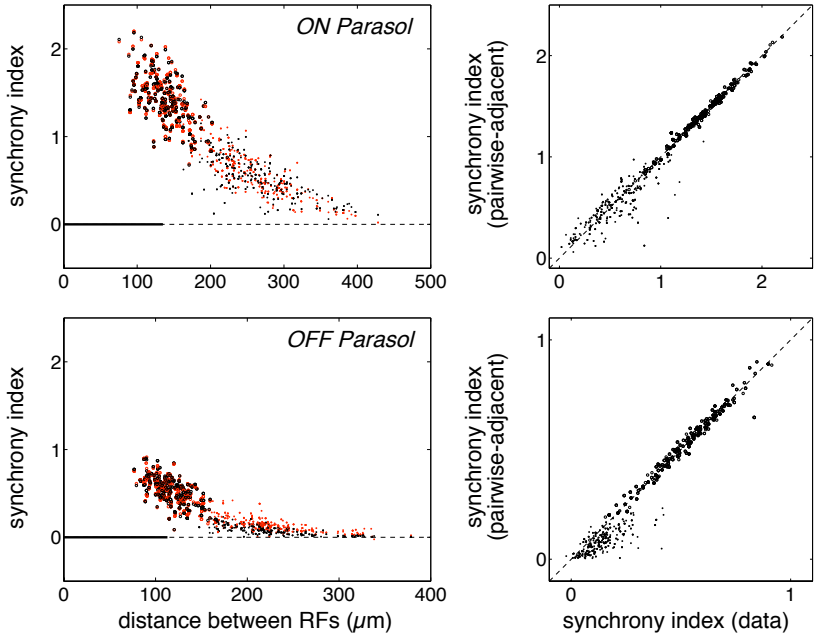

Figure 5.7: Predicted and observed pairwise synchrony index. Left panels show the synchrony index (Equation 5.1) in pairs of parasol cells as a function of distance between their RFs (see Figure 5.2). Black points indicate the observed synchrony index, red points indicate the predictions obtained from the maximum entropy pairwise-adjacent model fitted to groups of $n = 7$ cells. The black bar near the origin represents the modal separation between cells in the mosaic. Right panels show the comparison between data and model predictions for each cell pair tested. In all panels, large open symbols represent cell pairs that are adjacent in the mosaic; small symbols represent cell pairs that are not.

These findings imply that firing patterns in parasol cells can be understood with high accuracy using the simplest possible connectivity illustrated in Figure 5.1d, a dramatic reduction in complexity. A possible mechanistic interpretation of this finding is that pairwise synchrony between non-adjacent cells in the mosaic (e.g. Figure 5.2b) do not necessarily imply long-distance contacts, but instead may be explained by propagation via pairwise connections between adjacent cells (e.g. gap junctions). To test the propagation hypothesis, the synchrony index observed in pairs of cells was compared to the index predicted from the pairwise-adjacent model fitted to cell groups of size $n = 7$ (Figure 5.7). Over the entire range of distances between cells, and across the range of synchrony index values observed, the observed and predicted synchrony index were mostly similar, for both adjacent cell pairs and non-adjacent cell pairs. This is significant because in non-adjacent cells, the pairwise-adjacent model only predicts synchrony as a consequence of synchrony with intermediate cells. Note, however, systematic discrepancies are present, particularly for non-adjacent OFF cells, suggestive of subtle departures from the pairwise-adjacent model.

5.8 Measuring the accuracy of pairwise and pairwise-adjacent models

To quantify how accurately the pairwise and pairwise-adjacent models explain interactions between RGCs, the average log likelihood value $\bar{L}$ shown in Figure 5.6 provides a natural measure. First, larger values of $\bar{L}$ indicate that the observed data are more consistent with the model. Second, it is easily shown (see Methods) that the value $-\bar{L}$ is an estimate of the *Kullback Leibler divergence*, D, between the observed firing pattern distribution, P_{obs}, and the model distribution. The divergence is an information-theoretic quantity that measures the inefficiency of storing the

Table 5.1: Accuracy of pairwise and pairwise adjacent models. Each numerical entry indicates the percentage of departures from statistical independence captured by a specific model, for a given stimulus condition, cell type tested, and time bin size (Δt). Results cited in the text were obtained with $\Delta t = 10$ ms. The range indicates the mean plus or minus 1 SD across several hundred cell groups tested, each consisting of 3-7 cells (in the case of the pairwise model) or 4-7 cells (in the case of the pairwise-adjacent model). For each model, the quantities shown are as follows. Pairwise model: $(D_{ind} - D_{pair})/D_{ind}$. Pairwise-adjacent model: $(D_{ind} - D_{adj})/D_{ind}$. Empirical model: $(D_{ind} - D_{emp})/D_{ind}$.

condition	cell type	Δt	pairwise	pairwise-adjacent	empirical
constant illumination	ON-parasol	10 ms	$98.6 \pm 0.5\%$	$98.3 \pm 1.0\%$	$99.8 \pm 0.1\%$
		5 ms	$97.8 \pm 0.5\%$	$97.5 \pm 1.0\%$	$99.8 \pm 0.1\%$
		20 ms	$99.2 \pm 0.4\%$	$98.9 \pm 0.9\%$	$99.7 \pm 0.1\%$
	OFF-parasol	10 ms	$98.9 \pm 0.3\%$	$98.2 \pm 1.3\%$	$99.4 \pm 0.4\%$
		5 ms	$98.5 \pm 0.4\%$	$97.4 \pm 1.5\%$	$99.0 \pm 0.5\%$
		20 ms	$99.2 \pm 0.3\%$	$98.6 \pm 1.3\%$	$99.4 \pm 0.3\%$
white noise stimulus	ON-parasol	10 ms	$98.6 \pm 0.4\%$	$98.4 \pm 0.9\%$	$99.6 \pm 0.2\%$
		5 ms	$97.8 \pm 0.5\%$	$97.5 \pm 1.0\%$	$99.6 \pm 0.2\%$
		20 ms	$99.1 \pm 0.3\%$	$98.9 \pm 0.9\%$	$99.5 \pm 0.2\%$
	OFF-parasol	10 ms	$98.6 \pm 0.5\%$	$98.3 \pm 0.9\%$	$98.8 \pm 0.7\%$
		5 ms	$98.2 \pm 0.8\%$	$98.0 \pm 1.3\%$	$98.4 \pm 1.0\%$
		20 ms	$98.6 \pm 0.7\%$	$98.3 \pm 1.0\%$	$98.6 \pm 0.9\%$

observed firing patterns using a compression scheme optimized for the model probability distribution [60]. Thus, larger divergence values (smaller values of $\bar{L}$) correspond to a less accurate the model.

The divergence of the independent model, D_{ind}, quantifies the departures from statistical independence in the firing of different RGCs. A natural measure of the success of the models is the degree to which they capture these departures from independence. The index $(D_{ind} - D_{pair})/D_{ind}$ expresses the fraction of the departures from independence accounted for by the pairwise model. On average, this value was ˜99% (see Table 5.1). Similarly, the index $(D_{ind} - D_{adj})/D_{ind}$ expresses the fraction of departures from independence accounted for by the pairwise-adjacent model. On average this value was ˜98%. As a benchmark, the index for the empirical model, $(D_{ind} - D_{emp})/D_{ind}$, was ˜99%. The latter quantity represents the highest value that can be expected given the reproducibility of the data. The departure from independence accounted for by

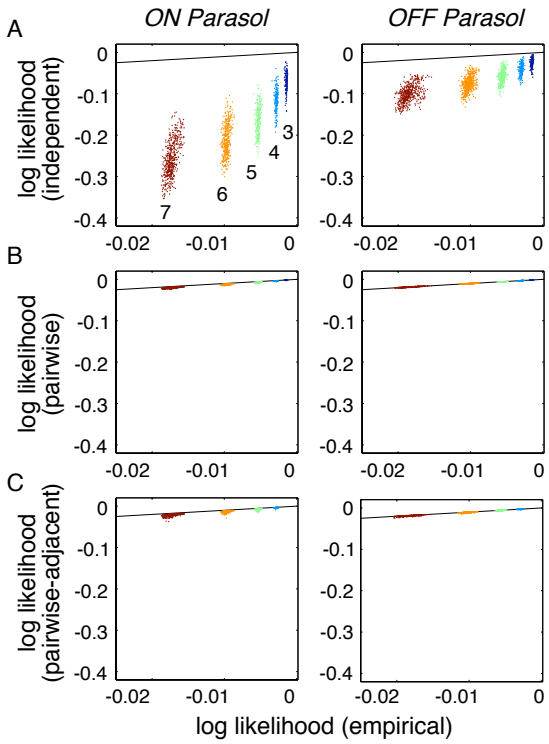

Figure 5.8: Likelihood test of pairwise and adjacent models with a fine-grained random visual stimulus. Panels and symbols as in Figure 5.6.

each model was ˜99% of this benchmark value. In summary, both models almost entirely account for the departures from independence observed in RGC firing.

To test whether these results depend strongly on the time scale of the analysis (10 ms time bins), analysis was repeated with bin sizes two-fold larger and smaller. The results in Table 5.1 indicate that the predictive power of pairwise and pairwise-adjacent models is essentially constant across this range of time scales.

5.9 Multi-cell firing patterns in the presence of visual stimulation are explained by pairwise, adjacent interactions

The data presented so far were obtained with steady spatially uniform illumination of the retina, and thus reflect the circuitry that mediates spontaneous synchronized firing in RGCs. However, it is possible that some contributions to synchronized firing, such as diverging inputs from amacrine cells, arise only in the presence of visual stimuli that vary over space and time. To test this possibility, the maximum entropy analysis was applied to data collected in the presence of the white noise stimulus used for the receptive field measurement (see Figure 5.8). This stimulus provides a wide range of spatial and temporal variations in an experiment of reasonable duration. Note that stimuli with a large spatial scale would be expected to introduce higher order correlations by simultaneously activating multiple RGCs. This would confound the analysis because synchronized firing could be produced by the stimulus, the retinal circuitry, or both [257]. This problem was avoided by using a stimulus with independently modulating pixels that were small relative to the parasol cell receptive field. In these conditions, the pairwise model captured ˜98% of the departures from independence, the pairwise-adjacent model captured ˜98%, and the empirical model benchmark captured ˜99% (see Table 5.1). Again, the models accounted for ˜99% of the departures from independence that were reproduced by the empirical benchmark. Thus, even in the presence of a dynamic, spatially varying stimulus, pairwise and adjacent models almost entirely account for the departures from independence observed in RGC firing.

5.10 Sensitivity of maximum entropy analysis for detecting non-pairwise, non-adjacent circuitry

Pairwise and adjacent connectivity clearly can explain most of the observed interactions between parasol RGCs. However, without direct experimental manipulation, it is impossible to draw firm conclusions about the structure of retinal circuits that underlies this statistical observation. A first step, however, is to ask: how sensitive is the maximum entropy analysis to departures from pairwise and adjacent connectivity? This question was approached by testing the sensitivity of the analysis to artificial perturbations of the data, in two ways.

First, the analysis was applied to artificial data obtained from a purely pairwise (or pairwise-adjacent) model, with varying amounts of common input added to simulate departures from the model. Specifically, a maximum entropy pairwise distribution P_{pair} was fitted to the observed data from a group of $n = 7$ RGCs. A hypothetical common input to all n cells was then simulated, occurring randomly with probability $0 < r < 1$ in each time bin, and generating a spike in each RGC with efficacy expressed as a probability p. If $(x_1, \ldots, x_n)$ is the binary firing pattern for n cells, then define $m = \sum_i x_i$ to be the total number of spikes in the firing pattern. The common input alone would produce a particular RGC firing pattern containing m spikes with probability:

$$P_{common} = \begin{cases} rp^m(1-p)^{n-m} & m > 0 \\ (1-r) + r(1-p)^n & m = 0 \end{cases}$$

P_{common} is the probability distribution of firing patterns created by the non-pairwise common input. The effect of this common input was simulated by calculating the distribution of firing

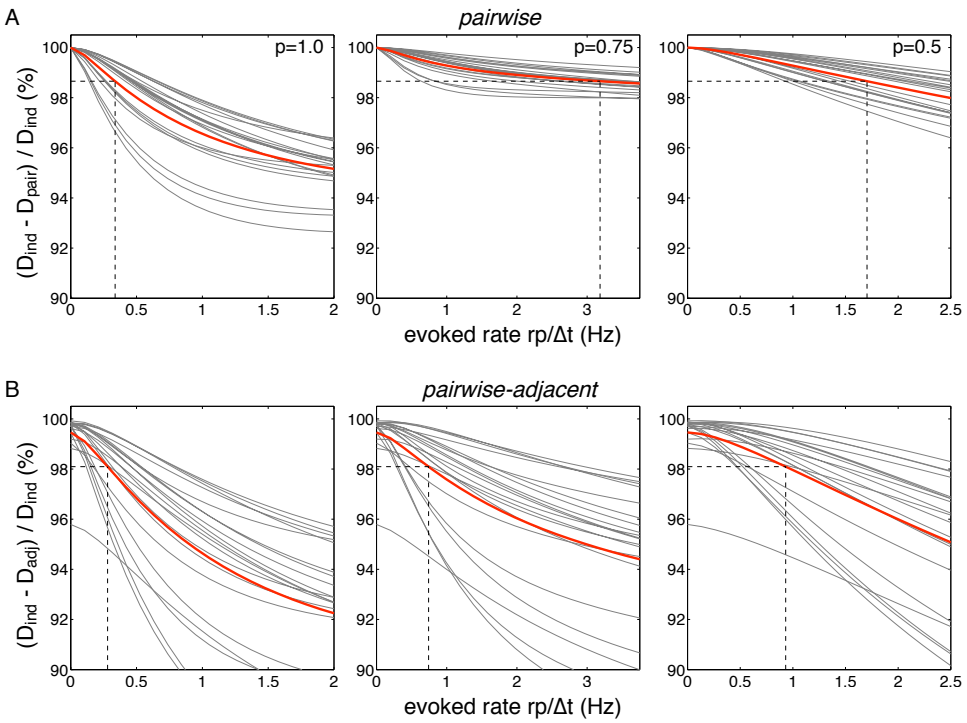

Figure 5.9: Sensitivity of maximum entropy analysis. Each panel shows the sensitivity of the maximum entropy analysis procedure for detecting a hypothetical non-pairwise, non-adjacent common input. The hypothetical input occurs at a rate r and causes a spike in each of $n = 7$ RGCs with a probability p. Results are shown for common input over a range of values of r and p added to simulations obtained with either the pairwise (A) or pairwise-adjacent (B) model fitted to data. In each case, the abscissa indicates the average evoked rate in the simulated RGCs, which is determined by r and p. The ordinate indicates the fraction of the departures from statistical independence accounted for by the pairwise or pairwise-adjacent model. Each gray trace shows the results obtained from a single group of ON-parasol cells; red traces indicate the average across all 20 groups. In each panel, the rate of common input r required to reproduce the average value observed in the original data was converted to the equivalent evoked rate and is indicated by a dashed line.

patterns expected from the logical OR combination of spikes from the firing patterns produced by the common input distribution, P_{common}, and the pairwise distribution, P_{pair}. This resulting simulated firing pattern distribution contains structure with systematic departures from pairwise interactions.

To assess the sensitivity of the pairwise model to common input, the degradation in performance of the model was measured as a function of the putative input rate r in the simulation. Specifically, a new pairwise model was fitted to the simulated data, and the fraction of departures

from statistical independence accounted for was computed. In the case of $r = 0$ (no common input), this value was 100%, because the pairwise model computed from the simulated distribution exactly reproduces the original P_{pair}. As Figure 5.9 demonstrates, the pairwise model is indeed sensitive to common input: this value systematically drops from 100% as the input rate r increases.

To assess the possible degree of common input in the recorded data, the difference between the fraction of departures from independence accounted for by the empirical and pairwise model was measured. This captures the failures of the pairwise model that are not accounted for by the lack of reproducibilty in the data. This difference was then subtracted from 100%, and the input rate r which produced an equivalent reduction was identified from the curves in Figure 5.9. This procedure is diagrammed with dashed lines in Figure 5.9 and measures the rate of common input that is consistent with the observed data.

With a common input of strength $p = 1$, an input rate of $r = 0.0034$ (equivalent to an evoked spike rate $rp/\Delta t$ in each target RGC of 0.34 Hz) produced a reduction in the fraction of departures of independence accounted for by the pairwise model equal to the value observed in the data (Figure 5.9a). The data are not consistent with a common input occurring at a rate higher than r, because r subsumes any discrepancy between model and data. For comparison, the mean firing rate of the recorded ON-parasol cells was 10.7 Hz. Similarly, for the pairwise-adjacent model, an input rate of $r = 0.0028$ (equivalent to an evoked RGC spike rate of 0.28 Hz) produced a value equal to the value observed in the data. As expected, for weaker common input (lower p), higher evoked rates were consistent with the values observed in the data (Figure 5.9b,c). This is because lower values of p produce a much smaller proportion of multi-cell firing patterns. In summary, the data indicate that at most a small fraction of the observed spikes in RGCs could be produced by widely diverging common inputs in the retinal circuit.

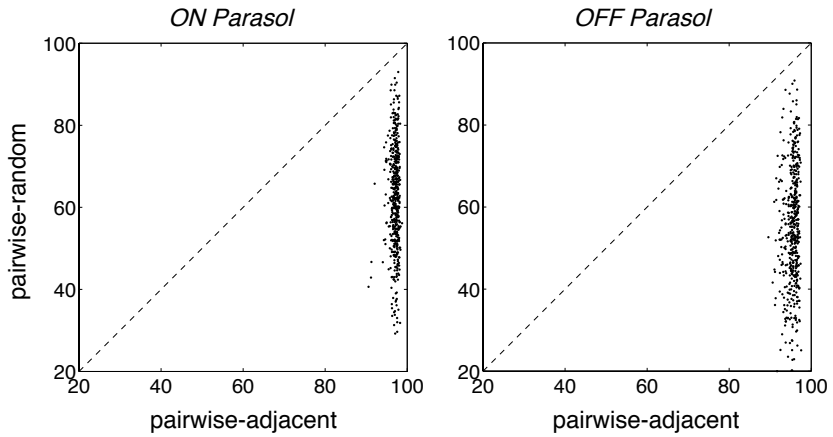

Figure 5.10: Sensitivity of maximum entropy analysis for detecting non-adjacent interactions. Each panel shows the fraction of departures from independence accounted for by the pairwise analysis restricted to a random subset of cell pairs, equal in number to the number of adjacent cell pairs, as a function of the fraction accounted for by the original pairwise-adjacent analysis. Each point represents the results for a single groups of $n = 7$ ON or OFF parasol cells. Dashed lines indicate equality.

A second test of the sensitivity of the maximum entropy approach was focused on the importance of adjacent interactions. The performance of the pairwise-adjacent model P_{adj} was compared to the performance of an alternate model. The latter was the maximum entropy distribution subject to the same single cell constraints $\{P(A), P(B), \cdots\}$ as P_{adj}, but with pairwise constraints $\{P(A,B), P(B,C), \cdots\}$ obtained from a *randomly selected* subset of k cell pairs, where k is equal to the true number of adjacent cell pairs in the group. This pairwise-random model uses the same number of constraints as the pairwise-adjacent model, but ignores the true spatial layout of recorded cells. The fraction of the departures from statistical independence accounted for by the pairwise-adjacent model, $(D_{ind} - D_{adj})/D_{ind}$, is compared to the corresponding statistic for the pairwise-random model in Figure 5.10, for collections of $n = 7$ ON and OFF parasol cells. The pairwise-random model exhibits substantially reduced capacity to explain the departures from independence in the data, spanning a range of performance of roughly 20-95%, rather than the values of roughly 97-99% exhibited by the pairwise-adjacent model. As expected, a few of the values approach parity with the pairwise-adjacent model: by chance, some of the random

samples will coincide with the truly adjacent pairs. These results indicate that the accuracy of the pairwise-adjacent model is not an artifact of limitations in the analysis, but instead hinges critically on the true spatial layout of recorded cells, confirming that adjacent interactions are of particular importance in understanding multi-neuron firing patterns.

5.11 Discussion

Our central finding is that multi-neuron firing patterns in parasol RGCs of primate retina can be explained accurately by purely pairwise interactions restricted to adjacent cells in the mosaic. This is consistent with the simplest possible model in Figure 5.1, and provides a parsimonious functional description of retinal network activity. A major practical implication for future work is that large-scale visual signals conveyed from the primate retina to brain can be understood on the basis of measurements from individual cells and pairs of adjacent cells. However, the limits of this interpretation, and the implications for retinal circuitry, must be approached with caution. Below, we first discuss several implications, and then return to consider the caveats.

First, the existence of multi-neuron synchrony in large collections of RGCs does not imply complex circuitry. Previous work suggested that such synchrony reflects widely diverging input from a presynaptic interneuron, such as an amacrine cell [261]. The present findings indicate that, at least in parasol cells, functional connections between pairs of adjacent cells can explain the observed synchrony. Note that this finding does not identify the mechanisms of synchrony. Previous evidence implicates a combination of mechanisms: direct gap junction coupling between neighboring RGCs [125, 119, 262, 41, 306], gap junction coupling through intermediate amacrine cells [65, 130, 306], and chemical synapses providing common input from bipolar or amacrine cells [181, 41] (and see [77, 125]). The present findings do not refine this picture, instead, they

reveal the circuit organization of these mechanisms in large groups of RGCs. Specifically, the following kinds of connectivity are not required to explain synchrony: (1) presynaptic common input to multiple RGCs or non-neighboring RGCs in the mosaic, or (2) reciprocal connections via intermediate cells that contact multiple or non-adjacent RGCs.

Second, the present results suggest that spatial scale of connectivity between RGCs is smaller than the spatial scale of physiological interactions. Specifically, synchronized firing clearly extended to pairs of cells that are not adjacent in the mosaic (Figure 5.2c), but this synchrony could be explained by interactions between adjacent cells. Thus long-range contacts, such as gap junctions at the tips of dendritic arbors (which overlap considerably in parasol cells [65]) or signals propagating through wide-field amacrine cells, are not required to explain synchrony. Instead, synchrony could be caused by propagation of signals through a chain of adjacent cells in the mosaic, for example, through proximal gap junctions or narrow-field amacrine cells. Again, this finding does not uniquely identify the mechanism.

There are several caveats to the interpretations above. First, as with any model, the conclusions one may draw about retinal circuits are limited by the fact that small non-pairwise or non-adjacent interactions cannot be entirely excluded in any finite data set. The degree to which the data quantitatively exclude such interactions are revealed by the sensitivity analysis presented in Results. Second, there are theoretical limits on what can be concluded about circuitry based on correlated firing patterns. For example, widely diverging Gaussian inputs can produce purely pairwise multi-neuron statistics. Third, only spontaneous activity and responses to a simple, fine-grained visual stimulus (white noise) were examined. It remains possible that more complex interactions, over longer distances, occur in the presence of patterned visual stimulation with more natural structure, as has been suggested in previous work [188, 210, 261, 148]. A test of this

possibility will require shuffle-correcting to control for multi-cell synchrony induced by stimuli covering multiple receptive fields. Fourth, analysis was restricted to parasol cells of the primate retina, which are efficiently sampled in the present recordings. It remains possible that different cell types, and retinas of different species, exhibit more complex interactions. Finally, the present work focused on spatial patterns of activity at a single point in time. It remains possible that complex temporal patterns are introduced by interactions that are not pairwise or not adjacent. These are important avenues for future work, and the maximum entropy framework can be extended to address many of these issues.

Although maximum entropy approaches have a long history in several fields, their application in neuroscience is fairly new. Recent theoretical work has set the stage [8, 178, 258], and one group has applied the approach to recordings from salamander and guinea pig retina and cultured cortical networks, concluding that pairwise interactions explain roughly 90% of network interactions [258, 259]. The present work provides several conceptual and technical advances. First, analysis was restricted to interactions between known morphological and functional types of RGC, in macaque monkey retina, and explained a substantially higher proportion of network interactions (˜98-99%). Second, analysis was restricted to neighboring cells in the mosaic, providing a spatial constraint on pairwise interactions within each cell type. Third, the model was cross-validated (constrained by one data set and evaluated on another) to avoid overfitting which can produce accurate model fits that do not generalize. Fourth, responses were measured in the presence of a steady, uniform stimulus and fine-grained white noise stimulus, rather than nautrialistic stimuli or modulating uniform stimuli; the latter have coarse spatial structure and and thus would be expected to produce significant departures from pairwise statistics. Finally, sensitivity analysis provided a bound on interpretation of the model in terms of network connectivity, and

suggested that even fairly high prediction accuracy (e.g. 90%) can be consistent with substantial non-pairwise interactions in the retinal circuit.

The present findings suggest an approach to understanding the function of many large circuits in the brain, to the degree that recording technology permits. For example, the possibility of complex interactions between cells within and across columns in the neocortex [299, 59], or between many hippocampal neurons involved in storing spatial memories [321], limits our capacity to understand these critical circuits. In the present work, an extremely simple pattern of connectivity sufficed to explain widespread synchrony in the retina. In some systems, such as gap-junction coupled networks in the thalamus and cortex (see [61]) or inferior olive [167], the present approach may translate essentially unmodified to test whether electrical coupling can fully account for network interactions. In other systems, interactions are likely to be more complicated. For example, cortical neurons may exhibit highly specific interactions dependent on layer and cell type [331, 332], resulting in complex firing patterns. The maximum entropy method is readily extended to measure the complexity of the underlying circuits. Specifically, hypothesized constraints on connectivity that emerge from anatomical considerations can be included in computation of the maximum entropy distribution, allowing a direct test of whether they account for recorded multi-cell firing patterns. For example, the approach could be used to test whether interactions are restricted to small groups of cells ($N = 2,3,4,\ldots$), or to cells over a specific length scale such as a cortical column. The approach factors out the influence of signals propagating through intermediate cells, which otherwise would confound the analysis of group size or spatial scale. Importantly, the methods can be used with measurements of spontaneous activity in circuits such as acute slices in which natural exogenous stimulation is not possible. With the increasingly widespread use of multi-electrode recordings and optical methods *in vivo* and *in vitro* in many

nervous system structures (e.g. [208, 321, 59, 22, 225, 207, 40, 323]), the importance of understanding the complexity of network interactions has grown tremendously. Thus, extensions of the present approach may prove useful for understanding functional connectivity in other neural circuits.

This chapter is taken from J Shlens, GD Field, JL Gauthier, MI Grivich, D Petrusca, A Sher, AM Litke & EJ Chichilnisky, (2006) *The structure of multi-neuron firing patterns in primate retina.* **Journal of Neuroscience**, 26(32): 8254-8266.

Chapter 6

Islands of Large-Scale Concerted Activity in the Primate Retina

6.1 Introduction

Synchrony between pairs of neurons is a prevalent mechanism exploited by early sensory systems [162] and higher cortical areas [87]. In parallel, the observation of synchrony and correlations in spike trains has provided strong clues about connectivity between pairs of neurons and neural circuits in general [300]. Historically, these questions have been examined in detail using paired recording techniques [227], however, with the advent of multi-neuron recording techniques, these questions must be revisited in the context of more than two neurons [45]. Intuitively, such recordings should provide vastly improved insight into how information is represented in a neural population as well as the underlying neural circuitry. Unfortunately, these issues are difficult to explore because of the inherent high-dimensionality of the data and the difficulty in positing plausible, constrained models of multi-neuron activity.

Mammalian retina provides an important system to explore such issues because the consequences of circuitry generating multi-neuron correlation has profound implications on the representation of visual information. Furthermore, unlike higher cortical areas, the neuroanatomy of the retina is well characterized and dedicated technologies exist for recording from large populations of neurons at a single cell, sub-millisecond resolution [166, 266]. Importantly, the electrical activity of populations of retinal ganglion cells (RGCs) constitute the neural code for visual information from the eye to the brain [243]. Deciphering the structure of correlated activity in this population code could have a tremendous influence on how visual information is represented. For instance, the neuroanatomy of the retina suggests at least two theories on the origin of correlated activity that have distinct consequences on the transmission of visual information.

Synchrony between a pair of cells could result from an underlying interneuron (e.g. amacrine cell) and thus reflect a apertured view of a larger pattern of correlated activity driven by this common input. The "electrical footprint" of an interneuron could multiplex the activity of RGCs to provide a mechanism for convey fine spatial visual information, spatial constancy or a looming sensation [191, 189, 148, 129]. Conversely, synchrony could arise from electrical coupling known to exist between neighboring RGCs [119, 125, 65, 130] and provide a mechanism for sensitivity at low light levels [65]. Although both mechanisms should produce multi-neuron correlated activity, the latter through the propagation of activity, an important distinction exists between the observation of both types of circuits. The former mechanism adds a level of complexity to a neural circuit because it necessitates simultaneously recording from every RGC downstream of an interneuron to characterize its activity. The latter mechanism is a rather parsimonious because the local strength of interactions is sufficient to explain the activity of the entire population. Thus, characterizing the spatial and numerical scale of correlated activity could provide important constraints about what

types of circuit mediate multi-neuron activity and the consequences this activity has on coding visual information.

Examining the complete structure of correlation in large neural populations is impossible in a finite experiment because the number of potential firing patterns is too large to sample. This technical limitation, however, does not obviate the need to provide some characterization of large-scale activity, as few results exist the literature [261, 128] although several predictions exist [259, 273]. We focus our attention on the spatial and numerical scale of simultaneous correlated activity of complete populations of RGCs of a single known cell type because such statistics can be estimated well in a finite experiment, constrain cell-type specific circuitry, and discern the quality of quantitative models for this activity.

The characterization of the large-scale activity of a neural population motivates some attempt to model the activity in a parsimonious manner. A parsimonious solution is to search for models that reduce the inherent dimension of multi-neuron activity guided by some biological structure. Often, dimensional reduction has been performed to account for *temporal correlation* to make the estimation of the model tractable (e.g. [233, 298]). In these cases complex dynamics of ionic channels are reduced to finite parameterizations of surrogate internal currents. In contrast, in the case of *spatial correlations*, anatomical investigations guide dimensional reduction of the underlying neural circuit. In this case, RGCs are known to couple with gap junctions to physically adjacent cells of the same type [65, 119] (and other amacrine cells [65, 130]). Deriving a statistical model exploiting this dimensional reduction to predict the multi-neuron activity is subtle [261] but by extending previous work [273], we find that such a model can explain the activity of the complete neural population. This model corresponds precisely to a nearest neighbor Ising model from statistical mechanics which permits an interpretation of the parameterization and allows us

to visualize and quantify the strength of the complete network activity.

6.2 Methods

Action potentials were recorded extracellularly from retinal ganglion cells (RGCs) in isolated macaque monkey retina perfused with a physiological saline solution on an array of 512 electrodes [166, 99]. The receptive field of each RGC was identified using reverse correlation with a white noise stimulus. Cells were segregated into distinct functional classes according to their receptive field characteristics. ON parasol cells, which project to the magnocellular or visual motion-sensing, were identified by their size and response kinetics [54].

RGCs of a particular functional class independently tile all of visual space as expected from previous anatomical studies [312, 310]. This feature is reflected in the nearly hexagonal lattice of receptive fields outlines derived from Gaussian fits across four retinas (Figure 6.1). The completeness of these mosaics reflect the fact that nearly all ON parasol cells have been recorded in this region of 4 by 8 degrees of retina ($n = 104$, 66, 65 and 54 neurons, respectively). Data from the first preparation have been used in prior work examining small-scale multi-neuron firing patterns [273].

6.3 An archipelago of spontaneous multi-neuron firing patterns

A large body of literature has consistently demonstrated that pairs of RGCs are not statistically independent and fire nearly simultaneously even in the absence of visual stimulation [12, 191, 41, 259, 129, 119, 206, 13, 4, 125, 77, 11, 181, 182, 183, 273] (e.g. Figure 6.2c). The observation of synchrony between pairs of cells, however, is an apertured view of larger patterns of activity occurring in a neural population. To investigate such questions, we examined the spatial

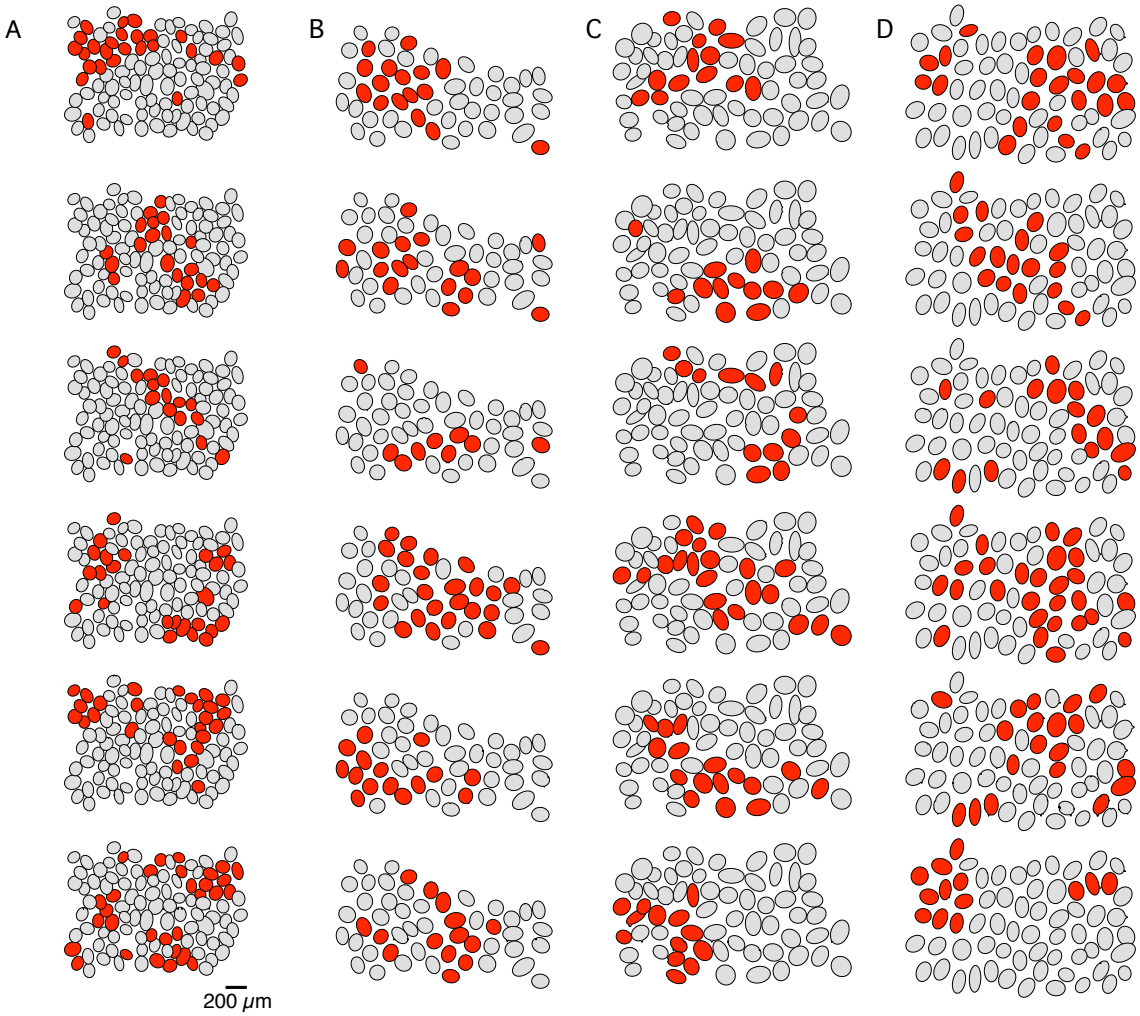

Figure 6.1: Islands of large-scale concerted activity in populations of primate ON parasol RGCs across four preparations (a-d). Each oval represents the 0.9, 1.0, 1.2 and 1.0 SD outline of the Gaussian fit to the receptive field in each preparation, respectively. If a neuron spikes within a 10ms moment in time, the receptive field is colored red. Shown are six selected frames out of several hours of activity from each preparation (Supplementary Material).

organization of spontaneous activity across a single population of RGCs in response to constant, photopic light. We visualized the population activity of all ON parasol cells by generating movies of spiking activity (Supplementary Materials) in which each cell's receptive field outline was colored red during the presence of a spike within a brief time period (10 ms; width of cross-correlation in Figure 6.2c). Selected movies frames of population activity are shown across four preparations (Figure 6.1a-d, respectively).

Figure 6.1 highlights several important features of the simultaneous activity. The most striking observation is that synchrony between a pair of cells (two cells colored red) is often a subset of larger patterns of simultaneous activity. In particular, over several hours of recording, firing patterns extend up to 46 neurons, or 44% of the population. Furthermore, a majority of the firing patterns occur in spatially localized islands of activity consisting of up to 39 neurons, or 38% of the population. The spatial contiguity of the patterns indicate that the mosaic layout of this neural population, dictated by the cell type, fundamentally shapes the structure of the correlated activity.

Qualitatively, this activity bears resemblance to percolating activity often observed in other physical media [126] exhibiting no pronounced moments in time when a repeated motif or stereotyped pattern of activity occurs. In particular, the lack of repeated, stereotyped events is quite distinct other forms of large-scale, spontaneous *in vitro* activity observed including neuronal avalanches [22, 23] and cortical songs [128]. This qualitative description can be made precise by noting that no distinct boundaries exist in the population activity as indicated by translation and angular invariance of correlations between pairs of cells. The strength of pairwise correlation, measured by the correlation coefficient [270] is largely dictated by the distance between the pair of cells and invariant to cell body location (Figure 6.2a). Likewise, additionally plotting this relation-

ship as a function of angle between pairs of neurons indicates no direction that is systematically favored (Figure 6.2b). The translation and angular invariance imply that no sharp boundaries exist and this activity is spatially isotropic.

Systematically investigating all forms of correlated activity is beyond the goal of this paper, thus we choose to focus our attention on the simultaneous activity that occurs on the time scale of the width of the cross-correlation (Figure 6.2c). The time scale of 10 ms emphasizes the significant synchronous peak in pairwise correlations as well as account for the refractory period (Figure 6.2d). To assess the amount of correlations existing in the spatial structure, we calculate the fraction of second-order correlations accounted for in the simultaneous activity within 10ms. Simultaneous correlations account for an average 83% of the variance about the free firing rate in cross-correlations (Figure 6.2e). In contrast, simultaneous activity accounts for 42% of the variance in the auto-correlation (Figure 6.2e) indicating serial correlation between successive frames of binned time (Supplementary Materials). We ignore these temporal effects and focus the remainder of this manuscript on characterizing the spatial organization of correlated activity.

6.4 Spatial and numerical scaling of correlations in a complete neural population

A precise characterization of all concerted activity in an entire neural population requires examining the relative frequency of every firing pattern. In a population of n neurons there exist 2^n firing patterns making a complete characterization of the four preparations in Figure 6.1 infeasible in a finite experiment (e.g. $2^{104} \sim 10^{30}$ patterns). This technical obstacle does not obviate the need to characterize the activity of large populations of neurons. Thus, we must resort to mea-

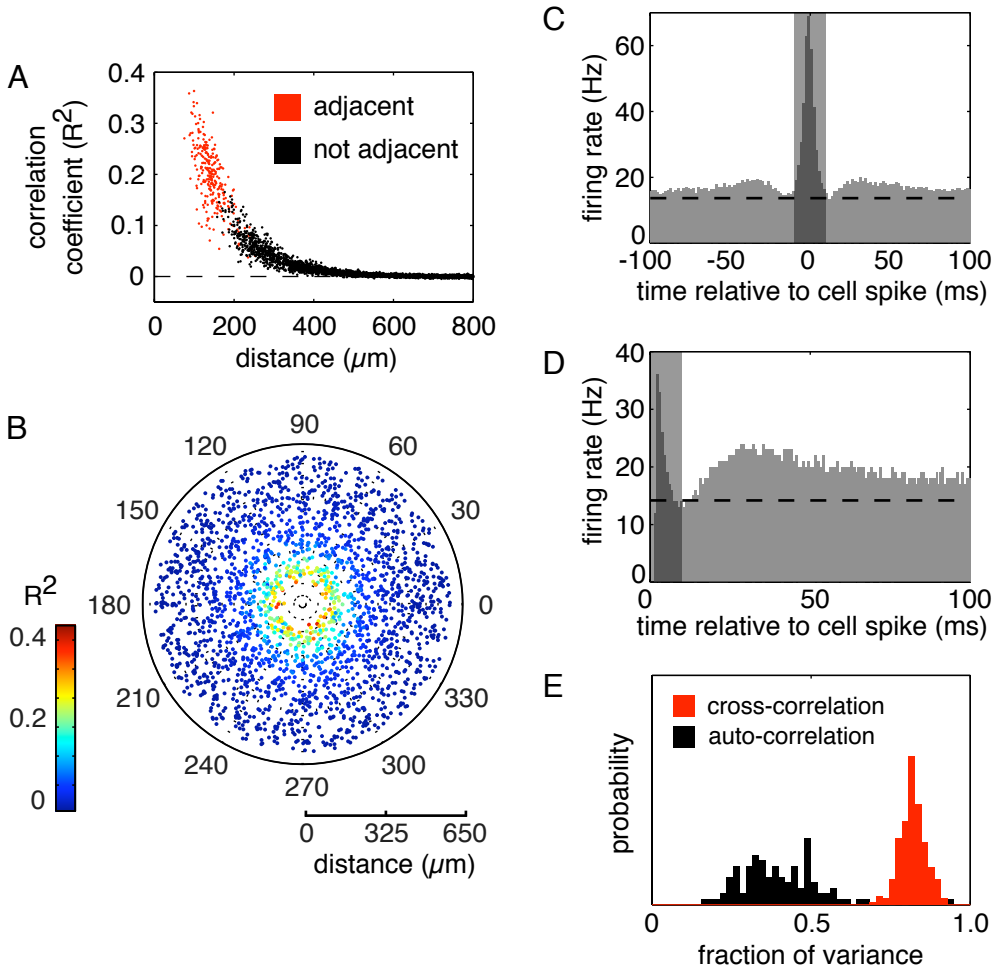

Figure 6.2: Homogeneity and magnitude of simultaneous pairwise correlations. (a) Correlation coefficient (R^2) between binned spike trains (10ms) of all pairs of neurons plotted as a function of distance. Adjacent cells labeled in red (see Methods). (b) Previous panel additionally plotted as a function of angle between pairs neurons. Color bar indicates magnitude of correlation coefficient. (c) Cross-correlation between typical pair of adjacent RGCs expressed as the firing rate of the neuron. Dashed line represents free firing rate of neuron and gray shadow indicates width of selected bin time (10 ms). (d) Auto-correlation of typical neuron. Dashed line and shadow as panel (c). (e) Fraction of variance about free firing rate within 100ms period contained in binned simultaneous activity (10ms).

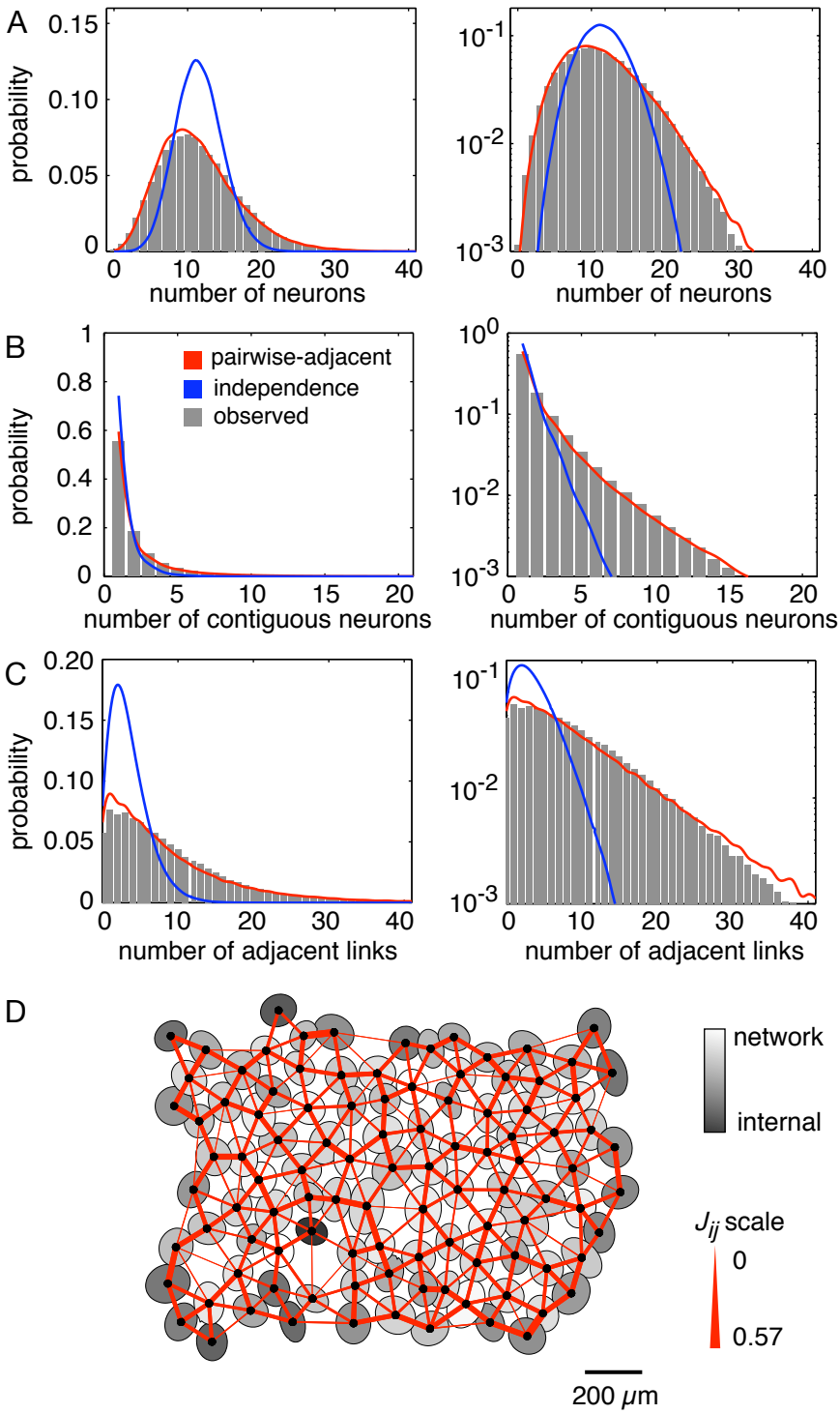

Figure 6.3: Large-scale statistical features of neural population in Figure 6.1a. (a) Distribution of the number of neurons firing observed in cross-validated data set (gray) and predicted from statistical independence (blue) and pairwise-adjacent model (red). Error bars indicate bootstrapped variance measures. Right panel is same data but logarithmically scaled. (b) Distribution of the number of spatially contiguous neurons firing and (c) the distribution of the number of active, adjacent links (see Methods). Panels and colors as in (a). (d) Visualization of inferred network architecture in pairwise-adjacent model. Thickness of red lines measures strength of Ising interaction terms J_{ij}. Grey-scale color of cell measures $h_i^{net} - h_i$ or whether the cell's activity is dominated by the network or internal drive. (Section 6.6)

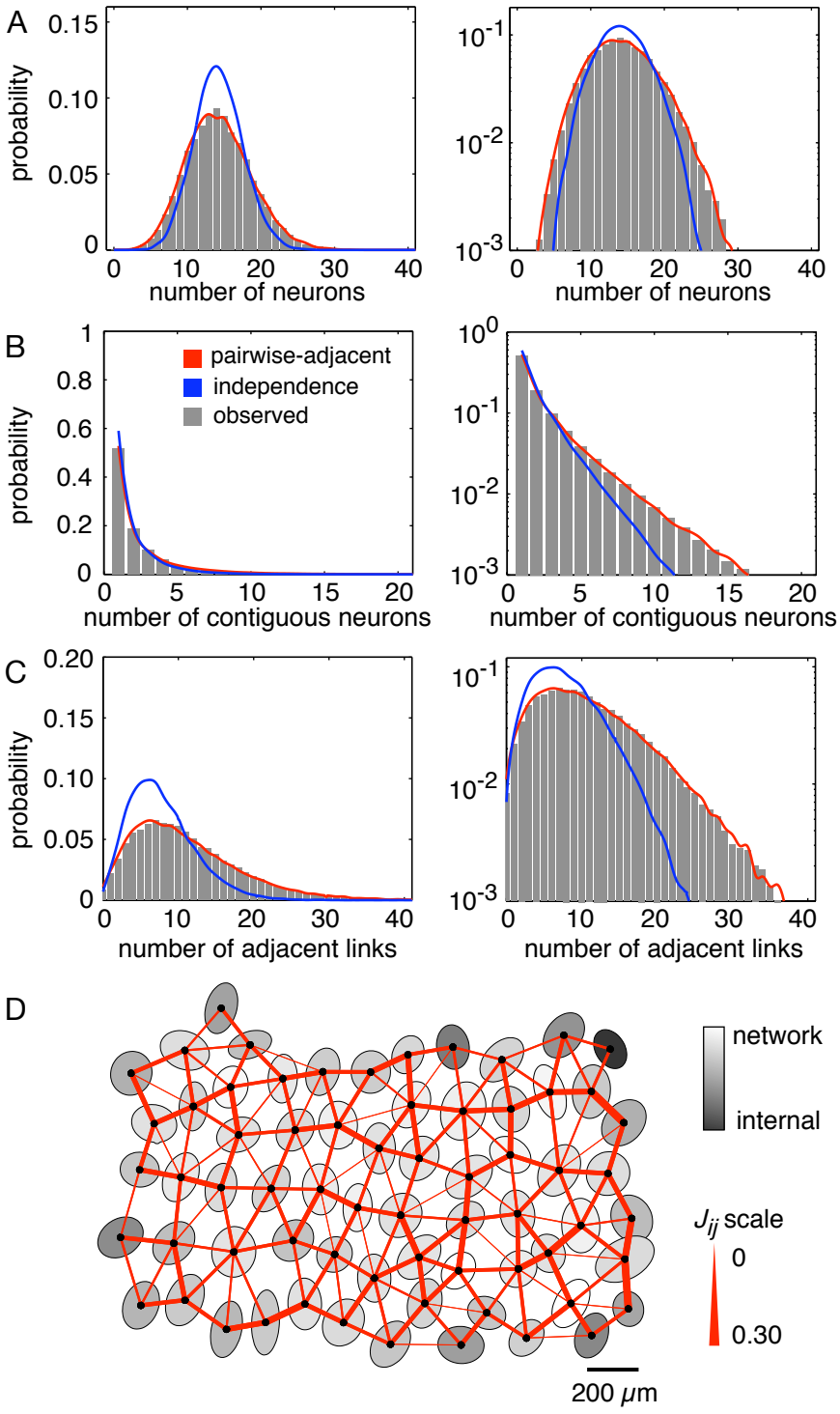

Figure 6.4: Large-scale statistical features of neural population in Figure 6.1d. Panels and colors same as previous figure.

suring features of the firing patterns leveraging our strong prior knowledge about the structure of the neural activity and the types of retinal circuits which might mediate this activity [310, 245]. Ideally, these features of the firing patterns should be well estimated in a finite experiment, constrain hypothesized retinal circuits, sample the frequency of higher order correlations and discern the quality of quantitative models [273, 259].

Simple features of the distribution permit us to ask what the spatial and numerical scale of the interactions are. For instance, one could imagine that spatial correlations might extend beyond our recording techniques if we had used more traditional multi-electrode technology [54], let alone paired recordings [184]. To address this question we examined how the size of islands of activity scaled as we systematically sub-sampled the number of contiguous neurons in a mosaic. The size of an island is defined as the number of contiguous adjacent neurons firing simultaneously (see Methods). For instance, in the bottom panel of Figure 6.1d, we find islands of size 10 and 3. We summarize this distribution with the mean island size, expressed as a fraction of the number of neurons sampled. This statistic asymptotes as one examines larger mosaics indicating that we capture the spatial scale of the correlated activity using our recording techniques (Figure 6.5a). Note for comparison the average number of neurons recorded using previous multi-electrode technology (n = 20) [54]. These curves lie on top of one another indicating that the size of islands, and presumably the underlying neural circuits, are conserved numerically across retinal preparations.

Focusing on the spatial and numerical scale of the activity, we examine three features of the firing patterns from the complete distributions: (1) the number of neurons firing, (2) the number of neurons composing spatially contiguous islands and (3) the number of active adjacent links. The first statistic is sometimes termed the *summed population code* ignoring the identify of which neurons spiked [240]. The second statistic was discussed previously. An active adjacent link is

defined as an edge connecting two spatially adjacent neurons in which both neurons are firing. For example, in the bottom panel of Figure 6.1d, we find 13 neurons firing, islands of size 10 and 3 and 18 active adjacent links. The distribution of these features across the entire recording are plotted for two preparations in Figure 6.3a-c and 6.4a-c (grey bars). Note that the number of neurons in the ordinal axis is far less than the total number of neurons in each population. Thus, at no moment in time are a large fraction of neurons or spatially contiguous neurons firing simultaneously. Cumulatively, in the preparation from Figure 6.3a, over 99.9% of the time, no more than 31 neurons (30% of population) fire simultaneously and no more than 15 spatially contiguous neurons (14% of population) fire simultaneously. (Please note in retrospect that the frames in Figure 6.1 are judiciously selected to highlight the spatial scale of the activity.) The distribution of these features place a strong bound on the numerical and spatial scale of any excitatory circuit driving this population of neurons. If one posits that an underlying interneuron projects to a spatially contiguous group of ON parasol cells, this circuit drives no more than 15 neighboring neurons simultaneously [191].

A common benchmark for examining the strength of correlations in a population of neurons is to compare the observed correlations to predictions generated from statistical independence [259, 273]. We can generate predictions of these statistics based on the measured firing rates of all neurons expressed as probabilities. In Figures 6.3a-c and 6.4a-c, (blue curves), the distribution of these features from a statistically independent model differs sharply from the observed features. The discrepancy, which can be as large as 10-100 fold, highlights the sensitivity of these features to discriminate the presence of correlations as well as the strength of the correlations.

While these statistics are useful for characterizing the strength of the network activity, one might want to look directly at the contributions of higher order correlations [126]. In the

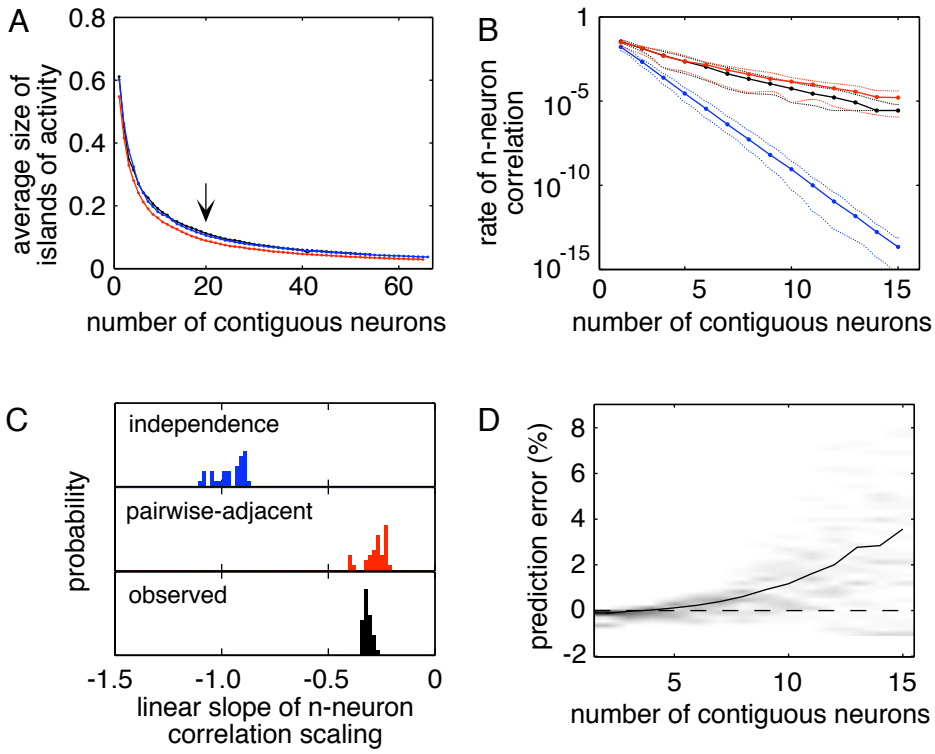

Figure 6.5: Higher order correlations in neural population. Subsets of contiguous neurons are selected from the complete neural population and systematically enlarged (see Methods). (a) Average size of islands of contiguous neuron firing patterns, expressed as a fraction of the total number of neurons in the population. Each color represents individual retina. Arrow represents number of neurons in typical multi-electrode recordings [54]. (b) Rate of n-neuron correlations in mosaics observed (black) and predicted from statistical independence (blue) and a pairwise-adjacent model (red). Dotted lines represent variance across 33 mosaics. (c) Distribution of linear slopes fit to 33 individual curves derived from (b). Note the slope is based on logarithmic axis. (d) Histogram of prediction error, expressed as a percentage, for the pairwise-adjacent model for n-neuron correlation. Solid line indicates the mean error.

physics literature, one often makes the distinction of examining n-point correlations to calculate the strength of n interacting elements. In our case, an n-point correlation corresponds precisely the frequency at which n neurons fire simultaneously. We examine the spatial scaling of n-point correlations across multiple sub-mosaics within our population of neurons. In Figure 6.5b we plot the average and variance of n-neuron correlations across 33 sub-sampled mosaics. The curve from statistical independence drops sharply in a linear fashion indicative of the fact that statistical independence vastly and systematically under-predicts the observed n-neuron correlation. The fact that the n-neuron correlation curve decreases at a lesser rate reflects the strongly correlated activity only evident in larger populations of neurons. We summarize this information by reporting the distribution of linear slopes fit to individual curves, although we note that the observed n-neuron correlations do not necessarily decay linearly [126]. All of the statistics of large scale firing patterns (Figures 6.3, 6.4 and 6.5) describe a population of neurons that contains a spatial organization tightly coupled to the mosaic structure of the anatomy. Furthermore, the strength of spatial correlations becomes evident at larger populations of neurons as evident in the growing systematic divergences from statistical independence. The subject of the remainder of these sections is to attempt to account for this correlated activity.

6.5 Synchrony between adjacent neurons explains spatial activity of complete neural population

One perspective is that these spatial correlations reflect divergent elements in the retinal circuit (e.g. amacrine cells) which provide common input on to multiple RGCs and thus reflect a mechanism for multiplexing visual signals across multiple RGCs [191, 261]. Implicitly, this hypothesis necessitates measuring from all neurons in this circuit in order to characterize the cor-

related activity. Conversely, a more parsimonious mechanism is that spatial correlations reflect the propagation of spiking activity across pairwise circuit elements such as homotypic gap junctions between neighboring RGCs [119, 125, 65, 130] or even synaptic or electrical synapses between a single amacrine cell on to effectively two RGCs [65, 130]. One benefit of the latter type of circuit is that correlated activity between neighboring cells would dictate all observable spatial correlations. In theory, one could measure synchrony between pairs of neighboring cells and "stitch" together the complete firing pattern distribution. The latter possibility is quite appealing for two reasons. First, by predicting the complete firing patterns one would see that local interactions dictate large-scale phenomena. Second, the number of pairwise measurements between adjacent neurons grows linearly with the number of neurons vastly reducing the complexity of the neural circuit and the dimension of the correlated firing patterns.

Quantifying such notions has proven difficult as determining how multi-neuron firing patterns should be predicted from pairwise synchrony is subtle [261]. We review such ideas in the case of three neurons $x = (x_1, x_2, x_3)$. The observed distribution $P_{obs}(x)$ consists of 8 binary firing patterns (e.g. triplet synchrony 111). The observed synchrony between each pair of neurons is quantified by the pairwise distributions $P(x_1, x_2), P(x_1, x_3)$ and $P(x_2, x_3)$. The goal of this exercise is to predict a joint distribution $\hat{P}(x)$ using our knowledge of $P(x_1, x_2), P(x_1, x_3)$ and $P(x_2, x_3)$ but shrewdly avoiding assumptions about the prevalence of any additional structure beyond pairwise interactions. One technique, borrowed from statistical mechanics [132, 133], is to select the distribution which maximizes the randomness, or *entropy*, but matches the observed synchrony between pairs of cells. The maximum entropy distribution is

$$\hat{P}(x) = \arg\max_{P(x)} \left[H[P] + \sum_{i=1}^{N} \lambda_i (E[f_i(x)] - k_i) \right] \tag{6.1}$$

where $H[P] = -\sum_x P(x) \log_2 P(x)$ is the entropy of a firing pattern distribution $P(x)$ and λ_i are Lagrange multipliers enforcing selected constraints (see Methods). This idea of predicting higher-order correlations from lower-order correlations was introduced in [8] (but see [178]) and extended in subsequent work [258, 259, 273]. In previous work, we found that the maximum entropy distribution can predict 99% of the correlations in the complete firing pattern distribution of up to 7 neurons from synchrony in adjacent neurons [273].

We extend such techniques to examine how well synchrony solely between adjacent RGCs predict the entire population activity (see Methods). We term this the pairwise-adjacent model P_{adj}. Again, we note that we can not compare the full firing pattern distributions P_{obs} and P_{adj} because the number of firing patterns are too large, thus we examine features of these distributions discussed previously (Section 6.4). In Figures 6.3a-c and 6.4a-c the pairwise-adjacent model (red curve) predicts all three features of the observed distribution up to an accuracy of 10^{-3} implying that cumulatively 99.9% of the firing patterns are accounted for by the pairwise-adjacent model. This can be verified visually by examining movies simulated from independent draws from P_{adj} for comparison to the observed activity (Supplementary Materials). Note that successive frames in P_{adj} (but not P_{obs}) are independent.

A second form of validation is to measure how close P_{adj} is to the observed distribution P_{obs} across all firing patterns in small subsets of neurons. The frequency of firing patterns of subsets of neurons are well-estimated and not subject to inherent biases (see Methods). In particular, one can calculate the average likelihood of observing the histogram of all firing patterns observed if the

Table 6.1: Accuracy of nearest neighbor Ising model for small-scale firing patterns. Each numerical entry indicates the percentage of deaprtures from statistical independence captured by a specific model, for a given stimulus condition and time bin size (Δt). The range indicates the mean plus or minus 1 SD across 50 groups tested, each consisting of 7 cells.

condition	Δt	pairwise-adjacent	fully pairwise	empirical
constant illumination	10 ms	$97.5 \pm 0.8\%$	$98.3 \pm 0.6\%$	$99.8 \pm 0.1\%$
	20 ms	$98.3 \pm 0.6\%$	$99.1 \pm 0.4\%$	$99.7 \pm 0.1\%$
	5 ms	$95.6 \pm 1.4\%$	$97.1 \pm 0.7\%$	$99.8 \pm 0.1\%$
white noise stimulus	10 ms	$97.4 \pm 0.5\%$	$98.4 \pm 0.5\%$	$99.6 \pm 0.1\%$

correct model were P_{model} [273]. The negative logarithm of this quantity is the Kullback-Leibler divergence $D_{model} \equiv D_{\mathrm{KL}}(P_{obs}||P_{model})$ and expresses in bits/s the similarity of an observed distribution to a candidate model P_{model}. To assess the success of a particular model, one can calculate the fraction of deviations from statistical independence P_{ind} accounted for by particular model, $1 - \frac{D_{model}}{D_{ind}}$, expressed as a percentage (Table 6.1). Across all four preparations. P_{adj} accounts for 97.5% $\pm$ 0.8% of the deviations from statistical independence in 50 mosaics of 7 neurons from the population.

Previous work has demonstrated that slight deviations can mask large contributions from higher order correlations or non-adjacent interactions [273]. To assess this possibility we compare the full pairwise-adjacent model to two benchmarks: P_{pair} is a maximum entropy model which accounts for synchrony between all pairs of neurons [273, 259]; P_{emp} is the actual data used to train the maximum entropy models. P_{pair} and P_{emp} provide benchmarks, respectively, for measuring the contributions from non-adjacent interactions and for measuring the reproducibility of the experiment itself (i.e. cross-validation). Across 50 mosaics of 7 neurons, we calculate that the empirical distribution P_{emp} and the fully pairwise model P_{pair} account for 99.8% $\pm$ 0.1% and 98.3% $\pm$ 0.6% of the deviation from statistical independence, respectively (Table 6.1). Hence, some of the failures of the pairwise-adjacent model can be attributed to counting statistics and

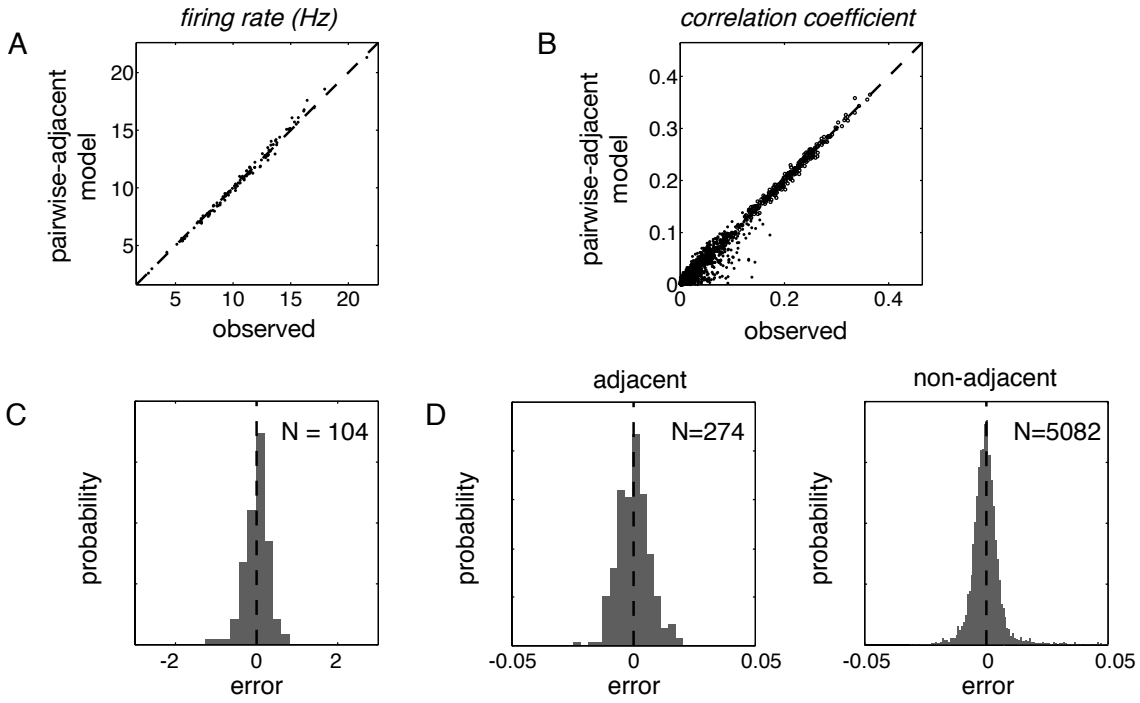

Figure 6.6: Validation of pairwise-adjacent model to first and second moments. Comparison of predicted (a) firing rate and (b) correlation coefficient across cross-validated data sets. Line indicates equality. Distribution of errors between observed and pairwise-adjacent model for (c) firing rates and (d) correlation coefficient (dashed line is zero). Note that non-adjacent correlation coefficients are not explicitly fit in the pairwise-adjacent model.

non-stationarity.

The lack of increased performance in the fully pairwise model suggests that P_{adj} generates non-adjacent correlations through the propagation of correlation. We can investigate this question by assessing the ability of P_{adj} to match the first and second moments (i.e. firing rate and correlation coefficient) of the observed distribution (Figure 6.6). The variance of errors in the firing rate and adjacent correlation coefficients reflects the precision of the model fit and natural variation in cross-validated data (see Methods). Non-adjacent correlation coefficients ($n = 5082$) exhibit similar variance but capture the general trend of observed correlation coefficients (Figure 6.6b and 6.6d, right panel), confirming that non-adjacent correlations are recovered eventhough they are not explicitly accounted for in the pairwise-adjacent model.

A closer examination of the pairwise-adjacent model does indicate systematic divergences from the observed firing patterns emerging in low frequency firing patterns that require a precise characterization of higher-order correlations. In particular, the pairwise-adjacent model fails to predict the frequency of large numbers of adjacent links and number of neurons firing (Figure 6.3a,c and 6.4a,c). Although these and other lesser frequency firing events comprise less than 1% of the observed activity, it appears that the pairwise-adjacent model systematically misestimates these large n-correlation patterns. A closer examination of n-neuron correlations confirms a small but growing prediction error as one examines larger mosaics of neurons (Figure 6.5d). The emerging systematic failure could arise from misidentified adjacency, inherently non-adjacent interactions or divergent common input.

In summary, we have observed that while not exhaustive, three lines of evidence support the notion that synchrony between adjacent neurons P_{adj} captures a majority of observed spatial correlations in the complete neural populations: (1) P_{adj} predicts a vast majority of several features of the complete distribution (Figure 6.3a-c, Figure 6.4a-c); (2) P_{adj} predicts the correlation coefficient in non-adjacent RGCs and (3) P_{adj} predicts the complete firing patterns in up to 7 neurons. We now investigate more closely the structure of the underlying network.

6.6 Identifying the dominant network organization governing population activity

The pairwise-adjacent model suggests that correlations between neighboring neurons play an important role in shaping network activity. We wish to make this role explicit and determine the network architecture for the complete population of neurons. Ideally, we would like to quantify the

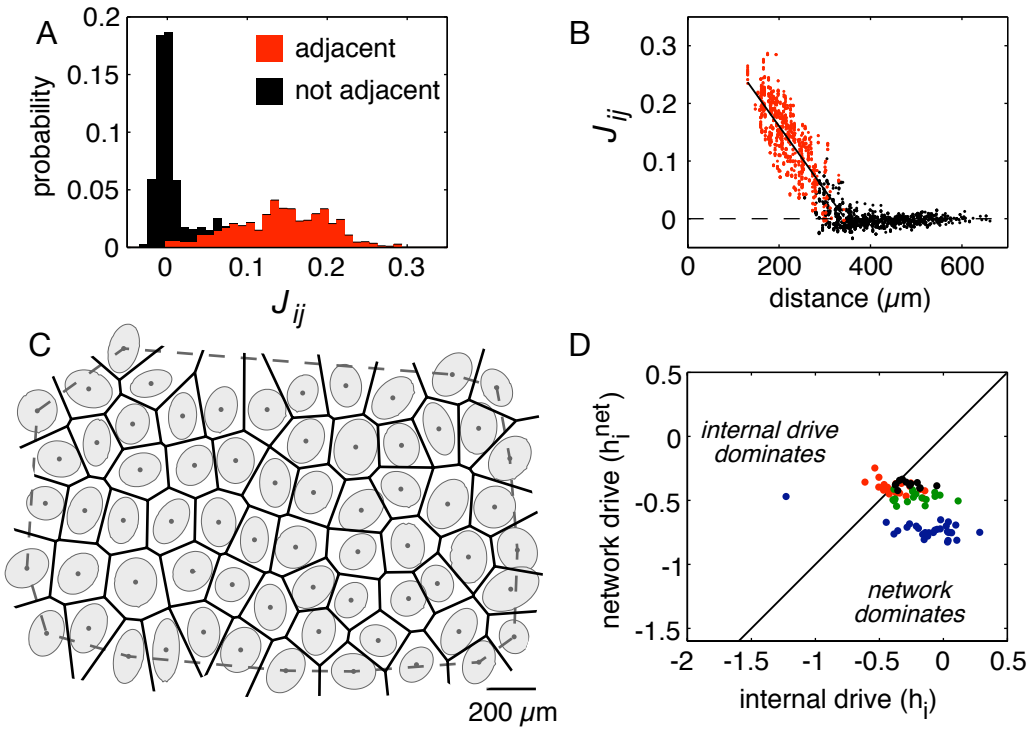

Figure 6.7: Adjacent interactions dominate single cell and network activity. (a) Distribution of Ising interaction terms J_{ij} for fully pairwise model P_{pair} across populations of $n = 8$ neurons. Red (black) points are (non-)adjacent cell pairs. (b) Ising interaction terms J_{ij} plotted as a function of distance between pairs of neurons. Colors follow (a). Black line is best fit line to adjacent cell pairs ($R^2 = -0.77$, slope $= -1.11x10^{-3}$ μm^{-1}). (c) Mosaic adjacency is determined through a Voronoi tesselation about receptive field centers (black dots). Cell pairs that share an edge in the tesselation (black lines) within the convex hull (dashed line) are defined as adjacent. (d) Comparison of internal drive h_i to average network drive h_i^{net} across four preparations (color indicates each preparation) for neurons internal to the mosaics. Line indicates equality.

role neighboring correlations play in determining the activity of the network as well as individual cells.

The maximum entropy formalism implicitly measures the strength of connections between neurons in the Lagrange multipliers used to enforce each imposed pairwise synchrony constraint. Recent theoretical work [259] has demonstrated that a binary distribution with all pairwise constraints can be rewritten as

$$P_{pair}(x) = \frac{1}{Z} \exp\left(\sum_{i=1}^{n} h_i x_i + \frac{1}{2}\sum_{i \neq j} J_{ij} x_i x_j\right) \tag{6.2}$$

where $x = (x_1, \ldots, x_n)$ is the binary firing pattern across n neurons, Z is a normalization constant, and $\{h_i, J_{ij}\}$ are the renamed Lagrange multipliers (see Methods). Computing the maximum entropy distribution is equivalent to computing the maximum likelihood estimate of $\{h_i, J_{ij}\}$ [62, 26]. Importantly, this distribution is recognized to be a form of an Ising model borrowed from statistical mechanics, whose parameters lend themselves to a physical interpretation: h_i the strength of a local, external field imposed on neuron i and J_{ij} is the effective interaction strength between neurons i and j after taking into account the propagation of correlation between intermediary neurons [259].

We focus our attention on the interaction terms J_{ij} because this parameter reflects the intrinsic connection strength between neurons i and j and collectively encapsulate the network architecture of the neural population. To more closely explore the structure of the network, we compute the interaction terms J_{ij} for 100 mosaics of 8 neurons from one retina and plot the distribution of J_{ij} (Figure 6.7a; compare with Figure 3b from [259]). The interaction terms are mostly positive and form a bimodal distribution with one sharp peak centered about zero. To explain the shape

and variance of this distribution, we plot these interaction terms as a function of distance between receptive field centers (Figure 6.7b). We find a regular linear decay with distance ($R^2 = -0.77$, slope $= -1.11x10^{-3}\ \mu m^{-1}$) and a sharp knee where interaction terms asymptote about zero. The linear decay in the magnitude of the interaction terms with distance is consistent with the intrinsic strength being dictated by receptive field or dendritic field overlap between RGCs [184, 65].

A natural question is to ask if the knee in the plot and consequently the two modes of the distribution is consistent with an established biophysical mechanism [119, 65, 125]. For example, if gap junctions between dendritic arborizations in adjacent RGCs subserve a majority of the correlated activity, then one might predict that only neurons that are physically adjacent should contain non-zero effective interaction strengths. We test this prediction by labeling whether interaction terms arise from adjacent neurons, as identified with a shared edge in a Voronoi tessellation (Figure 6.7c; see Methods). Importantly, this geometrical distinction marks the knee of Figure 6.7b and labels each mode of the distribution of J_{ij} (Figure 6.7a). The variance in the adjacent mode of the distribution (red) is largely explained by the systematic variation of J_{ij} with distance ($R^2 = -0.77$). The variance in the non-adjacent mode can be interpreted as estimation error due to overfitting terms which should be zero. Thus, the pairwise model might provide too many parameters to account for the observed activity (see Discussion).

We conclude several important points from this observation. The first point is that adjacent interactions dominate the activity of the network as interaction terms J_{ij} are much larger than non-adjacent interactions. The second point is retrospective in that we now recognize why the pairwise-adjacent model P_{adj} performs as well as P_{pair}. By solely enforcing synchrony between adjacent neurons in the maximum entropy model, P_{pair} effectively sets $J_{ij} = 0$ for pairs of non-adjacent cells (or equivalently, sets all black points in Figure 6.7a to zero). Thus, the pairwise-adjacent

model is equivalent to Equation 6.2 with only nearest neighbor interactions; we emphasize that a nearest neighbor stipulation recovers the precise definition of the Ising model [126]. We visualize the network of this neural population in Figures 6.3d and 6.4d by drawing a line in red between receptive fields whose thickness is prescribed by the magnitude of each interaction term. Note the homogeneity of the network across the entire population except for edge effects due to cells not recorded. Thus, the network of the neural population is dominated by these nearest neighbor interactions.

An intriguing prediction suggests that in large networks, the activity of individual cells is dominated by all network interactions [259]. In contrast, we note that the measured correlation coefficients are all uniformly small ($R^2 \leq 0.4$) indicating that no single neuron dominates the activity of a second neuron. We test this prediction explicitly in our large populations of neurons by calculating the average interactions from all other neurons $h_i^{net} = \frac{1}{2}\sum_{i \neq j} J_{ij} x_j$ and comparing this quantity to the internal bias h_i. The results are plotted in Figure 6.3d and 6.4d by coloring in individual cells according to $h_i^{net} - h_i$. Note that cells in the interior of the mosaic are uniformly dominated by the activity of their neighboring cells in contrast to neurons at the edge of the mosaic (or near a mosaic hole). The edge effects are due to intrinsic biases in excluding neurons not recorded. We summarize the dominant effect of the network for the entire Ising model by comparing h_i and h_i^{net} for neurons internal to the mosaic (Figure 6.7d). Across all four preparations we find that the activity of individual cells are uniformly dominated by network activity. Thus, in large populations local adjacent interactions dominate the network as well as the activity of individual neurons.

6.7 Discussion

In this manuscript we have provided a first characterization of large-scale spatial correlations of a complete population of ON parasol cells. Accounting for a large fraction of all correlated activity, simultaneous activity is spatially isotropic and comprised of multiple islands of spatially contiguous activity. The type of circuits which might mediate this activity are numerous [245], however the observation of the numerical and spatial scale of correlated activity does place strong bounds on any excitatory circuit. For instance, if spatial correlations are driven by any excitatory circuit from an amacrine or bipolar cell, then such a cell does not drive more than ~ 15 spatially localized cells of the same type.

The issue of fan-out from an amacrine or bipolar cell becomes subtle in the context of visual stimulation. It is quite possible that inter-neurons become active in the presence of particular light levels (e.g. AII amacrine cells) or specific features of the stimulus (e.g. starburst amacrine cells) and consequently the spatial and numerical extent of the observed correlations might change dependent on stimulus conditions. Assessing such questions is important but requires controlling for correlations artificially introduced by the stimulus [227, 212]. As a first step, we examine these questions under a white noise checkerboard stimulus designed so as not to artificially generate correlations between RGCs. Under these stimulus conditions the results in Figure 6.3 and 6.4 are largely unchanged (data not shown). More complex stimuli should be tested in future examinations.

A consummate goal of neural coding research is to find tractable models to explain correlations in observed spike trains. Much research has focused on explaining *temporal correlations* through dimensional reduction techniques used to explain channel conductances [233, 298]. This

work has followed the same spirit in applying dimensional reduction guided by our prior knowledge of the neural circuit to simplify the observation of simultaneous activity in complete populations of neurons. In particular, we have exploited the existence of known electrical coupling between nearest neighbors in the mosaic to create a parsimonious and successful model of neural activity. Dimensional reduction can be recognized by counting the number of effective parameters in the distribution. In n neurons the distribution consists of $O(2^n)$ parameters; the pairwise model $O(n^2)$ and the pairwise-adjacent model $O(n)$. Importantly, the latter model P_{adj} contains the same complexity as a model based on statistical independence P_{ind} but is far more accurate at predicting the firing patterns of a complete population, where small correlations dominate at large scales. One might be able to reduce further all interaction terms to two parameters characterizing the slope of the best fit line in Figure 6.7b.

One drawback of this investigation is the lack of time and stimulus (but see [233]). This drawback could confuse these results because we average over a firing response distribution which potentially introduces higher order correlations. The success of this dimensional reduction be obscured in the presence of a stimulus that generates higher-order spatial correlation. For instance, in the presence of full field monitor flicker, in mosaics of 10 neurons, the fully pairwise model accounts for 95.5% $\pm$ 0.5% of the deviations from statistical independence even though higher order correlations from the stimulus clearly dominate the activity of individual cell (compare with [259]). Note, however, that the pairwise-adjacent model only recovers 81.1% $\pm$ 4.6% of deviations from statistical independence. A naive interpretation would conclude that a fully pairwise model successfully accounts for the activity but the small 10% could mask substantial higher-order correlations. Hence, quantifying the failures of these models through the contributions of higher-order correlations must be interpreted with caution [273].

The pairwise-adjacent model, or equivalently a nearest-neighbor Ising model, presents an intriguing result, namely that global structure can be predicted from local interactions. Furthermore, these local interactions dominate the activity of individual cells when taken together. The nearest neighbor structure of this network is identical to models used to explore phase transitions in physical media [126, 30, 108] and pattern recognition in associative memory [123, 121] and suggests that future work might explore whether a real population of neurons exhibit such features [296].

A new class of models present opportunity to examine the structure of networks of neurons while incorporating the stimulus-response relationship and dynamic properties of the neural population [298, 234]. This new class of models will permit one to explore whether the correlation structure exhibited by a neural population can be explained by network interactions as well as the stimulus-response relationship. Furthermore, a dynamic model of correlated activity will permit examining whether complex features such as adaptation [51], gain control [265] or changes to the structure of noise correlations (M. Chacron, personal communication) can be explained by a static or adapting network.

This chapter will appear in J Shlens, GD Field, JL Gauthier, M Greschner, A Sher, AM Litke & EJ Chichilnisky. *Islands of large-scale concerted activity in primate retina.* to appear.

Chapter 7

Conclusions and Future Directions

The first observations of correlated activity in RGCs [244, 12] followed by the foundational work of David Mastronarde [184] opened the door to a rich field of research from exploring mechanisms underlying retinal circuitry to exploring strategies for encoding visual information. Furthermore, the recent advent of large scale recording technology has highlighted how traditional notions of synchrony bely large scale networks of correlated activity which dominate retinal function [273, 259]. While this research has refined our understanding of how visual information is signaled to the brain, this work has had larger implications in the field of neuroscience: pioneering new sets of experimental tools for recording from populations of neurons [166, 266], inspiring the development of new quantitative tools for the analysis and characterization of neural populations [216, 273, 259, 304], refining our notions of how sensory information is represented (efficiently) and processed by neural circuitry [191, 261], and finally highlighting how simple biological mechanisms can produce complex information processing circuits [96, 190].

This detailed level of investigation has been made possible by earlier foundational work

characterizing the anatomy, cell types and circuit layout of the retina (reviewed in [245]). This groundwork made by previous generations of retinal anatomists and physiologists has framed the types of questions examined currently and structures how we think about the structure of correlated activity in the retina [273] and what function it subserves [96, 190]. Likewise, we suspect that the research on the near horizon will provide a similar role to the next decade of work, thus we now take this opportunity to revisit each section with particular attention to new methods and directions in investigating correlated activity in RGCs.

Our understanding of mechanisms shaping correlated activity will be profoundly influenced by new experimental techniques, in particular genetic manipulations, for dissecting neural circuitry. To be sure, established methods have yet to be exhausted: paired recordings, imaging and extrinsic stimulation of RGCs should establish the types of chemical and electrical inputs mediating correlated activity (F. Rieke, C. Sekirnjak, personal communication); genetic knockouts of specific connexins highlight how electrical synapses influence aspects of correlated activity [74, 306]. Furthermore, new dyes could overcome limits of traditional tracer dyes [124] and elucidate previously undiscovered electrical synapses. Finally, an entire battery of genetic techniques have been developed for selectively ablating particular cell types [280], identifying all mono-synaptic targets from a neuron [320] and hyper/de-polarizing individual cell types through the application of an exogenous neurotransmitter [289] or brief pulses of light [38, 293, 115]. These techniques of course rely on expressing proteins in particular cells which ultimately require identification of cell-type specific promoters. The application of such techniques provide exciting directions for reshaping our understanding of what mechanisms and circuitry create correlated activity in the retina.

Improving our understanding of mechanisms of correlated activity shapes our expectations

about what types of correlations should be observed. Although several works have demonstrated that correlated activity in populations of neurons can be understood rather parsimoniously [259, 273], many departures from this simple picture could arise in the future. Correlations within specific cell types are universal [273], however complexities and interdependencies could surface when examining correlations *between* identified RGC cell types and even amacrine cells. Adaptation in single neuron's correlations and strength of synchrony could be a novel mechanisms for visual signaling; observations and mechanisms for such multi-neuron adaptation in retina have been reported [4]. Evidence from other sensory systems suggest that such adaptation in intrinsic correlations optimizes the performance of sensory systems in the natural environment (M. Chacron, personal communication). How such ideas shape our investigation of correlated activity will be quite exciting as these open questions will shape the mechanisms searched for and the types of coding strategies available to the retina.

Discovering new mechanisms and forms of correlated activity will of course drive new questions about what implications such discoveries have on how the retina transmits visual information to the brain. Addressing such questions requires the development and successful applications of new quantitative methods for the analysis and modeling of populations of neurons. While new techniques from information theory abound [304], new parametric statistical models provide particularly exciting directions both because of their efficient tractability in neural data [216, 298] and numerous extensions for exploring and testing the response of entire networks to real visual stimuli. These techniques permit examining what types of stimulus features are efficiently represented in the retina and provide concrete (non-trivial) predictions of how network activity should adapt in various stimulus regimes. Furthermore, recent extensions to identify sources of latent common input (e.g. amacrine cells) should increase our ability to infer and predict the structure

of large scale correlated activity [158].

Explorations into correlated activity in the neural code of the retina is an exciting field truly at the intersection of applications of traditional anatomy, state-of-the-art electrophysiology and the forefront of new quantitative methods. While mastering all such techniques might be the aspiration of all scientists, this hope must be tempered by the reality that steady progress in such interdisciplinary research requires the diligent collaboration and cooperation of scientists from a variety of backgrounds (and good funding.)

This chapter is taken from J Shlens and EJ Chichilnisky, (2007) *Synchrony and concerted activity in the neural code of the retina.* In RR Hoy, GM Shepherd, AI Basbaum, A Kaneko and G Westheimer (ed). **The Senses: A Comprehensive Foundation**, Elsevier Press.

Appendix A

Methods

A.1 Recordings

Preparation and recording methods are described elsewhere [166, 100, 54]. Briefly, eyes were obtained from deeply and terminally anesthetized macaque monkeys (*Macaca mulatta*) used by other experimenters in accordance with institutional guidelines for the care and use of animals. Immediately after enucleation, the anterior portion of the eye and vitreous were removed in room light and the eye cup was placed in a bicarbonate buffered Ames' solution (Sigma; St. Louis, MO) and stored in darkness at 32-34 degrees C, pH 7.4, for $\geq$ 20 minutes prior to dissection. Under infrared illumination pieces of peripheral retina 3-5 mm in diameter, isolated from the retinal pigment epithelium, were placed flat against a planar array of 512 extracellular microelectrodes, covering an area of 1,800 x 900 μm. The present results were obtained from 30-60 m segments of recording. The preparation was perfused with Ames' solution bubbled with 95% O_2, 5% CO_2 and maintained at 32-34 degrees C, pH 7.4.

A.2 Spike sorting

The voltage on each electrode was digitized at 20 kHz and stored for off-line analysis. Details of recording methods and spike sorting are given elsewhere [166]. Briefly, spikes were identified using a threshold of 3 times the voltage SD. For each spike, the waveform of the spike and the simultaneous waveforms on 6 adjacent electrodes were extracted. Three to five waveform features were identified using principal component analysis. A mixture of Gaussians model was fit to the distribution of features using expectation maximization [83]. The number of clusters and initial conditions for the model was determined automatically using an adapted watershed transformation [50, 248] . All clusters were visually inspected and when necessary, a mixture of Gaussians model was instead fit using manually selected initial conditions. Clusters with a large number of refractory period violations (more than 10% estimated contamination), or spike rates below 1 Hz, were excluded from further analysis.

A.3 Stimulation and receptive field analysis

An optically reduced stimulus from a gamma-corrected cathode ray tube computer display refreshing at 120 Hz was focused on the photoreceptor outer segments. The low photopic intensity was controlled by neutral density filters in the light path. The mean photon absorption rate for the long (middle, short) wavelength sensitive cones was approximately equal to the rate that would have been caused by a spatially uniform monochromatic light of wavelength 561 (530, 430) nanometers and intensity 9200 (8700, 7100) photons/μm^2/sec, incident on the photoreceptors. For the collection of parasol cells shown in Figure 5.2a, the mean firing rate during exposure to a steady, spatially uniform display at this light level was 10.7 $\pm$ 3.3 Hz for ON cells and 17.1 $\pm$ 3.5

Hz for OFF cells.

Spatio-temporal receptive fields were measured using a dynamic checkerboard (white noise) stimulus in which the intensity of each display phosophor was selected randomly and independently over space and time from a binary distribution. RMS stimulus contrast was 96%, stimulus duration was 30 m. The pixel size (60 μm) was selected to accurately capture the spatial structure of parasol cell receptive fields. For each RGC, the spike-triggered average stimulus was computed; this summarizes how the cell integrates visual inputs over space and time [176, 52]. An elliptical 2-dimensional Gaussian function was fit to the the spatial profile; outlines in Figure 5.2a represent 1 SD boundary of these fits.

A.4 Identifying adjacent neurons in mosaic

Several statistics (e.g. Figure 6.3b,c) as well as the pairwise-adjacent model P_{adj} rely on defining which cells are physically adjacent with one another. This geometrical notion of adjacency is meant to identify RGCs whose dendritic arborizations overlap and consequently might reciprocally couple via gap junctions [65, 130].

In previous work, we developed a parametric routine for determining an adjacency matrix based on examining the statistics of the distances between receptive field centers (normalized by the radii and orientation of receptive fields) [273]. In this work we used a non-parametric technique based solely on receptive field center locations. We defined every point in stimulus space as "belonging" to a particular neuron if the point is closest to the neuron's receptive field center. This definition delineates boundaries shared by typically two receptive field centers bisecting regions "belonging" to each cell. The set of boundaries demonstrated for one mosaic in Figure 6.7c is

called a *Voronoi tessellation* [307] (see also [209]). A pair of cells that share a common boundary are defined as adjacent. The Voronoi tessellation requires no user-defined notions of distance and provides a rough approximation of the typical convex hull drawn by anatomists to trace out the extent of an RGCs dendritic arborization [65].

The Voronoi tessellation provides a reasonable approximation of adjacency but fails in notable cases. Importantly, a Voronoi tessellation misidentifies adjacency if a hole exists in the mosaic due to an unrecorded cell (e.g. Figure 6.3, bottom left). Likewise, the tessellation will misidentify adjacency between cells along the edge of the mosaic because a boundary between two cells exists a large distance from the actual mosaic. Thus, we add a secondary stipulation that adjacency is solely defined by a shared edge within the convex hull of the mosaic receptive field centers. This, for instance, excludes two cells in the upper right of Figure 6.7c from being labeled as adjacent.

A.5 Maximum entropy

Maximum entropy methods are used in statistical inference to identify an unknown distribution given several constraints which are insufficient to fully specify the answer. A parsimonious unique solution is to select the distribution with the greatest *entropy* consistent with the constraints [132, 133, 60]. The entropy indicates the average number of bits required to transmit the identity of samples from a distribution [60]. Mathematically, maximizing the entropy is equivalent to selecting the maximum likelihood distribution consistent with the observed data [26].

Specifically, suppose the unknown distribution is $P(x)$, where x is a vector. Assume that N

constraints on the distribution are known:

$$E[f_i(x)] = k_i, \ \forall i \in \{1,\ldots,N\} \tag{A.1}$$

where $E[\cdot]$ is the expectation over the unknown distribution and $f_i(\cdot)$ is an arbitrary function of x. The maximum entropy solution is the distribution which maximizes entropy subject to the observed constraints:

$$\hat{P}(x) = \arg\max_{P(x)} \left[H[P] + \sum_{i=1}^{N} \lambda_i (E[f_i(x)] - k_i) \right] \tag{A.2}$$

where $H[P] = -\sum_x P(x) \log_2 P(x)$ is the entropy of a distribution $P(x)$ and λ_i are Lagrange multipliers. The second derivative matrix (or Hessian) of this equation is negative definite for all x. Thus, no local maxima exist and the unique global maximum can be found with any constrained gradient ascent optimization technique [238, 26, 173, 71, 178]. The functional form of the maximum entropy solution with pairwise constraints is an exponential distribution, which matches the Ising model in statistical mechanics [117] and the Hopfield model of neural networks [123]. The multipliers $\{\lambda_i\}$ measure the magnitude and sign of interactions between pairs of neurons; in the present work the estimated multipliers were universally positive (data not shown).

For the present analysis, spike trains were binned at a resolution of 10 ms; bins with 2 or more spikes (fewer than 1%) were replaced with 1. The distribution $P(x)$ is over all binary words x expressed by M cells; this is a 2^M element vector (see Figure 5.5). For example, for $M = 3$ cells, $P(x)$ is the probability distribution over the words $\{(0,0,0),(0,0,1),\cdots,(1,1,1)\}$. The constraint is a linear function specifying which distribution values to sum to generate the observed marginal

distributions, e.g. $P(1,1) = P(1,1,1) + P(1,1,0)$. In matrix form all constraints can be expressed as a $N \times 2^M$ sparse matrix with values of 1 selecting which elements of the joint distribution sum to form the observed marginals. The exponential growth of the number of words with the number of cells analyzed necessitates efficient algorithms to estimate the maximum entropy distribution [26, 173], and effectively limits the number of cells that can be analyzed simultaneously. Any constrained gradient ascent method can be used to find $\hat{P}(x)$ although in practice, specialized algorithms exploiting Jensen's inequality can be faster [26]. The search terminated when the fractional change in entropy was smaller than 10^{-8}.

A.6 Ising models

In the case of of simultaneous activity the firing pattern distribution of n neurons consists of a set of binary random variables $x = (x_1, x_2, \ldots, x_n)$. A binary distribution which solely enforces all pairwise constraints P_{pair} between individual neurons can be reformulated as the form of the Ising model (Equation 3.2)by relabeling the absence of a spike as -1 [258, 259]. In this reformulation the Lagrange multipliers $\{\lambda_i\}$ parameterize the distribution and are renamed $\{h_i, J_{ij}\}$ to extend a physical interpretation to the parameters. The maximum entropy distribution can be recast as calculating the maximum likelihood estimate of the Lagrange multipliers (or Ising parameters). Calculating the maximum likelihood estimate of the parameters of the Ising model is a special case of estimating the parameters of a discrete Markov random field [137] or equivalently, a Boltzmann machine [121]. Many specialized algorithms exist for estimating paramters of this class of graphical models using approximations of the likelihood [224, 120] and simulated annealing [121, 117] — although the problem of estimating these parameters in large models is recognized to be quite difficult and an area of active research [327].

A drawback of these methods is that most optimization techniques require an explicit calculation of the probability distribution, which in turn requires normalizing across all possible firing patterns. In the case of simultaneous activity the firing pattern distribution across n neurons consists of a set of binary random variables $x = (x_1, x_2, \ldots, x_n)$ with over 2^n elements. Hence, determining the normalization constant across the firing pattern distribution for the entire neural population (e.g. $2^{104} \sim 10^{30}$ patterns) is infeasible. Estimating the parameters of the Ising model requires a method to make draws from the distribution according to the unnormalized probability distribution. This can be achieved using Markov Chain Monte Carlo (MCMC) techniques [146, 102] which can be exploited to draw samples from an unnormalized distribution. Traditional MCMC sampling, however, can be laboriously slow because severe auto-correlation can exist between individual draws from the distribution. Thus we use a specialized form of sampling for Ising models [288] that exhibits better mixing properties.

To estimate the parameters of the Ising model at large n we employ MCMC to draw samples of our estimated distribution and calculate the complete likelihood gradient for each set of parameters [224]. To assure appropriate convergence, we employ an adaptive learning rate a learning rate that systematically decreases as a function of the number of trials, while in parallel incrementing the number of samples from the MCMC procedure to improve the fidelity of the likelihood gradient. This procedure amounts to a form of simulated annealing commonly employed in neural networks literature [117]. These learning procedures are validated by the ability of the Ising model to reproduce the selected constraints from the observed probability distribution. In the case of the pairwise-adjacent model P_{adj}, this amounts to identifying to matching the firing rates of individual neurons and the correlation coefficient between adjacent neurons (Figure 6.6c, 6.6d, right panel). Note that some error still exists reflecting the convergence criterion selected and the

variation across cross-validated data sets.

A.7 Kullback-Leibler divergence and likelihood

The Kullback-Leibler (KL) divergence is a measure in statistics [60] that quantifies in bits how close a probability distribution $p = \{p_i\}$ is to a model (or candidate) distribution $q = \{q_i\}$,

$$D_{\mathrm{KL}}(p \,||\, q) = \sum_i p_i \log_2 \frac{p_i}{q_i}$$

D_{KL} is non-negative (≥ 0), not symmetric in p and q, zero if the distributions match exactly and can potentially equal infinity. A common technical interpretation – although bereft of intuition – is that the KL divergence is the "coding penalty" associated with selecting a distribution q to approximate the true distribution p [60].

An intuitive understanding, however, arises from likelihood theory - the probability that one observes a set of data given that a particular model were true [83]. Pretend we perform an experiment to measure a discrete, random variable - such as the simultaneous binned firing patterns of multiple neurons. If we perform a long experiment and make n measurements, we can count the number of times we observe each type of firing pattern, a histogram $c = \{c_i\}$, where $n = \sum_i c_i$. This histogram measures the relative frequency of each type of firing pattern. If this experiment lasts forever, the normalized histogram counts $\frac{c_i}{n}$ reflect an underlying distribution $p_i = \frac{c_i}{n}$. Pretend we have a candidate model for these firing patterns, the distribution q. What is the probability of observing the histogram counts c if the model q actually generated the observations? This

probability is given by the *multinomial likelihood* [83],

$$L \propto \prod_i q_i^{c_i}$$

To gain some intuition, imagine that we performed $n = 1$ measurements - in this case, the likelihood would be the q_i attributed to the single observed firing pattern. The likelihood L shrinks mutiplicatively as we perform more measurements (or n grows). Ideally, we want the probability to be invariant to the number of measurements - this is given by the average likelihood $\bar{L} = L^{\frac{1}{n}}$, a number between 0 and 1. Matching intuition, as we perform more measurements, if $\frac{c_i}{n} \to q_i$, then the average likelihood would be perfect, or $\bar{L} \to 1$. Conversely, as $\frac{c_i}{n}$ diverges from the model q_i, the average likelihood $\bar{L}$ decreases, approaching zero. The link between likelihood and the KL divergence arises from the fact that if we perform an infinite number of measurements (see [273]; Section 12.1 of [60]),

$$D_{\mathrm{KL}}(p \,||\, q) = -\log_2 \bar{L}.$$

Thus, if the distributions p and q are identical, $\bar{L} = 1$ and $D_{\mathrm{KL}} = 0$ (or if $\bar{L} = 0$, $D_{\mathrm{KL}} = \infty$). The central intuition is that the KL divergence effectively measures the average likelihood of observing (infinite) data with the distribution p if the particular model q actually generated the data.

The KL divergence has many applications and is a foundation of information theory and statistics [60]. For example, one can ask how similar a joint distribution $p(x,y)$ is to the product of its marginals $p(x)p(y)$ - this is the *mutual information*, a general measure of statistical dependence between two random variables [60, 271],

$$I(X;Y) = \sum_{x,y} p(x,y) \log_2 \frac{p(x,y)}{p(x)p(y)} \tag{A.3}$$

The mutual information is zero if and only if the two random variables X and Y are statistically independent. In addition to its role in mutual information, the KL divergence has been applied extensively in the neural coding literature, most recently to quantify the effects of conditional dependence between neurons (Section 4.2) [258, 159, 9] and to measure how well higher order correlations can be approximated by lower order structure (Section 3.5) [259, 273].

Bibliography

[1] HDI Abarbanel. *Analysis of Observed Chaotic Data*. Springer, 1997.

[2] LF Abbott and P Dayan. The effect of correlated variability on the accuracy of a population code. *Neural Comput*, 11(1):91–101, 1999.

[3] SW Aboelela and DW Robinson. Physiological response properties of displaced amacrine cells of the adult ferret retina. *Vis Neurosci*, 21(2):135–144, 2004.

[4] JM Ackert, SH Wu, JC Lee, J Abrams, EH Hu, I Perlman, and SA Bloomfield. Light-induced changes in spike synchronization between coupled on direction selective ganglion cells in the mammalian retina. *J Neurosci*, 26(16):4206–4215, 2006.

[5] ED Adrian. Synchronized reactions in the optic ganglion of dytiscus. *J Physiol*, 91(1): 66–89, 1937.

[6] ED Adrian and R Matthews. The action of light on the eye: Part iii. the interaction of retinal neurones. *J Physiol*, 65(3):273–298, 1928.

[7] B Aguera y Arcas, AL Fairhall, and W Bialek. Computation in a single neuron: Hodgkin and huxley revisited. *Neural Comput*, 15(8):1715–1749, 2003.

[8] S Amari. Information geometry on hierarchy of probability distributions. *IEEE Transactions on Information Theory*, 47(5):1701–1711, 2001.

[9] S Amari and H Nakahara. Correlation and independence in the neural code. *Neural Comput*, 18(6):1259–1267, 2006.

[10] DJ Amit. *Modelling Brain Function: The World of Attractor Neural Networks*. Cambridge University Press, 1992.

[11] FR Amthor, JS Tootle, and NM Grzywacz. Stimulus-dependent correlated firing in directionally selective retinal ganglion cells. *Vis Neurosci*, 22(6):769–787, 2005.

[12] D Arnett. Statistical dependence between neighboring retinal ganglion cells in goldfish. *Exp Brain Res*, 32(1):49–53, 1978.

[13] D Arnett and TE Spraker. Cross-correlation analysis of the maintained discharge of rabbit retinal ganglion cells. *J Physiol*, 317:29–47, 1981.

[14] DW Arnett. Correlation analysis of units recorded in the cat dorsal lateral geniculate nucleus. *Exp Brain Res*, 24(2):111–130, 1975.

[15] F Attneave. Some informational aspects of visual perception. *Psychol Rev*, 61(3):183–193, 1954.

[16] BB Averbeck and D Lee. Neural noise and movement-related codes in the macaque supplementary motor area. *J Neurosci*, 23(20):7630–7641, 2003.

[17] BB Averbeck, PE Latham, and A Pouget. Neural correlations, population coding and computation. *Nat Rev Neurosci*, 7(5):358–366, 2006.

[18] SA Baccus. Timing and computation in inner retinal circuitry. *Annu Rev Physiol*, 2006.

[19] R Barbieri, LM Frank, DP Nguyen, MC Quirk, V Solo, MA Wilson, and EN Brown. Dynamic analyses of information encoding in neural ensembles. *Neural Comput*, 16(2):277–307, 2004.

[20] HB Barlow. Possible principles underlying the transformation of sensory messages. In WA Rosenblith, editor, *Sensory Communication*, pages 217–234. MIT Press, Cambridge, MA, 1961.

[21] HB Barlow. Redundancy reduction revisited. *Network*, 12(3):241–253, 2001.

[22] JM Beggs and D Plenz. Neuronal avalanches in neocortical circuits. *J Neurosci*, 23(35): 11167–11177, 2003.

[23] JM Beggs and D Plenz. Neuronal avalanches are diverse and precise activity patterns that are stable for many hours in cortical slice cultures. *J Neurosci*, 24(22):5216–5229, 2004.

[24] MV Bennett. Seeing is relieving: electrical synapses between visualized neurons. *Nat Neurosci*, 3(1):7–9, 2000.

[25] MV Bennett, LC Barrio, TA Bargiello, DC Spray, E Hertzberg, and JC Saez. Gap junctions: new tools, new answers, new questions. *Neuron*, 6(3):305–320, 1991.

[26] A Berger, S Della Pietra, and C Della Pietra. A maximum entropy approach to natural language processing. *Computational Linguistics*, 22:1–36, 1996.

[27] M Bezzi, I Samengo, S Leutgeb, and SJ Mizumori. Measuring information spatial densities. *Neural Comput*, 14(2):405–420, 2002.

[28] W Bialek and A Zee. Coding and computation with neural spike trains. *J Stat Phys*, 59: 103–115, 1990.

[29] W Bialek, F Rieke, RR de Ruyter van Steveninck, and D Warland. Reading a neural code. *Science*, 252(5014):1854–1857, 1991.

[30] J.J. Binney, N. J. Dowrick, A. J. Fisher, M. E. J. Newman, N.J. Dowrick, A.J. Fisher, and M.E.J. Newman. *The Theory of Critical Phenomena: An Introduction to the Renormalization Group (Oxford Science Publications)*. Oxford University Press, USA, 1992.

[31] SA Bloomfield. Two types of orientation-sensitive responses of amacrine cells in the mammalian retina. *Nature*, 350(6316):347–350, 1991.

[32] SA Bloomfield. Relationship between receptive and dendritic field size of amacrine cells in the rabbit retina. *J Neurophysiol*, 68(3):711–725, 1992.

[33] SA Bloomfield and D Xin. A comparison of receptive-field and tracer-coupling size of amacrine and ganglion cells in the rabbit retina. *Vis Neurosci*, 14(6):1153–1165, 1997.

[34] R Boos, H Schneider, and H Wassle. Voltage- and transmitter-gated currents of all-amacrine cells in a slice preparation of the rat retina. *J Neurosci*, 13(7):2874–2888, 1993.

[35] AS Bordt, H Hoshi, ES Yamada, WC Perryman-Stout, and DW Marshak. Synaptic input to off parasol ganglion cells in macaque retina. *J Comp Neurol*, 498(1):46–57, 2006.

[36] A Borst and FE Theunissen. Information theory and neural coding. *Nat Neurosci*, 2(11): 947–957, 1999.

[37] B. Boycott, JE Dowling, and H Kolb. Organization of the primate retina: Light microscopy. *Phil Trans Royal Society London Series B, Biological Sciences*, 255(799):109–184, 1969.

[38] ES Boyden, F Zhang, E Bamberg, G Nagel, and K Deisseroth. Millisecond-timescale, genetically targeted optical control of neural activity. *Nat Neurosci*, 8(9):1263–1268, 2005.

[39] N Brenner, SP Strong, R Koberle, W Bialek, and RR de Ruyter van Steveninck. Synergy in a neural code. *Neural Comput*, 12(7):1531–1552, 2000.

[40] KL Briggman, HD Abarbanel, and WB Jr Kristan. Optical imaging of neuronal populations during decision-making. *Science*, 307(5711):896–901, 2005.

[41] IH Brivanlou, DK Warland, and M Meister. Mechanisms of concerted firing among retinal ganglion cells. *Neuron*, 20(3):527–539, 1998.

[42] AE Brockwell, AL Rojas, and RE Kass. Recursive bayesian decoding of motor cortical signals by particle filtering. *J Neurophysiol*, 91(4):1899–1907, 2004.

[43] RN Brooke, C Downer Jde, and TP Powell. Centrifugal fibres to the retina in the monkey and cat. *Nature*, 207(5004):1365–1367, 1965.

[44] EN Brown, LM Frank, D Tang, MC Quirk, and MA Wilson. A statistical paradigm for neural spike train decoding applied to position prediction from ensemble firing patterns of rat hippocampal place cells. *J Neurosci*, 18(18):7411–7425, 1998.

[45] EN Brown, RE Kass, and PP Mitra. Multiple neural spike train data analysis: state-of-the-art and future challenges. *Nat Neurosci*, 7(5):456–461, 2004.

[46] DA Butts. How much information is associated with a particular stimulus? *Network*, 14 (2):177–187, 2003.

[47] DA Butts and MS Goldman. Tuning curves, neuronal variability, and sensory coding. *PLoS Biol*, 4(4):e92, 2006.

[48] Gyorgy Buzsaki. *Rhythms of the Brain*. Oxford University Press, USA, 2006.

[49] JM Carmena, MA Lebedev, RE Crist, JE O'Doherty, DM Santucci, DF Dimitrov, PG Patil, CS Henriquez, and MA Nicolelis. Learning to control a brain-machine interface for reaching and grasping by primates. *PLoS Biol*, 1(2):E42, 2003.

[50] Kenneth R Castleman. *Digital image processing*. Prentice Hall, Englewood Cliffs, N.J, 1996.

[51] D Chander and EJ Chichilnisky. Adaptation to temporal contrast in primate and salamander retina. *J Neurosci*, 21(24):9904–9916, 2001.

[52] EJ Chichilnisky. A simple white noise analysis of neuronal light responses. *Network: Computation in Neural Systems*, 12(2):199–213, 2001.

[53] EJ Chichilnisky and DA Baylor. Synchronized firing by ganglion cells in monkey retina. *Soc Neurosci Abstr*, 25:1042, 1999.

[54] EJ Chichilnisky and RS Kalmar. Functional asymmetries in on and off ganglion cells of primate retina. *J Neurosci*, 22(7):2737–2747, 2002.

[55] DF Condorelli, R Parenti, F Spinella, A Trovato Salinaro, N Belluardo, V Cardile, and F Cicirata. Cloning of a new gap junction gene (cx36) highly expressed in mammalian brain neurons. *Eur J Neurosci*, 10(3):1202–1208, 1998.

[56] BW Connors and MA Long. Electrical synapses in the mammalian brain. *Annu Rev Neurosci*, 27:393–418, 2004.

[57] JE Cook and DL Becker. Gap junctions in the vertebrate retina. *Microsc Res Tech*, 31(5): 408–419, 1995.

[58] PB Cook and FS Werblin. Spike initiation and propagation in wide field transient amacrine cells of the salamander retina. *J Neurosci*, 14(6):3852–3861, 1994.

[59] R Cossart, D Aronov, and R Yuste. Attractor dynamics of network up states in the neocortex. *Nature*, 423(6937):283–288, 2003.

[60] TM Cover and JA Thomas. *Elements of information theory*. Wiley, New York, 1991.

[61] SJ Cruikshank, CE Landisman, JG Mancilla, and BW Connors. Connexon connexions in the thalamocortical system. *Prog Brain Res*, 149:41–57, 2005.

[62] I Csiszar. I divergence geometry of probability distributoins and minimization problems. *Annals of Probability*, 3:146–158, 1975.

[63] CA Curcio and KA Allen. Topography of ganglion cells in human retina. *J Comp Neurol*, 300(1):5–25, 1990.

[64] DM Dacey. The mosaic of midget ganglion cells in the human retina. *J Neurosci*, 13(12): 5334–5355, 1993.

[65] DM Dacey and S Brace. A coupled network for parasol but not midget ganglion cells in the primate retina. *Vis Neurosci*, 9(3-4):279–290, 1992.

[66] DM Dacey and MR Petersen. Dendritic field size and morphology of midget and parasol ganglion cells of the human retina. *Proc Natl Acad Sci U S A*, 89(20):9666–9670, 1992.

[67] DM Dacey, BB Peterson, FR Robinson, and PD Gamlin. Fireworks in the primate retina: in vitro photodynamics reveals diverse lgn-projecting ganglion cell types. *Neuron*, 37(1): 15–27, 2003.

[68] RF Dacheux and E Raviola. Horizontal cells in the retina of the rabbit. *J Neurosci*, 2(10): 1486–1493, 1982.

[69] D.J Daley and D. Vere-Jones. *An Introduction to the Theory of Point Processes, Volume 1*. Springer, 2002.

[70] Y Dan, JM Alonso, WM Usrey, and RC Reid. Coding of visual information by precisely correlated spikes in the lateral geniculate nucleus. *Nat Neurosci*, 1(6):501–507, 1998.

[71] JN Darroch and D Ratcliff. Generalized iterative scaling for log-linear models. *Ann Math Stats*, 43:1470–1480, 1972.

[72] RR de Ruyter van Steveninck and W Bialek. Real-time performance of a movement-sensitive neuron in the blowfly visual system: coding and information transfer in short spike sequences. *Proc Roy Soc Lond B*, 234(1277):379–414, 1988.

[73] MR Deans and DL Paul. Mouse horizontal cells do not express connexin26 or connexin36. *Cell Commun Adhes*, 8(4-6):361–366, 2001.

[74] MR Deans, B Volgyi, DA Goodenough, SA Bloomfield, and DL Paul. Connexin36 is essential for transmission of rod-mediated visual signals in the mammalian retina. *Neuron*, 36(4):703–712, 2002.

[75] R Dermietzel and DC Spray. Gap junctions in the brain: where, what type, how many and why? *Trends Neurosci*, 16(5):186–192, 1993.

[76] PB Detwiler, AL Hodgkin, and PA McNaughton. Temporal and spatial characteristics of the voltage response of rods in the retina of the snapping turtle. *J Physiol*, 300:213–250, 1980.

[77] SH DeVries. Correlated firing in rabbit retinal ganglion cells. *J Neurophysiol*, 81(2):908–920, 1999.

[78] SH DeVries and DA Baylor. Mosaic arrangement of ganglion cell receptive fields in rabbit retina. *J Neurophysiol*, 78(4):2048–2060, 1997.

[79] SH DeVries and DA Baylor. An alternative pathway for signal flow from rod photoreceptors to ganglion cells in mammalian retina. *Proc Natl Acad Sci U S A*, 92(23):10658–10662, 1995.

[80] MR DeWeese and M Meister. How to measure the information gained from one symbol. *Network*, 10(4):325–340, 1999.

[81] AG Dimitrov and JP Miller. Neural coding and decoding: communication channels and quantization. *Network*, 12(4):441–472, 2001.

[82] MW Dubin. The inner plexiform layer of the vertebrate retina: a quantitative and comparative electron microscopic analysis. *J Comp Neurol*, 140(4):479–505, 1970.

[83] RO Duda, PE Hart, and DG Stork. *Pattern classification*. Wiley & Sons, New York, 2001.

[84] FE Dudek, A Obenaus, and JG Tasker. Osmolality-induced changes in extracellular volume alter epileptiform bursts independent of chemical synapses in the rat: importance of non-synaptic mechanisms in hippocampal epileptogenesis. *Neurosci Lett*, 120(2):267–270, 1990.

[85] FE Dudek, T Yasumura, and JE Rash. 'Non-synaptic' mechanisms in seizures and epileptogenesis. *Cell Biol Int*, 22(11-12):793–805, 1998.

[86] J Eichhorn, A Tolias, A Zien, M Kuss, C Rasmussen, J Weston, NK Logothetis, and B Schölkopf. Prediction on spike data using kernel algorithms. In S Thrun, L Saul, and B Schölkopf, editors, *Advances in Neural Information Processing Systems*, volume 16, Cambridge, MA, 2004. MIT Press.

[87] AK Engel, P Fries, and W Singer. Dynamic predictions: oscillations and synchrony in top-down processing. *Nat Rev Neurosci*, 2(10):704–716, 2001.

[88] GL Fain. Interactions of rod and cone signals in the mudpuppy retina. *J Physiol*, 252(3): 735–769, 1975.

[89] AL Fairhall, CA Burlingame, R Narasimhan, RA Harris, JL Puchalla, and MJ 2nd Berry. Selectivity for multiple stimulus features in retinal ganglion cells. *J Neurophysiol*, 96(5): 2724–2738, 2006.

[90] EV Famiglietti. Polyaxonal amacrine cells of rabbit retina: morphology and stratification of pa1 cells. *J Comp Neurol*, 316(4):391–405, 1992.

[91] EV Famiglietti. Polyaxonal amacrine cells of rabbit retina: PA2, PA3, and PA4 cells. light and electron microscopic studies with a functional interpretation. *J Comp Neurol*, 316(4): 422–446, 1992.

[92] EV Famiglietti. Polyaxonal amacrine cells of rabbit retina: size and distribution of pa1 cells. *J Comp Neurol*, 316(4):406–421, 1992.

[93] EV Jr Famiglietti and H Kolb. Structural basis for on-and off-center responses in retinal ganglion cells. *Science*, 194(4261):193–195, 1976.

[94] A Feigenspan, B Teubner, K Willecke, and R Weiler. Expression of neuronal connexin36 in aii amacrine cells of the mammalian retina. *J Neurosci*, 21(1):230–239, 2001.

[95] A Feigenspan, U Janssen-Bienhold, S Hormuzdi, H Monyer, J Degen, G Sohl, K Willecke, J Ammermuller, and R Weiler. Expression of connexin36 in cone pedicles and off-cone bipolar cells of the mouse retina. *J Neurosci*, 24(13):3325–3334, 2004.

[96] GD Field and EJ Chichilnisk. Information processing in the retina: Circuitry, coding, and mechanism. *Ann Reviews in Neuroscience*, 30, 2007.

[97] GD Field, AP Sampath, and F Rieke. Retinal processing near absolute threshold: from behavior to mechanism. *Ann Revs Physiol*, 67, 2005.

[98] SI Firth, CT Wang, and MB Feller. Retinal waves: mechanisms and function in visual system development. *Cell Calcium*, 37(5):425–432, 2005.

[99] ES Frechette, MI Grivich, R Kalmar, AM Litke, D Petrusca, A Sher, and EJ Chichilnisky. Ensemble retinal motion signals and limits on behavioral speed discrimination. *Soc Neurosci Abstr*, 30, 2004.

[100] ES Frechette, A Sher, MI Grivich, D Petrusca, AM Litke, and EJ Chichilnisky. Fidelity of the ensemble code for visual motion in primate retina. *J Neurophysiol*, 94(1):119–135, 2005.

[101] MA Freed and P Sterling. The on-alpha ganglion cell of the cat retina and its presynaptic cell types. *J Neurosci*, 8(7):2303–2320, 1988.

[102] Dani Gamerman and Hedibert F. Lopes. *Markov Chain Monte Carlo: Stochastic Simulation for Bayesian Inference, Second Edition (Texts in Statistical Science Series)*. Chapman & Hall/CRC, 2006.

[103] I Gat and N Tishby. Synergy and redundancy among brain cells of behaving monkeys. In Kearns MS, Solla SA, and Cohn DA, editors, *Adv Neural Information Processing Systems*, volume 11, pages 111–117, 1999.

[104] TJ Gawne and BJ Richmond. How independent are the messages carried by adjacent inferior temporal cortical neurons? *J Neurosci*, 13(7):2758–2771, 1993.

[105] W Gerstner and W Kistler. *Spiking neuron models: single neurons, populations, plasticity*. Cambridge University Press, Cambridge, MA, 2002.

[106] G Gestri, L Maffei, and D Petracchi. Statistical independence of events in neighboring retinal units. *Brain Res*, 2(4):397–398, 1966.

[107] KK Ghosh, AK Goodchild, AE Sefton, and PR Martin. Morphology of retinal ganglion cells in a new world monkey, the marmoset callithrix jacchus. *J Comp Neurol*, 366(1): 76–92, 1996.

[108] N Goldenfeld. *Lectures on Phase Transitions and the Renormalization Group*. Westview Press, 1992.

[109] HD Golledge, S Panzeri, F Zheng, G Pola, JW Scannell, DV Giannikopoulos, RJ Mason, MJ Tovee, and MP Young. Correlations, feature-binding and population coding in primary visual cortex. *Neuroreport*, 14(7):1045–1050, 2003.

[110] DA Goodenough, JA Goliger, and DL Paul. Connexins, connexons, and intercellular communication. *Annu Rev Biochem*, 65:475–502, 1996.

[111] JD Green. The hippocampus. *Physiol Rev*, 44:561–608, 1964.

[112] M Guldenagel, G Sohl, A Plum, O Traub, B Teubner, R Weiler, and K Willecke. Expression patterns of connexin genes in mouse retina. *J Comp Neurol*, 425(2):193–201, 2000.

[113] J Haag and A Borst. Encoding of visual motion information and reliability in spiking and graded potential neurons. *J Neurosci*, 17(12):4809–4819, 1997.

[114] EC Hampson, DI Vaney, and R Weiler. Dopaminergic modulation of gap junction permeability between amacrine cells in mammalian retina. *J Neurosci*, 12(12):4911–4922, 1992.

[115] X Han and ES Boyden. Multiple-color optical activation, silencing, and desynchronization of neural activity, with single-spike temporal resolution. *PLoS ONE*, 2:e299, 2007.

[116] S He and RH Masland. Retinal direction selectivity after targeted laser ablation of starburst amacrine cells. *Nature*, 389(6649):378–382, 1997.

[117] John Hertz, Anders Krogh, and Richard G Palmer. *Introduction to the theory of neural computation*. Addison-Wesley Pub. Co, Redwood City, Calif, 1991.

[118] S Hidaka, M Maehara, O Umino, Y Lu, and Y Hashimoto. Lateral gap junction connections between retinal amacrine cells summating sustained responses. *Neuroreport*, 5(1):29–32, 1993.

[119] S Hidaka, Y Akahori, and Y Kurosawa. Dendrodendritic electrical synapses between mammalian retinal ganglion cells. *J Neurosci*, 24(46):10553–10567, 2004.

[120] GE Hinton. Training products of experts by minimizing contrastive divergence. *Neural Comput*, 14(8):1771–1800, 2002.

[121] GE Hinton and TJ Sejnowski. Learning and relearning in boltzmann machines. In DE Rumelhart and JL McClelland, editors, *Parallel Distributed Processing: Explorations in the Microstructure of Cognition. Volume 1: Foundations*, pages 45–76. MIT Press, Cambridge, MA, 1986.

[122] DW Hochman, SC Baraban, JW Owens, and PA Schwartzkroin. Dissociation of synchronization and excitability in furosemide blockade of epileptiform activity. *Science*, 270 (5233):99–102, 1995.

[123] JJ Hopfield. Neural networks and physical systems with emergent collective computational abilities. *Proc Natl Acad Sci U S A*, 79(8):2554–2558, 1982.

[124] H Hoshi, J O'Brien, and SL Mills. A novel fluorescent tracer for visualizing coupled cells in neural circuits of living tissue. *J Histochem Cytochem*, 54(10):1169–1176, 2006.

[125] EH Hu and SA Bloomfield. Gap junctional coupling underlies the short-latency spike synchrony of retinal alpha ganglion cells. *J Neurosci*, 23(17):6768–6777, 2003.

[126] K Huang. *Statistical Mechanics. Second Edition.* see notes for publisher info, 1987.

[127] DR Humphrey, EM Schmidt, and WD Thompson. Predicting measures of motor performance from multiple cortical spike trains. *Science*, 170(959):758–762, 1970.

[128] Y Ikegaya, G Aaron, R Cossart, D Aronov, I Lampl, D Ferster, and R Yuste. Synfire chains and cortical songs: temporal modules of cortical activity. *Science*, 304(5670):559–564, 2004.

[129] H Ishikane, M Gangi, S Honda, and M Tachibana. Synchronized retinal oscillations encode essential information for escape behavior in frogs. *Nat Neurosci*, 8(8):1087–1095, 2005.

[130] RA Jacoby, D Stafford, N Kouyama, and D Marshak. Synaptic inputs to on parasol ganglion cells in the primate retina. *J Neurosci*, 16(24):8041–8056, 1996.

[131] RA Jacoby, AF Wiechmann, SG Amara, BH Leighton, and DW Marshak. Diffuse bipolar cells provide input to off parasol ganglion cells in the macaque retina. *J Comp Neurol*, 416 (1):6–18, 2000.

[132] ET Jaynes. Information theory and statistical mechanics. *Phys Rev*, 106:620–630, 1957.

[133] ET Jaynes. Information theory and statistical mechanics ii. *Phys Rev*, 108:171–190, 1957.

[134] JG Jefferys. Nonsynaptic modulation of neuronal activity in the brain: electric currents and extracellular ions. *Physiol Rev*, 75(4):689–723, 1995.

[135] JA Johnsen and MW Levine. Correlation of activity in neighbouring goldfish ganglion cells: relationship between latency and lag. *J Physiol*, 345:439–449, 1983.

[136] R Jolivet, TJ Lewis, and W Gerstner. Generalized integrate-and-fire models of neuronal activity approximate spike trains of a detailed model to a high degree of accuracy. *J Neurophysiol*, 92(2):959–976, 2004.

[137] Michael I. Jordan. *Learning in Graphical Models (Adaptive Computation and Machine Learning)*. The MIT Press, 1998.

[138] PR Jusuf, PR Martin, and U Grunert. Random wiring in the midget pathway of primate retina. *J Neurosci*, 26(15):3908–3917, 2006.

[139] ER Kandel, JH Schwartz, and TM Jessell. *Principles of Neural Science*. McGraw-Hill Medical, 2000.

[140] A Kaneko, LH Pinto, and M Tachibana. Transient calcium current of retinal bipolar cells of the mouse. *J Physiol*, 410:613–629, 1989.

[141] E Kaplan. The receptive field structure of retinal ganglion cells in cat and monkey. In A Leventhal, editor, *The Neural Basis of Visual Function*, pages 10–40. 1991.

[142] K Karmeier, HG Krapp, and M Egelhaaf. Population coding of self-motion: applying bayesian analysis to a population of visual interneurons in the fly. *J Neurophysiol*, 94(3): 2182–2194, 2005.

[143] Steven M. Kay. *Fundamentals of Statistical Signal Processing, Volume I: Estimation Theory*. Prentice Hall PTR, 1993.

[144] J Keat, P Reinagel, RC Reid, and M Meister. Predicting every spike: a model for the responses of visual neurons. *Neuron*, 30(3):803–817, 2001.

[145] R Kelly and TS Lee. Decoding v1 neuronal activity using particle filtering with volterra kernels. In S Thrun, L Saul, and B Schölkopf, editors, *Advances in Neural Information Processing Systems*, volume 16, Cambridge, MA, 2004. MIT Press.

[146] MB Kennel, J Shlens, HD Abarbanel, and EJ Chichilnisky. Estimating entropy rates with bayesian confidence intervals. *Neural Comput*, 17(7):1531–1576, 2005.

[147] GT Kenyon and DW Marshak. Gap junctions with amacrine cells provide a feedback pathway for ganglion cells within the retina. *Proc Biol Sci*, 265(1399):919–925, 1998.

[148] GT Kenyon, J Theiler, JS George, BJ Travis, and DW Marshak. Correlated firing improves stimulus discrimination in a retinal model. *Neural Comput*, 16(11):2261–2291, 2004.

[149] O Kinouchi and M Copelli. Optimal dynamical range of excitable networks at criticality. *Nature Physics*, 2:348–351, 2006.

[150] S Kirkpatrick and D Sherrington. Infinite-ranged models of spin-glasses. *Phys Rev B*, 17: 4384 – 4403, 1978.

[151] H Kolb and EV Famiglietti. Rod and cone pathways in the inner plexiform layer of cat retina. *Science*, 186(4158):47–49, 1974.

[152] H Kolb and D Marshak. The midget pathways of the primate retina. *Doc Ophthalmol*, 106 (1):67–81, 2003.

[153] H Kolb and R Nelson. Off-alpha and off-beta ganglion cells in cat retina: Ii. neural circuitry as revealed by electron microscopy of hrp stains. *J Comp Neurol*, 329(1):85–110, 1993.

[154] H Kolb, KA Linberg, and SK Fisher. Neurons of the human retina: a golgi study. *J Comp Neurol*, 318(2):147–187, 1992.

[155] MA Koontz and AE Hendrickson. Stratified distribution of synapses in the inner plexiform layer of primate retina. *J Comp Neurol*, 263(4):581–592, 1987.

[156] MA Koontz and AE Hendrickson. Distribution of gaba-immunoreactive amacrine cell synapses in the inner plexiform layer of macaque monkey retina. *Vis Neurosci*, 5(1):17–28, 1990.

[157] W Krebs and IP Krebs. Quantitative morphology of the central fovea in the primate retina. *Am J Anat*, 184(3):225–236, 1989.

[158] JE Kulkarni and L Paninski. Common-input models for multiple neural spike-train data. *submitted*, 2007.

[159] PE Latham and S Nirenberg. Synergy, redundancy, and independence in population codes, revisited. *J Neurosci*, 25(21):5195–5206, 2005.

[160] M Laufer and M Verzeano. Periodic activity in the visual system of the cat. *Vision Res*, 7 (3):215–229, 1967.

[161] SB Laughlin. Efficiency and complexity in neural coding. *Novartis Found Symp*, 239: 177–87; discussion 187–92, 234–40, 2001.

[162] G Laurent. Olfactory network dynamics and the coding of multidimensional signals. *Nat Rev Neurosci*, 3(11):884–895, 2002.

[163] E.L. Lehmann and George Casella. *Theory of Point Estimation (Springer Texts in Statistics)*. Springer, 2003.

[164] B Lin and RH Masland. Populations of wide-field amacrine cells in the mouse retina. *J Comp Neurol*, 499(5):797–809, 2006.

[165] J Liske, Lemon DJ, Driver SP, Cross NJG, and Couch WJ. The millennium galaxy catalogue: $16 <$ bmgc < 24 galaxy counts and the calibration of the local galaxy luminosity function. *Monthly Notices of the Royal Astronomical Society*, 344:307, 2003.

[166] AM Litke, N Bezayiff, EJ Chichilnisky, W Cunningham, W Dabrowski, AA Grillo, M Grivich, P Grybos, P Hottowy, S Kachiguine, RS Kalmar, K Mathieson, D Petrusca, M Rahman, and A Sher. What does the eye tell the brain? development of a system for the large scale recording of retinal output activity. *IEEE Trans Nucl Sci*, pages 1434–1440, 2004.

[167] R Llinas and Y Yarom. Electrophysiology of mammalian inferior olivary neurones in vitro. different types of voltage-dependent ionic conductances. *J Physiol*, 315:549–567, 1981.

[168] Rodolfo R. Llinas. *I of the Vortex: From Neurons to Self*. The MIT Press, 2001.

[169] MA Long, MR Deans, DL Paul, and BW Connors. Rhythmicity without synchrony in the electrically uncoupled inferior olive. *J Neurosci*, 22(24):10898–10905, 2002.

[170] CK Machens, MB Stemmler, P Prinz, R Krahe, B Ronacher, and AV Herz. Representation of acoustic communication signals by insect auditory receptor neurons. *J Neurosci*, 21(9): 3215–3227, 2001.

[171] MA MacNeil and RH Masland. Extreme diversity among amacrine cells: implications for function. *Neuron*, 20(5):971–982, 1998.

[172] MA MacNeil, JK Heussy, RF Dacheux, E Raviola, and RH Masland. The shapes and numbers of amacrine cells: matching of photofilled with golgi-stained cells in the rabbit retina and comparison with other mammalian species. *J Comp Neurol*, 413(2):305–326, 1999.

[173] R Malouf. A comparison of algorithms for maximum entropy parameter estimation. In B Andersson, M Bergholtz, and P Johannesson, editors, *Proceedings of the Sixth Conference on Natural Language Learning (CoNLL-2002)*, pages 49–55, Stockholm, Sweden, 2002.

[174] AP Mariani. Amacrine cells of the rhesus monkey retina. *J Comp Neurol*, 301(3):382–400, 1990.

[175] AP Mariani and LB Hersh. Synaptic organization of cholinergic amacrine cells in the rhesus monkey retina. *J Comp Neurol*, 267(2):269–280, 1988.

[176] PZ Marmarelis and K Naka. White-noise analysis of a neuron chain: an application of the wiener theory. *Science*, 175(27):1276–1278, 1972.

[177] DW Marshak, LB Aldrich, J Del Valle, and T Yamada. Localization of immunoreactive cholecystokinin precursor to amacrine cells and bipolar cells of the macaque monkey retina. *J Neurosci*, 10(9):3045–3055, 1990.

[178] L Martignon, G Deco, K Laskey, M Diamond, W Freiwald, and E Vaadia. Neural coding: higher-order temporal patterns in the neurostatistics of cell assemblies. *Neural Comput*, 12 (11):2621–2653, 2000.

[179] PR Martin and U Grunert. Spatial density and immunoreactivity of bipolar cells in the macaque monkey retina. *J Comp Neurol*, 323(2):269–287, 1992.

[180] SC Massey, JJ O'Brien, EB Trexler, W Li, JW Keung, SL Mills, and J O'Brien. Multiple neuronal connexins in the mammalian retina. *Cell Commun Adhes*, 10(4-6):425–430, 2003.

[181] DN Mastronarde. Correlated firing of cat retinal ganglion cells. i. spontaneously active inputs to x- and y-cells. *J Neurophysiol*, 49(2):303–324, 1983.

[182] DN Mastronarde. Correlated firing of cat retinal ganglion cells. ii. responses of x- and y-cells to single quantal events. *J Neurophysiol*, 49(2):325–349, 1983.

[183] DN Mastronarde. Interactions between ganglion cells in cat retina. *J Neurophysiol*, 49(2): 350–365, 1983.

[184] DN Mastronarde. Correlated firing of retinal ganglion cells. *Trends Neurosci*, 12(2):75–80, 1989.

[185] EM Maynard, NG Hatsopoulos, CL Ojakangas, BD Acuna, JN Sanes, RA Normann, and JP Donoghue. Neuronal interactions improve cortical population coding of movement direction. *J Neurosci*, 19(18):8083–8093, 1999.

[186] P. McCullagh and John A. Nelder. *Generalized Linear Models, Second Edition (Monographs on Statistics and Applied Probability)*. Chapman & Hall/CRC, 1989.

[187] WJ McGill. Multivariate informaton transmission. *IRE Trans Info Theory*, 4:93–111, 1954.

[188] JT McIlwain. Receptive fields of optic tract axons and lateral geniculate cells: peripheral extent and barbiturate sensitivity. *J Neurophysiol*, 27:1154–1173, 1964.

[189] M Meister. Multineuronal codes in retinal signaling. *Proc Natl Acad Sci USA*, 93(2): 609–614, 1996.

[190] M Meister and MJ Berry. The neural code of the retina. *Neuron*, 22(3):435–450, 1999.

[191] M Meister, L Lagnado, and DA Baylor. Concerted signaling by retinal ganglion cells. *Science*, 270(5239):1207–1210, 1995.

[192] M. Mezard, Giorgio Parisi, and M. Virasoro. *Spin Glass Theory and Beyond (World Scientific Lecture Notes in Physics, Vol 9)*. World Scientific Publishing Company, 1987.

[193] G Miller and W Madow. On the maximum likelihood estimate of the shannon-wiener measure of information. *Air Force Cambridge REsearch Center Technical Report*, 75:54, 1954.

[194] SL Mills and SC Massey. Labeling and distribution of aii amacrine cells in the rabbit retina. *J Comp Neurol*, 304(3):491–501, 1991.

[195] SL Mills and SC Massey. Differential properties of two gap junctional pathways made by aii amacrine cells. *Nature*, 377(6551):734–737, 1995.

[196] SL Mills and SC Massey. The kinetics of tracer movement through homologous gap junctions in the rabbit retina. *Vis Neurosci*, 15(4):765–777, 1998.

[197] SL Mills and SC Massey. A series of biotinylated tracers distinguishes three types of gap junction in retina. *J Neurosci*, 20(22):8629–8636, 2000.

[198] SL Mills, JJ O'Brien, W Li, J O'Brien, and SC Massey. Rod pathways in the mammalian retina use connexin 36. *J Comp Neurol*, 436(3):336–350, 2001.

[199] Todd K. Moon and Wynn C. Stirling. *Mathematical Methods and Algorithms for Signal Processing*. Prentice Hall, 1999.

[200] NS Narayanan, EY Kimchi, and M Laubach. Redundancy and synergy of neuronal ensembles in motor cortex. *J Neurosci*, 25(17):4207–4216, 2005.

[201] K Negishi and T Teranishi. Close tip-to-tip contacts between dendrites of transient amacrine cells in carp retina. *Neurosci Lett*, 115(1):1–6, 1990.

[202] I Nemenman, F Shafee, and W Bialek. Entropy and inference, revisited. In TG Dietterich, S Becker, and Z Ghahramani, editors, *Advances in neural information processsing systems*, volume 14, Cambridge, MA, 2002. MIT Press.

[203] S Neuenschwander and W Singer. Long-range synchronization of oscillatory light responses in the cat retina and lateral geniculate nucleus. *Nature*, 379(6567):728–732, 1996.

[204] S Neuenschwander, M Castelo-Branco, and W Singer. Synchronous oscillations in the cat retina. *Vision Res*, 39(15):2485–2497, 1999.

[205] S Nirenberg and PE Latham. Decoding neuronal spike trains: how important are correlations? *Proc Natl Acad Sci U S A*, 100(12):7348–7353, 2003.

[206] S Nirenberg, SM Carcieri, AL Jacobs, and PE Latham. Retinal ganglion cells act largely as independent encoders. *Nature*, 411(6838):698–701, 2001.

[207] H Ogawa, GI Cummins, GA Jacobs, and JP Miller. Visualization of ensemble activity patterns of mechanosensory afferents in the cricket cercal sensory system with calcium imaging. *J Neurobiol*, 66(3):293–307, 2006.

[208] K Ohki, S Chung, YH Ch'ng, P Kara, and RC Reid. Functional imaging with cellular resolution reveals precise micro-architecture in visual cortex. *Nature*, 433(7026):597–603, 2005.

[209] Atsuyuki Okabe, Barry Boots, Kokichi Sugihara, and Sung Nok Chiu. *Spatial Tessellations: Concepts and Applications of Voronoi Diagrams (Wiley Series in Probability and Statistics)*. Wiley, 2000.

[210] BP Olveczky, SA Baccus, and M Meister. Segregation of object and background motion in the retina. *Nature*, 423(6938):401–408, 2003.

[211] MW Oram, NG Hatsopoulos, BJ Richmond, and JP Donoghue. Excess synchrony in motor cortical neurons provides redundant direction information with that from coarse temporal measures. *J Neurophysiol*, 86(4):1700–1716, 2001.

[212] G Palm, AM Aertsen, and GL Gerstein. On the significance of correlations among neuronal spike trains. *Biol Cybern*, 59(1):1–11, 1988.

[213] L Paninski. Convergence properties of three spike-triggered analysis techniques. *Network*, 14(3):437–464, 2003.

[214] L Paninski. Estimation of entropy and mutual information. *Neural Comput*, 15(6):1191–1253, 2003.

[215] L Paninski. Maximum likelihood estimation of cascade point-process neural encoding models. *Network*, 15(4):243–262, 2004.

[216] L Paninski. Log-concavity results on gaussian process methods for supervised and unsupervised learning. In LK Saul, Y Weiss, and L Bottou, editors, *Neural Information Processing System*, volume 17, pages 1025–1032, Cambridge, MA, 2005. MIT Press.

[217] L Paninski, JW Pillow, and EP Simoncelli. Maximum likelihood estimation of a stochastic integrate-and-fire neural encoding model. *Neural Comput*, 16(12):2533–2561, 2004.

[218] L Paninski, JW Pillow, and J Lewi. Statistical models for neural encoding, decoding, and optimal stimulus design. In P Cisek, T Drew, and JF Kalaska, editors, *Computational Neuroscience: Theoretical Insights into Brain Function*. Elsevier, Amsterdam, 2007.

[219] S Panzeri, SR Schultz, A Treves, and ET Rolls. Correlations and the encoding of information in the nervous system. *Proc Biol Sci*, 266(1423):1001–1012, 1999.

[220] S Panzeri, G Pola, F Petroni, MP Young, and RS Petersen. A critical assessment of different measures of the information carried by correlated neuronal firing. *Biosystems*, 67(1-3):177–185, 2002.

[221] L Peichl and H Wassle. Morphological identification of on- and off-centre brisk transient (y) cells in the cat retina. *Proc R Soc Lond B Biol Sci*, 212(1187):139–153, 1981.

[222] L Peichl, EH Buhl, and BB Boycott. Alpha ganglion cells in the rabbit retina. *J Comp Neurol*, 263(1):25–41, 1987.

[223] AA Penn, RO Wong, and CJ Shatz. Neuronal coupling in the developing mammalian retina. *J Neurosci*, 14(6):3805–3815, 1994.

[224] P Perez. Markov random fields and images. *CWI Quarterly*, 11(4):413–437, 1998.

[225] J Perez-Orive, O Mazor, GC Turner, S Cassenaer, RI Wilson, and G Laurent. Oscillations and sparsening of odor representations in the mushroom body. *Science*, 297(5580):359–365, 2002.

[226] D Perkel and T Bullock. Neural coding. *Neurosci Res Prog Bull*, 6:221, 1968.

[227] DH Perkel, GL Gerstein, and GP Moore. Neuronal spike trains and stochastic point processes. ii. simultaneous spike trains. *Biophys J*, 7(4):419–440, 1967.

[228] DH Perkel, GL Gerstein, MS Smith, and WG Tatton. Nerve-impulse patterns: a quantitative display technique for three neurons. *Brain Res*, 100(2):271–296, 1975.

[229] RS Petersen, S Panzeri, and ME Diamond. Population coding of stimulus location in rat somatosensory cortex. *Neuron*, 32(3):503–514, 2001.

[230] RS Petersen, S Panzeri, and ME Diamond. Population coding in somatosensory cortex. *Curr Opin Neurobiol*, 12(4):441–447, 2002.

[231] J Pillow and L Paninski. Model-based decoding, information estimation, and change-point detection in multi-neuron spike trains. submitted, 2007.

[232] JW Pillow and EP Simoncelli. Dimensionality reduction in neural models: an information-theoretic generalization of spike-triggered average and covariance analysis. *J Vis*, 6(4): 414–428, 2006.

[233] JW Pillow, L Paninski, VJ Uzzell, EP Simoncelli, and EJ Chichilnisky. Prediction and decoding of retinal ganglion cell responses with a probabilistic spiking model. *J Neurosci*, 25(47):11003–11013, 2005.

[234] JW Pillow, J Shlens, L Paninski, EJ Chichilnisky, and EP Simoncelli. Modeling the correlated spike responses of a cluster of primate retinal ganglion cells. *Soc Neurosci Abstr*, 31, 2005.

[235] G Pola, A Thiele, KP Hoffmann, and S Panzeri. An exact method to quantify the information transmitted by different mechanisms of correlational coding. *Network*, 14(1):35–60, 2003.

[236] SL Polyak. *The retina*. University of Chicago Press, Chicago, 1941.

[237] M Potters and W Bialek. Statistical mechanics and visual signal processing. *J Phys I France*, 4:1755–1775, 1994.

[238] WH Press, BP Flannery, SA Teukolsky, and WT Vetterling. *Numerical recipes in C*. Cambridge University Press, Cambridge, England, 1988.

[239] JL Puchalla, E Schneidman, RA Harris, and MJ Berry. Redundancy in the population code of the retina. *Neuron*, 46(3):493–504, 2005.

[240] DS Reich, F Mechler, and JD Victor. Independent and redundant information in nearby cortical neurons. *Science*, 294(5551):2566–2568, 2001.

[241] J Reperant, R Ward, D Miceli, JP Rio, M Medina, NB Kenigfest, and NP Vesselkin. The centrifugal visual system of vertebrates: a comparative analysis of its functional anatomical organization. *Brain Res Brain Res Rev*, 52(1):1–57, 2006.

[242] F Rieke, DA Bodnar, and W Bialek. Naturalistic stimuli increase the rate and efficiency of information transmission by primary auditory afferents. *Proc R Soc Lond B Biol Sci*, 262 (1365):259–265, 1995.

[243] F Rieke, D Warland, RR de Ruyter van Steveninck, and W Bialek. *Spikes: exploring the neural code*. MIT Press, Cambridge, MA, 1997.

[244] RW Rodieck. Maintained activity of cat retinal ganglion cells. *J Neurophysiol*, 30(5): 1043–1071, 1967.

[245] RW Rodieck. *The first steps in seeing*. Sinauer, Sunderland, MA, 1998.

[246] RW Rodieck and TJ Haun. Parasol retinal ganglion cells in macaques connect intracelluarly to other parasol cells, and to amacrine cells found in the ganglion cell layer. In *Soc Neurosci Abstr*, volume 17, page 1375, 1991.

[247] RW Rodieck and DW Marshak. Spatial density and distribution of choline acetyltransferase immunoreactive cells in human, macaque, and baboon retinas. *J Comp Neurol*, 321(1):46–64, 1992.

[248] JBTM Roerdink and A Meijster. The watershed transform: Definitions, algorithms and parallelization strategies. *Fundamenta Informaticae*, 41(1-2):187–228, 2001.

[249] SN Roper, A Obenaus, and FE Dudek. Osmolality and nonsynaptic epileptiform bursts in rat ca1 and dentate gyrus. *Ann Neurol*, 31(1):81–85, 1992.

[250] DL Ruderman and W Bialek. Statistics of natural images: Scaling in the woods. *Physical Review Letters*, 73(6):814–817, 1994.

[251] NC Rust and JA Movshon. In praise of artifice. *Nat Neurosci*, 8(12):1647–1650, 2005.

[252] HM Sakai, K Naka, and JE Dowling. Ganglion cell dendrites are presynaptic in catfish retina. *Nature*, 319(6053):495–497, 1986.

[253] S Schein, P Sterling, IT Ngo, TM Huang, and S Herr. Evidence that each s cone in macaque fovea drives one narrow-field and several wide-field blue-yellow ganglion cells. *J Neurosci*, 24(38):8366–8378, 2004.

[254] NA Schellart and H Spekreijse. Origin of the stochastic nature of ganglion cell activity in isolated goldfish retina. *Vision Res*, 13(2):337–345, 1973.

[255] DM Schneeweis and JL Schnapf. Photovoltage of rods and cones in the macaque retina. *Science*, 268(5213):1053–1056, 1995.

[256] DM Schneeweis and JL Schnapf. The photovoltage of macaque cone photoreceptors: adaptation, noise, and kinetics. *J Neurosci*, 19(4):1203–1216, 1999.

[257] E Schneidman, W Bialek, and MJ Berry. Synergy, redundancy, and independence in population codes. *J Neurosci*, 23(37):11539–11553, 2003.

[258] E Schneidman, S Still, MJ Berry, and W Bialek. Network information and connected correlations. *Phys Rev Lett*, 91:238701, 2003.

[259] E Schneidman, MJ Berry, R Segev, and W Bialek. Weak pairwise correlations imply strongly correlated network states in a neural population. *Nature*, 440(7087):1007–1012, 2006.

[260] E Schneidman, J Puchalla, R Segev, RA Harris, W Bialek, and M Berry. Synergy from silence in a combinatorial neural code. 2007.

[261] MJ Schnitzer and M Meister. Multineuronal firing patterns in the signal from eye to brain. *Neuron*, 37(3):499–511, 2003.

[262] T Schubert, J Degen, K Willecke, SG Hormuzdi, H Monyer, and R Weiler. Connexin36 mediates gap junctional coupling of alpha-ganglion cells in mouse retina. *J Comp Neurol*, 485(3):191–201, 2005.

[263] AB Schwartz, DM Taylor, and SI Tillery. Extraction algorithms for cortical control of arm prosthetics. *Curr Opin Neurobiol*, 11(6):701–707, 2001.

[264] AB Schwartz, XT Cui, DJ Weber, and DW Moran. Brain-controlled interfaces: movement restoration with neural prosthetics. *Neuron*, 52(1):205–220, 2006.

[265] O Schwartz, EJ Chichilnisky, and EP Simoncelli. Characterizing neural gain control using spike-triggered covariance. In *Adv Neural Information Processing Systems*, volume 14, pages 269–276, Vancouver, BC, Canada, 2002. MIT Press.

[266] R Segev, J Goodhouse, J Puchalla, and MJ Berry. Recording spikes from a large fraction of the ganglion cells in a retinal patch. *Nat Neurosci*, 7(10):1154–1161, 2004.

[267] R Segev, J Puchalla, and MJ 2nd Berry. Functional organization of ganglion cells in the salamander retina. *J Neurophysiol*, 95(4):2277–2292, 2006.

[268] MD Serruya, NG Hatsopoulos, L Paninski, MR Fellows, and JP Donoghue. Instant neural control of a movement signal. *Nature*, 416(6877):141–142, 2002.

[269] MN Shadlen and WT Newsome. Noise, neural codes and cortical organization. *Curr Opin Neurobiol*, 4(4):569–579, 1994.

[270] MN Shadlen and WT Newsome. The variable discharge of cortical neurons: implications for connectivity, computation, and information coding. *J Neurosci*, 18(10):3870–3896, 1998.

[271] CE Shannon and W Weaver. *The mathematical theory of communication*. University of Illinois Press, Urbana, 1949.

[272] T Sharpee, NC Rust, and W Bialek. Analyzing neural responses to natural signals: maximally informative dimensions. *Neural Comput*, 16(2):223–250, 2004.

[273] J Shlens, GD Field, JL Gauthier, MI Grivich, D Petrusca, A Sher, AM Litke, and EJ Chichilnisky. The structure of multi-neuron firing patterns in primate retina. *J Neurosci*, 26(32):8254–8266, 2006.

[274] J Shlens, MB Kennel, HD Abarbanel, and E. J. Chichilnisky. Estimating information rates in neural spike trains with confidence intervals. *Neural Comput*, in press, 2007.

[275] S Shoham, LM Paninski, MR Fellows, NG Hatsopoulos, JP Donoghue, and RA Normann. Statistical encoding model for a primary motor cortical brain-machine interface. *IEEE Trans Biomed Eng*, 52(7):1312–1322, 2005.

[276] L Shpigelman, Y Singer, R Paz, and E Vaadia. Spikernels: predicting arm movements by embedding population spike rate patterns in inner-product spaces. *Neural Comput*, 17(3): 671–690, 2005.

[277] E. P. Simoncelli, L Paninski, J Pillow, and O Schwartz. Characterization of neural responses with stochastic stimuli. In MS Gazzaniga, editor, *The Cognitive Neurosciences*. MIT Press, Cambridge, MA, 2004.

[278] EP Simoncelli and BA Olshausen. Natural image statistics and neural representation. *Annu Rev Neurosci*, 24:1193–1216, 2001.

[279] LC Sincich and JC Horton. The circuitry of v1 and v2: integration of color, form, and motion. *Annu Rev Neurosci*, 28:303–326, 2005.

[280] JR Sinclair, AL Jacobs, and S Nirenberg. Selective ablation of a class of amacrine cells alters spatial processing in the retina. *J Neurosci*, 24(6):1459–1467, 2004.

[281] W Singer and OD Creutzfeldt. Reciprocal lateral inhibition of on- and off-center neurones in the lateral geniculate body of the cat. *Exp Brain Res*, 10(3):311–330, 1970.

[282] G Sohl, J Degen, B Teubner, and K Willecke. The murine gap junction gene connexin36 is highly expressed in mouse retina and regulated during brain development. *FEBS Lett*, 428 (1-2):27–31, 1998.

[283] Larry R. Squire, James L. Roberts, Nicholas C. Spitzer, Michael J. Zigmond, Susan K. McConnell, and Floyd E. Bloom. *Fundamental Neuroscience, Second Edition*. Academic Press, 2002.

[284] DK Stafford and DM Dacey. Physiology of the a1 amacrine: a spiking, axon-bearing interneuron of the macaque monkey retina. *Vis Neurosci*, 14(3):507–522, 1997.

[285] GJ Stephens, S Neuenschwander, JS George, W Singer, and GT Kenyon. See globally, spike locally: oscillations in a retinal model encode large visual features. *Biol Cybern*, 95 (4):327–348, 2006.

[286] JK Stevens and GL Gerstein. Interactions between cat lateral geniculate neurons. *J Neurophysiol*, 39(2):239–256, 1976.

[287] M Stopfer, S Bhagavan, BH Smith, and G Laurent. Impaired odour discrimination on desynchronization of odour-encoding neural assemblies. *Nature*, 390(6655):70–74, 1997.

[288] RH Swendsen and JS Wang. Nonuniversal critical dynamics in monte carlo simulations. *Physical Review Letters*, 58(2):86–88, 1987.

[289] EM Tan, Y Yamaguchi, GD Horwitz, S Gosgnach, ES Lein, M Goulding, TD Albright, and EM Callaway. Selective and quickly reversible inactivation of mammalian neurons in vivo using the drosophila allatostatin receptor. *Neuron*, 51(2):157–170, 2006.

[290] WR Taylor. Response properties of long-range axon-bearing amacrine cells in the dark-adapted rabbit retina. *Vis Neurosci*, 13(4):599–604, 1996.

[291] T Teranishi and K Negishi. Double-staining of horizontal and amacrine cells by intracellular injection with lucifer yellow and biocytin in carp retina. *Neuroscience*, 59(1):217–226, 1994.

[292] T Teranishi, K Negishi, and S Kato. Functional and morphological correlates of amacrine cells in carp retina. *Neuroscience*, 20(3):935–950, 1987.

[293] SM Thompson, JP Kao, RH Kramer, KE Poskanzer, RA Silver, D Digregorio, and SS Wang. Flashy science: controlling neural function with light. *J Neurosci*, 25(45): 10358–10365, 2005.

[294] EE Thomson and WB Kristan. Quantifying stimulus discriminability: a comparison of information theory and ideal observer analysis. *Neural Comput*, 17(4):741–778, 2005.

[295] N Tishby, FC Pereira, and W Bialek. The information bottleneck method. In Hajek B and Sreenivas RS, editors, *Proceedings of the 37th Annual Allerton Conference on Communication, Control and Computing*, pages 368–377. University of Illinois, 1999.

[296] G Tkacik, E Schneidman, M Berry, and W Bialek. Ising models for networks of real neurons. 2007.

[297] A Treves and S Panzeri. The upward bias in measures of information derived from limited data samples. *Neural Comput*, 7(2):399–407, 1995.

[298] W Truccolo, UT Eden, MR Fellows, JP Donoghue, and EN Brown. A point process framework for relating neural spiking activity to spiking history, neural ensemble, and extrinsic covariate effects. *J Neurophysiol*, 93(2):1074–1089, 2005.

[299] DY Ts'o, CD Gilbert, and TN Wiesel. Relationships between horizontal interactions and functional architecture in cat striate cortex as revealed by cross-correlation analysis. *J Neurosci*, 6(4):1160–1170, 1986.

[300] WM Usrey and RC Reid. Synchronous activity in the visual system. *Annu Rev Physiol*, 61: 435–456, 1999.

[301] DI Vaney. Many diverse types of retinal neurons show tracer coupling when injected with biocytin or neurobiotin. *Neurosci Lett*, 125(2):187–190, 1991.

[302] DI Vaney. Territorial organization of direction-selective ganglion cells in rabbit retina. *J Neurosci*, 14(11 Pt 1):6301–6316, 1994.

[303] DI Vaney. Patterns of neuronal coupling in the retina. *Progress in Retinal Eye Research*, 13 (1):301–355, 1994.

[304] JD Victor. Approaches to information-theoretic analysis of neural activity. *Biological Theory*, 1:302–316, 2006.

[305] B Volgyi, D Xin, Y Amarillo, and SA Bloomfield. Morphology and physiology of the polyaxonal amacrine cells in the rabbit retina. *J Comp Neurol*, 440(1):109–125, 2001.

[306] B Volgyi, J Abrams, DL Paul, and SA Bloomfield. Morphology and tracer coupling pattern of alpha ganglion cells in the mouse retina. *J Comp Neurol*, 492(1):66–77, 2005.

[307] G Voronoi. Nouvelles applications des paramtres continus la thorie des formes quadratiques. *Journal fr die Reine und Angewandte Mathematik*, 133:97–178, 1907.

[308] BA Wandell. *Foundations of vision*. Sinauer, Sunderland, MA, 1995.

[309] DK Warland, P Reinagel, and M Meister. Decoding visual information from a population of retinal ganglion cells. *J Neurophysiol*, 78(5):2336–2350, 1997.

[310] H Wassle and BB Boycott. Functional architecture of the mammalian retina. *Physiol Rev*, 71(2):447–480, 1991.

[311] H Wassle, BB Boycott, and RB Illing. Morphology and mosaic of on- and off-beta cells in the cat retina and some functional considerations. *Proc R Soc Lond B Biol Sci*, 212(1187): 177–195, 1981.

[312] H Wassle, L Peichl, and BB Boycott. Dendritic territories of cat retinal ganglion cells. *Nature*, 292(5821):344–345, 1981.

[313] H Wassle, L Peichl, and BB Boycott. Morphology and topography of on- and off-alpha cells in the cat retina. *Proc R Soc Lond B Biol Sci*, 212(1187):157–175, 1981.

[314] H Wassle, L Peichl, and BB Boycott. Mosaics and territories of cat retinal ganglion cells. *Prog Brain Res*, 58:183–190, 1983.

[315] H Wassle, U Grunert, MH Chun, and BB Boycott. The rod pathway of the macaque monkey retina: identification of aii-amacrine cells with antibodies against calretinin. *J Comp Neurol*, 361(3):537–551, 1995.

[316] M Watanabe and RW Rodieck. Parasol and midget ganglion cells of the primate retina. *J Comp Neurol*, 289(3):434–454, 1989.

[317] M Watanabe, Y Fukuda, CF Hsiao, and H Ito. Electron microscopic analysis of amacrine and bipolar cell inputs on y-, x-, and w-cells in the cat retina. *Brain Res*, 358(1-2):229–240, 1985.

[318] S Watanabe. Information theoretical analysis of multivariate correlation. *IBM J Res and Dev*, 4(66), 1960.

[319] AJ Weber, MA McCall, and LR Stanford. Synaptic inputs to physiologically identified retinal x-cells in the cat. *J Comp Neurol*, 314(2):350–366, 1991.

[320] IR Wickersham, DC Lyon, RJ Barnard, T Mori, S Finke, KK Conzelmann, JA Young, and EM Callaway. Monosynaptic restriction of transsynaptic tracing from single, genetically targeted neurons. *Neuron*, 53(5):639–647, 2007.

[321] MA Wilson and BL McNaughton. Dynamics of the hippocampal ensemble code for space. *Science*, 261(5124):1055–1058, 1993.

[322] U Wolff. Collective monte carlo updating for spin systems. *Physical Review Letters*, 62(4): 361–364, 1989.

[323] T Womelsdorf, P Fries, PP Mitra, and R Desimone. Gamma-band synchronization in visual cortex predicts speed of change detection. *Nature*, 2005.

[324] LL Wright and DI Vaney. The type 1 polyaxonal amacrine cells of the rabbit retina: a tracer-coupling study. *Vis Neurosci*, 21(2):145–155, 2004.

[325] S Wu, H Nakahara, and S Amari. Population coding with correlation and an unfaithful model. *Neural Comput*, 13(4):775–797, 2001.

[326] W Wu, Y Gao, E Bienenstock, JP Donoghue, and MJ Black. Bayesian population decoding of motor cortical activity using a kalman filter. *Neural Comput*, 18(1):80–118, 2006.

[327] Lan X, Roth S, Huttenlocher D, and MJ Black. Efficient belief propagation with learned higher-order markov random fields. In *European Conference on Computer Vision*, volume II, pages 269–282. Springer, 2006.

[328] D Xin and SA Bloomfield. Tracer coupling pattern of amacrine and ganglion cells in the rabbit retina. *J Comp Neurol*, 383(4):512–528, 1997.

[329] CY Yang, P Lukasiewicz, G Maguire, FS Werblin, and S Yazulla. Amacrine cells in the tiger salamander retina: morphology, physiology, and neurotransmitter identification. *J Comp Neurol*, 312(1):19–32, 1991.

[330] G Yang and RH Masland. Direct visualization of the dendritic and receptive fields of directionally selective retinal ganglion cells. *Science*, 258(5090):1949–1952, 1992.

[331] Y Yoshimura and EM Callaway. Fine-scale specificity of cortical networks depends on inhibitory cell type and connectivity. *Nat Neurosci*, 8(11):1552–1559, 2005.

[332] Y Yoshimura, JL Dantzker, and EM Callaway. Excitatory cortical neurons form fine-scale functional networks. *Nature*, 433(7028):868–873, 2005.

[333] K Zhang, I Ginzburg, BL McNaughton, and TJ Sejnowski. Interpreting neuronal population activity by reconstruction: unified framework with application to hippocampal place cells. *J Neurophysiol*, 79(2):1017–1044, 1998.